Exploring Orbital Physics with Angle-Resolved Photoemission Spectroscopy

by

Yue Cao

B.S., Tsinghua University, Beijing, China, 2007

M.S., University of Colorado, Boulder, 2010

A thesis submitted to the

Faculty of the Graduate School of the

University of Colorado in partial fulfillment

of the requirements for the degree of

Doctor of Philosophy

Department of Physics

2014

This thesis entitled:
Exploring Orbital Physics with Angle-Resolved Photoemission Spectroscopy
written by Yue Cao
has been approved for the Department of Physics

_____

Daniel S. Dessau

_____

Dmitry Reznik

Date _____

The final copy of this thesis has been examined by the signatories, and we find that both the
content and the form meet acceptable presentation standards of scholarly work in the above
mentioned discipline.

Cao, Yue (Ph.D., Physics)

Exploring Orbital Physics with Angle-Resolved Photoemission Spectroscopy

Thesis directed by Prof. Daniel S. Dessau

As an indispensable electronic degree of freedom, the orbital character dominates some of the key energy scales in the solid state — the electron hopping, Coulomb repulsion, crystal field splitting, and spin-orbit coupling. Recent years have witnessed the birth of a number of exotic phases of matter where orbital physics plays an essential role, e.g. topological insulators, spin-orbital coupled Mott insulators, orbital-ordered transition metal oxides, etc. However, a direct experimental exploration is lacking concerning how the orbital degree of freedom affects the ground state and low energy excitations in these systems.

Angle-resolved photoemission spectroscopy (ARPES) is an invaluable tool for observing the electronic structure, low-energy electron dynamics and in some cases, the orbital wavefunction. Here we perform a case study of (a) the topological insulator and (b) the $J_{1/2}$ Mott insulator Sr_2IrO_4 using ARPES.

For the prototype topological insulator Bi_2X_3 (X=Se, Te), our studies reveal the topological surface state has a spin-orbital coupled wavefunction asymmetric to the Dirac point, and it is possible to manipulate the spin of the photoelectron using polarized photons.

We also discover there are multiple features, including pseudogaps, Fermi "arcs", and marginal-Fermi-liquid-like electronic scattering rates in the effectively hole doped Sr_2IrO_4, which have been reported in the high-T_C cuprates. Due to the relatively simple phase diagram of these doped iridates, we find the aforementioned low energy features are not exclusive to preformed Cooper pairs, or the existence of Quantum Critical Points as suggested in influential theories. Instead, the short-range antiferromagnetic correlation might be vital to the description of the Mott-metal crossover.

Dedication

To Mom and Dad.

Acknowledgements

I would like to thank my advisor, Professor Dan Dessau, for leading me into the exciting frontiers of angle-resolved photoemission. I will always remember his stimulating guidance, and his devotion to me and other students throughout the years. He has helped me develop the critical skills needed as an independent researcher. I have learned a great deal from Dan in the past seven years, and there is much more to learn. I am grateful to Dan and his family, for putting up with the occasional after-hours discussions, sometimes at midnight.

I am fortunate to have all the former and present members of the Dessau group. Yi-De Chuang brought me into the world of X-ray scattering as a technique complimentary to ARPES, and offered me (and the rest of the group) invaluable help during the lengthy beamtime in Berkeley. Zhe Sun, Qiang Wang, Ted Reber and Nick Plumb taught me how to perform ARPES from the very beginning. I would like to thank them for willing to work through some of my "crazy" ideas in the early stage of some of these projects. I have spent many wonderful hours in Colorado and at beamlines with them, and also with Justin Griffith, Steve Parham, Justin Waugh, Daniel Weingarten, Haoxiang Li and Xiaoqing Zhou. We have together made many interesting discoveries, and have shared joyful memories.

Most of my experiment data were taken at lightsources around the world, including the Advanced Light Source (ALS, LBL), Synchrotron Radiation Center (SRC), Swiss Light Source (SLS, PSI) and the Hiroshima Synchrotron Radiation Center (HiSor). I would like to thank Sung-Kwan Mo, Eli Rotenberg, Aaron Bostwick, Jonathan Denlinger, Alexei Fedorov, J. Hugo Dil, R. S. Dhaka, Gabriel Landolt, Hideaki Iwasawa, Taichi Okuda, Koji Miyamoto, Bob Schoenlein, Wanli

Contents

Chapter

Tables

Table

Figures

Figure

Chapter 1

Orbital Physics in a Nutshell

An electron in a solid has four degrees of freedom: charge, spin, lattice and orbital. The first three degrees of freedom, charge, spin and lattice, have been the focus of study since the early days of condensed matter physics and now we have understood a great deal about them. For example, they have collective excitations including phasons, amplitudons, magnons, and phonons. Also the interactions between electrons and phonons could lead to conventional superconductivity in metals, as revealed by the "BCS theory" [1]. The orbital degree of freedom, however, is far less talked about. Recently, exotic physics and new phases of matter have been proposed and discovered in materials where orbitals play an essential role [2, 3, 4, 5, 6]. Orbital physics has emerged as a new frontier of condensed matter physics.

In this chapter, we provide an overview of the orbital physics, focusing on how orbitals determine/contribute to the fundamental energy scales in the solid. Similar to the study of other electron degrees of freedom, our ultimate goal is to understand how orbital physics affects the "low-energy" electronic structures and excitations near the Fermi level. This theis is but an initial experimental attempt in this new field, exploiting the versatility of the angle-resolved photoemission spectroscopy.

1.1 Describing Electrons Using Orbitals

The concept of "orbital" is rooted in atomic physics, which describes how electrons are spatially confined relative to the positively-charged ions. For semiconductors, insulators and even

some metals and semimetals, we could generally identify an electron in the solid as occupying an orbital centered at a constituting atom. Many materials vital to the modern energy and electronics industry, and also those of scientific interest fall into this category. The role of electron orbitals in these materials is dual: on the one hand, the spatial distribution of orbital wavefunctions directly determines the fundamental energy scales in the solid. On the other hand, the low energy wavefunction of electrons, which results from these orbital-related energy scales, could be treated as a superposition of the same set of orbital wavefunctions. In the first-principles calculations, this latter approach is termed the linear combination of atomic orbitals (LCAO). Thus the orbital degree of freedom serves as a "bridge" that connects the high-energy scales and the low-energy excitations. In a few cases, it is not straightforward to assign orbital characters to electrons. For example, in noble metals, electrons near the Fermi level form a mobile Fermi gas and are less confined to the atoms. After all, unlike charge and spin, the "orbital" is not an *intrinsic* property of an electron. However, we will not focus on these exceptions, as many of them are well understood.

Much we know about the real space orbitals comes from the hydrogen atom from undergraduate quantum mechanics, where each orbital can be identified by its radial and angular distribution and is usually labeled with quantum numbers n, l and m, respectively. The angular distribution is described by the spherical harmonics Y_{lm}, with $l = 0, 1, 2, 3$ corresponding to the s, p, d and f orbitals. Only the s angular wavefunction is isotropic. For a multi-electron atom, the solutions of the hydrogen atom are of course over-simplified. We could still adopt the same set of angular wavefunctions, while the radial wavefunctions are modified due to the Coulomb repulsion from other electrons around the positive ion.

Now we review how the fundamental energy scales (as they appear in a theoretical Hamiltonian) are determined by the orbital character. We list these energy scales with the increasing number of atoms.

On a single atom level, each atomic orbital could accommodate up to two electrons, due to the Pauli exclusion principle. A Coulomb repulsion U is produced between these two electrons. We could regard $U > 0$ as the energy cost to add an extra electron into the atomic orbital. For

the outer shell valence electrons, U increases with reduced n (or the number of filled inner shells). The filled inner shells effectively reduce the effective charge the outer electron sees and hence the Coulomb attraction. For 3d orbitals, U is on the order of $\sim$10eV. This number reduces to 2$\sim$3eV for the 5d orbitals [4]. Also, U increases with larger angular momentum l. For instance, with the same pinciple quantum number n, the d orbitals are spatially more localized than the p orbitals. The f electrons are so localized in space (and buried inside the s and p outer shell) that the corresponding valence band are essentially "flat" in momentum space, with a heavy band mass [7]. In this thesis we will focus on the physics of the p and d orbitals.

For an assembly of more than one atom, the energy level and density distribution of the orbitals are severely modified by the overlap of orbitals with the neighboring atoms.

In the case of two atoms, this is illustrated in the formation of chemical bonds. The terms "bonding" and "antibonding" reflect the orbital wavefunction symmetry and the spatial distribution between the two atoms. Also, the kinetic energy t for an electron to hop between two atoms is determined by the overlap of the participating orbital wavefunctions.

New physics is brought in as the number of neighboring atoms increases. We would like to mention two examples: in some cases, the symmetry of neighboring atoms deviates so badly from the orbital orientation, that the orbitals are "hybridized" into new orbitals. This is how chemical bonds form in the graphene as compared to the diamond. In the former, one s orbital and two planar p orbitals are mixed together (sp^2 hybridization) and the latter requires all three p orbitals to participate (sp^3 hybridization).

The other example I would like to discuss is the crystal field splitting. For an atom "caged" by atoms of (usually) different species, the surrounding atoms create a static electric field and split the otherwise degenerate orbitals of the centering atom. Without introducing the entire framework of crystal field theory, we provide a hand-waving explanation for the energy splitting in the octahedral atomic complex, as this is commonly seen in many material systems, including cuprates, iridates and manganites. Figure 1.1 **a** presents a cartoon of the octahedron, with the transition metal atom in the center and 6 oxygen atoms around it. The d orbitals (there are 5 of them) split
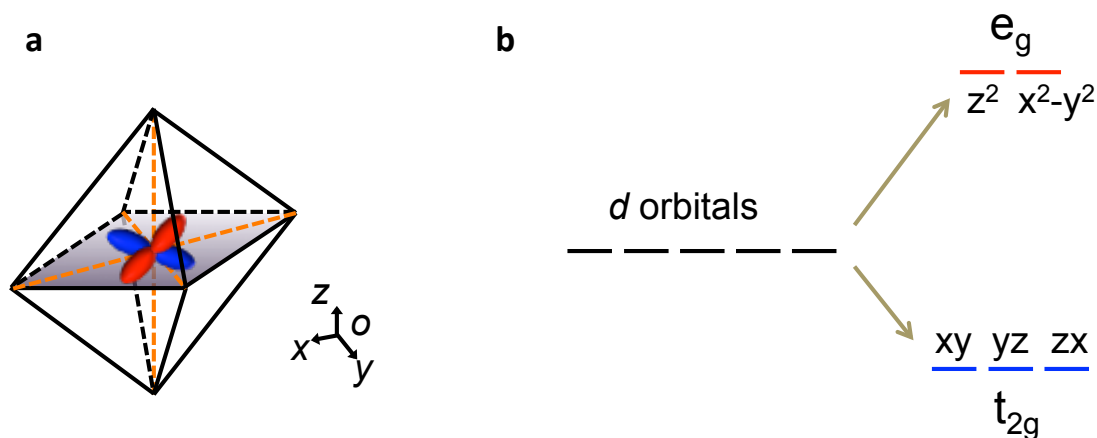
Figure 1.1: The crystal field splitting of d orbitals in an octahedral atomic complex. **a**. Geometry of the octahedron. The transition metal atom is at the center, and there is an oxygen atom at each of the 6 corners. The oxygen 2p orbitals extends along one of the x, y and z axis. We draw the wavefunction of the d_{xy} orbital at the center, with less overlap with the oxygen 2p orbitals than, e.g. the d_{z^2} orbital. The red/blue colors represent the relative phase of the d orbital wavefunction. **b**. The crystal field splitting. The two e_g orbitals have higher energy than the three t_{2g} orbitals.

into two groups. The d_{z^2} and $d_{x^2-y^2}$ orbitals (the e_g orbitals) are higher in energy (Figure 1.1 **b**) than the three t_{2g} orbitals d_{xy}, d_{yz} and d_{zx}. This is because the t_{2g} orbitals point away from the corner oxygen and there is less wavefunction overlap. For a perfect octahedron where the 6 oxygens share the same distance to the metal atom, the three t_{2g} orbitals (and the two e_g orbitals) are degenerate. However, these degenerate orbitals could further split in energy, as the octahedron becomes elongated, or as one octahedron shares a corner (or edge/face) with another octahedron.

For the 3d transition metal oxides, U is the largest term in energy. As the atomic number increases, U becomes smaller, while the electron hopping t is larger. For the 4d/5d transition metal oxides, the energy scales of t, U and E_{CF} are comparable, making possible the emergence of new phases of matter.

So far we have discussed important high-energy scales originating entirely from the orbitals. There are other local interactions that couple both the spin and the orbital degrees of freedom. These interactions require electrons to twist their spin as they hop from one orbital to another on the neighboring lattice site, to optimize (at least partially) the local energy. This local spin-orbital entanglement may have a global effect on the wavefunction symmetry and low-energy dynamics, as we will show throughout the thesis. We list two of the often-encountered spin-orbital interactions below:

For atoms with a high atomic number Z, the spin-orbit coupling increases as Z^4 and could no longer be neglected. In the case of topological insulators , the spin-orbit coupling is responsible for band inversion in the known topological insulators [5]. As we will show in Chapter 3, the spin-orbit coupling profoundly determines the unconventional spin polarization (which we will refer to as the spin-orbital texture) of the topological surface state.

For the lighter elements, where the atomic spin-orbit coupling is relatively small, the spin and orbital could still be coupled. This has been demonstrated in the complex phase diagrams of many 3d transition metal oxides, including doped manganites, nickelates and cobaltates [2]. In these materials, a new energy scale, the Hund's coupling J_H comes into play. Hund's rules state that the d shell tends to be filled or half filled whenever possible; and the electron spins tend to achieve

the largest total moment (the so-called high spin state). This rule suggests each new electron to be put into the 3d shell has to choose its orbital occupation and spin polarization simultaneously. This new electron either has to find an empty 3d orbital and maximize the total onsite moment (by aligning itself with electron spins on other d orbitals on the same site); or has to doubly fill a 3d orbital with the spin opposite to the electron already in that orbital.

1.2 The Scope and Organization of The Thesis

This thesis is dedicated to how the orbital physics manifests itself in the "low-energy" electronic structures and correlations. We present two cases — the topological insulators (Chapter 3) and doped J_{eff}=1/2 Mott insulator Sr_2IrO_4 (Chapter 5) — that exhibit two distinct facets of orbital physics. We explore these materials with angle-resolved photoemission spectroscopy (ARPES), and briefly introduce the basics of ARPES in Chapter 2.

As discussed in Section 1.1, the wavefunction of a solid could be considered as a superposition of all the relevant atomic orbitals. ARPES and first-principles calculations provide the experimental and theoretical tools needed for *directly* observing the orbital wavefunction. In Chapter 3, we choose topological insulators as our model system, as the weak correlation between electrons allows comparison between experiments and calculations. Interestingly, the strong spin-orbit coupling in topological insulators gives rise to a special type of wavefunction, which is a superposition of different orbitals coupled with the corresponding spin orientations. We term this new form the "spin-orbital texture", which in principle could also be found in other materials.

The collective excitation and dynamics near the Fermi energy usually result from broken symmetries, and are not related to the details of electron interactions. Following this argument, it might appear at first sight (and we will further the discussion in Chapter **??**) the orbital degree of freedom does not have an exclusive feature in spectroscopies. However, for such exotic low-energy features as pseudogap, there is no agreement which symmetry is broken. The orbital physics may offer new materials with similar low-energy dynamics but very different high-energy electron interactions. By comparing these material families, we will be able to determine many potentially

broken symmetries as irrelevant to the low energy feature. This in itself could mark a major advancement in a much debated area of research. In Chapter 5, we show the Mott-metal crossover in doped iridates shares some striking similarities with that of cuprates. By comparing the phase diagrams of these two systems, we could rule out pre-formed Cooper pairing and quantum criticality as responsible for these universal features during the Mott-metal crossover. Due to the complexity of Mott physics, we review in Chapter 4 some of the key theories and experimental findings.

The review Chapters 2 and 4 include the essential ingredients for the self-consistency of the thesis, without further details where review articles are available. For example, in Chapter 2, I introduce the concept of energy/momentum distribution curves and the Lorentzian fitting method, as these are the workhorses in real-world data analysis. I deliberately leave out discussions about the spectral function of the Fermi liquid, but instead comment on the essence of single-electron scattering rate. This is because a reader could learn the former from a review [8] or a book [9], while the latter is much less seen.

For an emerging field as complicated as orbital physics, there are many questions unanswered and many opportunities unexplored. We list two of them here, in the hope of inspiring further theoretical and experimental explorations:

First, it would be interesting to investigate whether/how orbital physics affects bulk properties in select materials. In the case of topological surface states, we will show in Chapter 3 that we could tune the photoelectron spin by controlling the orbital excitation using polarized photons. An intriguing future direction is to generate spin-polarized photocurrent with the same photon polarization. This requires precise control of competing electron-hole recombination processes in the bulk topological insulators [10], as well as improved spin-current detection at the edge of the sample.

Also, the orbital degree of freedom could form long-range orders [3, 11] and collective excitations [12, 13], just like spin and charge. So far elastic and inelastic scattering experiments are the main approaches to confirm the existence of orbital order. However, these spectroscopies rarely provide insight into the driving mechanism. Fermi surface nesting is often used to explain the

formation of charge order, and is a natural candidate in the case of orbital order. In this sense, ARPES is the perfect tool to study orbital order — it could be used to detect orbitals of different symmetries and to map the Fermi surface topology. We expect future work that combines ARPES and scattering experiments to explore orbital ordered materials.

Chapter 2

Imaging the Electrons as a Function of Binding Energy and Crystal Momentum

Angle-resolved photoemission spectroscopy (ARPES) proves an invaluable tool for directly observing both electronic structure and low-energy electron dynamics in the solid state and bears implications for electronic order including density-wave instabilities. Indeed, ARPES has demonstrated its unique ability in describing the phenomenology in many high-profile materials, including high T_C superconductors [8], few-layer graphenes [14, 15], and most recently the topological quantum phases of matter [5].

There has been a major increase in the number of ARPES research groups and endstations in the world, thanks in part to the implementation of new light sources (including synchrotrons, lasers and gaseous lamps) with improved energy resolution and also in part to the birth of the two-dimensional electron analyzer.

In this chapter, we present a very brief review on the principles of ARPES. We discuss how the electronic dispersion and scattering rate could be extracted from the ARPES spectra, as well as the modulation of ARPES intensity due to the orbital wavefunction symmetry. We review the design of the hemispherical analyzer in Appendix A.

2.1   Energy and Momentum Conservation in the Photoemission Process

The photoemission technique was born out of the photoelectric effect discovered by Hertz in 1887. When light strikes on a sample an electron can escape from the material by absorbing a quanta of light radiation. Einstein provided his critical explanation in 1905 that opened the door

to quantum mechanics. Each electron in the solid absorbs the energy of a photon[1] and escapes out by overcoming an energy barrier at the surface. Using energy conservation, the kinetic energy of a photoelectron is related to the energy of the electron in the solid via the following equation (also see Figure 2.1 **a**)

$$E_k = h\nu - \Phi - E_B \tag{2.1}$$

where Φ is the sample workfunction and E_B is the binding energy, i.e. the energy of the electron relative to the Fermi level. Thus the maximum kinetic energy of the photoelectron is simply $h\nu - \Phi$, as observed in the photoelectric effect in the late 19th century.

Moreover, the momentum parallel to the sample surface is conserved during photoemission, similar to the process of a ball bouncing off a wall in undergraduate mechanics. As we need to consider the momentum from both the electron and photon

$$k_{i,\parallel} + k_{h\nu} = k_{f,\parallel} \tag{2.2}$$

where $k_{h\nu}$ is the momentum of the photon; $k_{i,\parallel}$, $k_{f,\parallel}$ are the momentum of the electron in the solid and the photoelectron, respectively. In most of the ARPES experiments, the photon energy $h\nu \leq 100$eV and the momentum of photons are negligible. Thus we have

$$k_{i,\parallel} = k_{f,\parallel} = \frac{1}{\hbar}\sqrt{2m_e(h\nu - \Phi - E_B)}\sin\theta \tag{2.3}$$

where θ is the angle away from normal electron emission (Figure 2.1 **b**).

It appears at first sight that ARPES provides a genuine "snapshot" of the energy and momentum of an electron in the solid; and the photoemission spectrum is a mere "shift" of the electron density of states in the solid. However, we have so far overlooked the complexities during the photoemission process. For example, we have assumed the photoexcited electron interacts with neither the surface of the material nor other electrons in the solid on its way out. For a realistic modeling, if we want to treat photoemission (which includes photon absorption, electron removal (from the Fermi sea), and electron escape) as a one-step process, we would then need to consider

---

[1] Two-photon photoemission is possible, but with much reduced absorption probability.
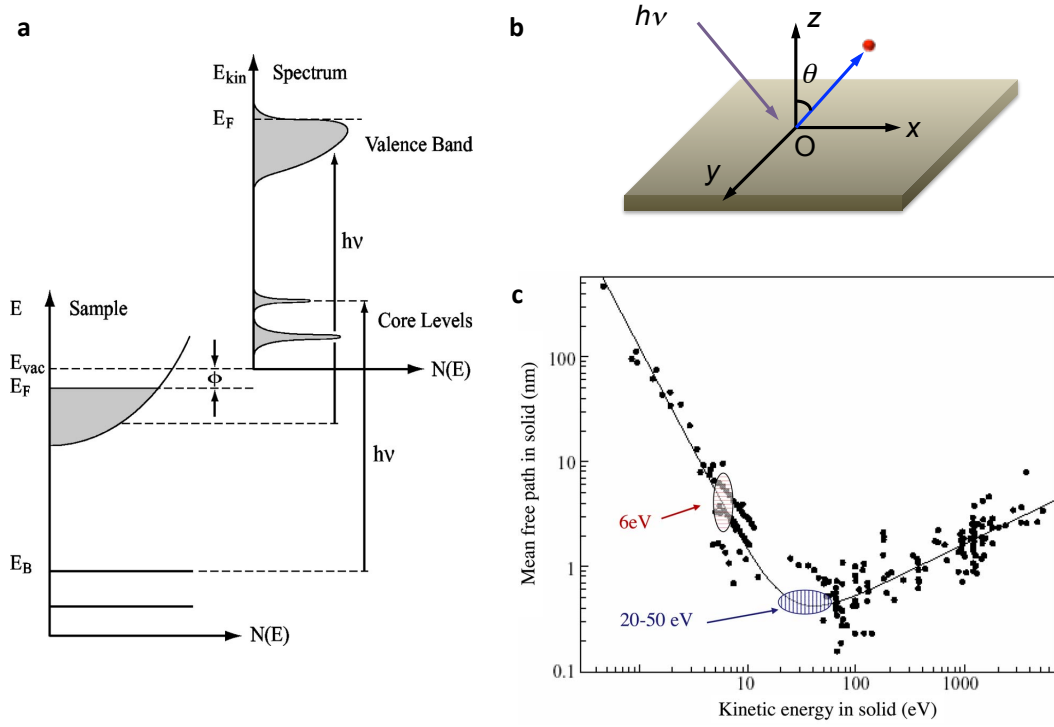
Figure 2.1: Energy and momentum conservation in the photoemission process. **a**. (reproduced from [9]) The electron in the solid absorbs the energy $h\nu$ of a photon, overcomes the workfunction Φ and converts itself into a photoelectron. **b**. The photoelectron (the solid red dot) travels out of the solid with an angle θ relative to the normal direction of the material. **c**. The relation between the mean free path and the kinetic energy of the photoelectron in the solid. Reproduced from [16], and data originally compiled in [17].

the above interactions, and this is a formidable job. An alternative is to adopt the following model that divides photoemission in three steps [18]:

(1) Optical excitation of the electron in the bulk.

(2) Travel of the excited electron to the surface.

(3) Escape of the photoelectron into vacuum.

Step (3) involves how photoelectrons transmit through the surface potential barrier and is relatively simple. We now focus on Steps (1) and (2) for the remainder of this section.

Step (1) is believed to contain intrinsic information about the electronic structure in the solid. An optical excitation would only occur when an electron is pumped from a filled state to an empty state. As electrons are indistinguishable particles that follows Pauli's exclusion principle, the excitation probability naturally requires information of all the electrons in the solid, both before and after the excitation. Specifically, using Fermi's golden rule, the transition probability from the initial to the final state

$$w = \frac{2\pi}{\hbar} |\langle \Psi_f^N | \mathcal{H}^{int} | \Psi_i^N \rangle|^2 \delta(E_f^N - E_i^N - h\nu) \tag{2.4}$$

with

$$\mathcal{H}^{int} = \frac{e\hbar}{mc} \vec{A} \cdot \vec{k} \tag{2.5}$$

where $|\Psi_{i,f}^N\rangle$ are the initial and final states for all N electrons and $E_{i,f}^N$ are the total energies for the initial and final state. $\vec{A}$ is the electromagnetic gauge of the photon field.

The initial state is straightforward, with all the states below the Fermi energy filled with electrons at 0K. For the final state, we would generally assume (which we call the "sudden approximation") the electron excited $h\nu$ above the hole does not talk with the rest of the filled states below the Fermi energy. This means we could write the N-particle final state as a product of the wavefunction of the excited electron and the wavefunction of the (yet to be relaxed) $N-1$ electrons.

$$|\Psi_f^N\rangle \propto \mathcal{A}[|\psi_f^{\vec{k}}\rangle \otimes |\Psi_f^{N-1}\rangle] \tag{2.6}$$

We use Ψ and ψ to denote the many-electron and single-electron wavefunctions, and $\mathcal{A}$ is an antisymmetric operator that properly antisymmetrizes the N-electron wave function. This way the transition probability is reduced to tracking the relaxation of the photo-hole (as we have only $N-1$ electrons below the Fermi energy now). One of the $N-1$ electrons would fill in the photohole (with the same energy-momentum relation as the ejected electron) during the relaxation, by scattering with other electrons or the lattice (thus providing information about the electron-electron and electron-phonon interactions, among others). Further discussions will be presented in Sections 2.2 and 2.3.

Step (2) could be approximated where electrons have an exponentially decaying probability of reaching the surface, and the characteristic length is called the escape depth of photoelectrons, which is significantly smaller than the probe depth of the incoming photon. Seah and Dench [17] compiled how the escape depth varies with photon energy, which we now refer to as the "universal curve". For photons $h\nu$ =20∼50eV, the escape depth is around 0.5nm and ARPES is said to be surface-sensitive. However, this is the photon range many of the ARPES works (including this thesis) are performed. The ARPES data collected at this photon energy range may or may not reflect the intrinsic properties of the bulk materials, depending on the details of the solid (e.g. sample cleave, dimensionality of the materials, etc.). For $h\nu$ <10eV we see a sharp increase in the electron escape depth. This photon energy range was not used in history, in part due to the lack of available light sources, and more importantly as the sudden approximation was assumed to be problematic for the low energy electrons. Koralek et al. [19] managed to prove that the sudden approximation still holds for photon energies down to 6eV and started the era in ARPES with better bulk sensitivity and higher resolution. It is to be noted that recently there have been successful demonstrations of ARPES experiments using soft and even hard X-rays with $h\nu$ larger than 500eV [20, 21]. In these experiments, the momentum of photons could no longer be ignored.

2.2   The ARPES Spectral Function

The measured ARPES intensity takes the general form [8]

$$I(\vec{k}, \omega) = |\langle \psi_f | \vec{A} \cdot \vec{p} | \psi_i \rangle|^2 f(\omega) A(\vec{k}, \omega) \tag{2.7}$$

where $f(\omega)$ is the Fermi function. $|\langle \psi_f | \vec{A} \cdot \vec{p} | \psi_i \rangle|^2$ is the dipole transition probability (often dubbed "the matrix element"). We will discuss the matrix element in Section 2.3. Here we focus on the $A(\vec{k}, \omega)$ term, which is the imaginary part of the single-electron Green's function (apart from a prefactor of $-1/\pi$)

$$G(\vec{k}, \omega) = \frac{1}{\omega - \epsilon_{\vec{k}} - \Sigma(\vec{k}, \omega)} \tag{2.8}$$

Thus

$$A(\vec{k}, \omega) = -\frac{1}{\pi} \frac{\Sigma''(\vec{k}, \omega)}{[\omega - \epsilon_{\vec{k}} - \Sigma'(\vec{k}, \omega)]^2 + [\Sigma''(\vec{k}, \omega)]^2} \tag{2.9}$$

with $\Sigma(\vec{k}, \omega) = \Sigma'(\vec{k}, \omega) + i\Sigma''(\vec{k}, \omega)$ being the electron self-energy. The real and imaginary parts of $\Sigma(\vec{k}, \omega)$ need to satisfy causality and are related by the Kramers-Kronig relations. $\epsilon_{\vec{k}}$ represents the electronic dispersion in the absence of electron correlation and is often referred to as the "bare dispersion". The $\omega_{\vec{k}} = \epsilon_{\vec{k}} + \Sigma'(\vec{k}, \omega)$ on the other hand is the "dressed" dispersion. The effect of the electron correlation is reflected not only in the single-electron lifetime (which is roughly the reciprocal of the imaginary part of the electron self-energy), but also in the measured band dispersion. The "dressed" dispersion corresponds to the renormalized, and usually heavier effective band mass of electrons or holes. We list the imaginary part $\Sigma''(\vec{k}, \omega)$ characteristic of the Fermi liquid (FL) and marginal Fermi liquid (MFL) [22], as these are often encountered in real materials

$$\Sigma''(\vec{k}, \omega)_{FL} \propto \omega^2 + (\pi k_B T)^2 \tag{2.10}$$

$$\Sigma''(\vec{k}, \omega)_{MFL} \propto \max(|\omega|, k_B T) \tag{2.11}$$

In Figure 2.2 we show a typical 2D energy-momentum intensity map. The measured/calculated ARPES spectra as a function of energy at a fixed momentum is called an energy-distribution curve
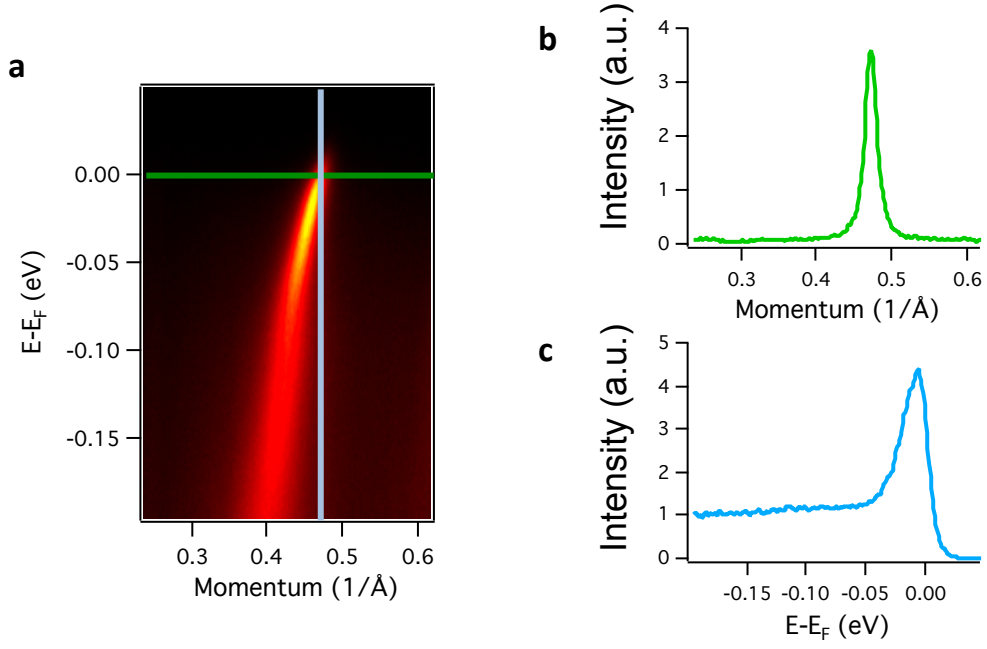
Figure 2.2: A typical 2D ARPES spectrum is presented in panel **a**. The data is taken from a optimally doped $Bi_2Sr_2CaCu_2O_{8+\delta}$ with a photon energy of 6eV. The energy (vertical axis) is measured relative to the Fermi level, with the negative side below the Fermi level. The momentum is along the analyzer slit and converted to $Å^{-1}$. **b**. The momentum distribution curve (MDC) and **c**. the energy distribution curve (EDC) taken along the solid green and blue lines in panel **a**, respectively.

(EDC). The momentum-distribution curve (MDC) could be defined similarly. In many realistic materials, with both strong and weak electron correlations, the electron self-energy strongly depends on the binding energy, but much less on the electron momentum. The MDC line shape usually fits well to a Lorentzian, in a wide range of energy close to the Fermi level, i.e.

$$A(\vec{k}, \omega) = -\frac{1}{\pi} \frac{\Sigma''(\omega)}{[\omega - \epsilon_{\vec{k}} - \Sigma'(\omega)]^2 + \Sigma''(\omega)^2} \tag{2.12}$$

The "dressed" dispersion $\epsilon_{\vec{k}} + \Sigma'(\omega)$ and the single-electron scattering rate $\Sigma''(\omega)$ could thus be obtained from the 2D energy-momentum intensity map as the centroid and the half width of the Lorentzian.

An important (but often less discussed) question is how much $\Sigma''(\omega)$ from ARPES measurements tells about the intrinsic correlations between electrons. We present the following two observations to justify the above question: First, the electron scattering rate obtained using Lorentzian fitting is often much larger than that from other (e.g. optical) spectroscopies [23]. Second, the MDC width varies from cleave to cleave for the same material, usually with a constant offset. This latter observation clearly suggests at least a portion of the scattering rate is contributed by the extrinsic elastic scattering off imperfections in the materials or on the surface. It is yet undetermined what this fraction would be.

If the intrinsic contribution accounts for a major fraction of $\Sigma''(\omega)$ from ARPES, the intrinsic spectral function (and accordingly the single-electron Green's function) would take a form closely resembling Eqn. (2.12). This puts very stringent constraints over the possible theories, especially for strongly correlated systems, and unfortunately not all the proposed spectral functions survive this test. One example involves the Anderson line shape [24] that successfully reproduced the asymmetric EDC in cuprates. However, the MDC from the same spectral function is also asymmetric, and does not agree with the measured MDC at all [25].

On the other hand, if the intrinsic contribution to $\Sigma''(\omega)$ is very small, then the constraints on the ARPES spectral function are relieved. Note the electron scattering rate reported in optical conductivity is indeed much smaller; and we should keep this possibility in mind.

Reber *et al.* have made a first attempt [23] at separating the intrinsic part of the electron scattering rate, using the tomographic density of states (TDoS) technique. However, the language and analysis technique used in [23] is so far exclusive to the cuprate system. We are not sure how the TDoS technique could be applied even in simple systems such as noble metals.

2.3   The Matrix Element Effect

The measured ARPES intensity has an overall transition probability termed "the matrix element" [8]

$$I \propto |\langle \psi_f | \vec{A} \cdot \vec{p} | \psi_i \rangle|^2 \tag{2.13}$$

Here $\vec{A}$ is the electromagnetic gauge and $\vec{p}$ is the electron momentum. $\vec{A}$ shares the same spatial mirror symmetry[2] as the electric field $\vec{E}$ of polarized photons. $|\psi_i\rangle$ and $|\psi_f\rangle$ are the electron wavefunction in the solid (or "the initial state") and the wavefunction of the photo-excited electron (or "the final state"), respectively. The initial state wavefunction contains information about the orbital characters of electrons, while the final state wavefunction is usually taken as a propagating plane wave along the photoelectron momentum $\vec{k}_f$.

In the presence of a linearly polarized electric field, only electronic states $|\psi_i\rangle$ of a particular symmetry will contribute to the measured ARPES intensity. This is because the matrix element includes integration across all spatial dimensions, so if the parity of the product $\langle \psi_f | \vec{A} \cdot \vec{p} | \psi_i \rangle$ is overall odd with respect to a particular mirror plane, the integration goes to zero and the ARPES intensity vanishes. We demonstrate the symmetry analysis by studying the two special cases in Figure 2.3. By "special", we delibrately put the Poynting vector of the light and the momentum of the initial ($\vec{k}_i$) and final ($\vec{k}_f$) states in the same plane[3] normal to the sample. The electric field normal to (along) this plane (with a pink color in Figure 2.3) is said to be s-polarized (p-polarized). This relative geometry between the light and the sample is not available in any random ARPES

---

[2] $\vec{A}$ is the spatial component of electromagnetic gauge, and is related to the electri field by $\vec{E} = -\partial \vec{A}/\partial t$. The electric potential ϕ is zero for the propagating electromagnetic wave in free space. In fact, $\vec{A}$ and $\vec{E}$ are parallel.

[3] In optics, the plane that contains both the Poynting vector and the sample normal is known as the plane of incidence.

setup.

For s polarized photons (Figure 2.3 **a**), the electric field $\vec{E}$ (and thus the gauge field $\vec{A}$) is odd with respect to the mirror plane. The in-plane momentum $\vec{k}_{\parallel} = \vec{k}_i$ and the final state wavefunction $|\psi_f\rangle$ are all even to the mirror plane. Thus for an orbital at $\vec{k}_i$ that is even with respect to the mirror plane, the overall mirror symmetry of $\langle \psi_f | \vec{A} \cdot \vec{p} | \psi_i \rangle$ is odd, and the matrix element vanishes. For the p polarized photons (Figure 2.3 **b**), the electric field $\vec{E}$ is even with respect to the mirror plane and the matrix element could be finite for the same orbital even relative to the mirror plane. The actual amplitude of the matrix element depends on the cross-section of the electric field with the spatial distribution of the orbital wavefunction. We could sum up the above symmetry analysis as

$$\langle \psi_f | \vec{A} \cdot \vec{p} | \psi_i \rangle = 0 \begin{cases} |\psi_i\rangle \text{ even} & \langle + | - | + \rangle \Rightarrow & \vec{A} \text{ odd}; \\ |\psi_i\rangle \text{ odd} & \langle + | + | - \rangle \Rightarrow & \vec{A} \text{ even}. \end{cases} \tag{2.14}$$

It is now evident that ARPES provides a unique opportunity to directly measure k-state orbital structures with different symmetries. The orbital character of the initial state wavefunction is mostly clearly shown when the ARPES intensity is suppressed along certain k directions. In practice, this requires careful arrangement of the geometry between the light and the sample. We usually choose the mirror plane to be along high symmetry directions of the Brillouin zone, so that the orbitals would have a defined mirror symmetry. We rotate the sample around the sample normal, till the Poynting vector of the light falls into the mirror plane. In principle, we could also choose the mirror plane to coincide with the photon plane of incidence so that the symmetry of $\vec{A}$ and $\vec{E}$ is fixed. This is particularly useful when higher symmetry is preserved in the system. We will adopt this latter method in Chapter 3 to analyze the orbital character of the Dirac surface state in topological insulators.

The matrix element generates an intensity modulation most prominent in the momentum space that may change with photon energy and polarization. For k-states away from the high-symmetry axis, a straightforward symmetry analysis similar to the one above is not available. Some of the complications in analyzing the matrix element over large regions in k-space include:

(1) The final state wavefunction: We have assumed the final state as a plane wave. For sufficiently high photon energies, usually at tens of eV, the final state is often in a quantum continuum above the Fermi energy and is close enough to a plane wave. For lower photon energies, this is not always the case.

(2) The k_z dependence of the initial state. For (quasi-)two-dimensional electron systems, while the band dispersion only depends weakly on k_z, there is no direct evidence that the k-space wavefunction depends on k_z as weakly. For example, in $Bi_2Sr_2CaCu_2O_{8+\delta}$ with two Cu-O planes, there are bonding and anti-bonding bands as a result of bilayer splitting. The relative intensity of these two (quasi-2D) bands are known to fluctuate with photon energies [26]. A possible explanation is that the bonding and anti-bonding wavefunctions have different symmetries along k_z.

(3) The spatial distribution of the initial state. The so-called surface states are not truly two-dimensional, and usually extend a few atomic layers into the bulk, on a length scale comparable to the electron mean free path in ARPES. A photoelectron could initiate from different atomic layers, giving rise to a quantum interference between these electron path. At a fixed (k_x, k_y) point, the interference between adjacent atomic layers has a prefactor $e^{ik_{f,z}c}$ with $k_{f,z}$ being the k_z momentum of the photoelectron and c the interlayer distance. Zhu *et al.* proposed [27] how this mechanism may lead to pronounced intensity modulations in the topological surface states.

Our list above is certainly not exhaustive. The matrix element is so complicated that it remains largely a "black box" in ARPES experiments. Deciphering the matrix element has been relying heavily on first-principles calculations [28, 29]. The danger of this approach is that these calculations hardly pinpoint the exact origin of the intensity modulation, and the calculation could be affected by many details in the materials.

The dependence of matrix elements on the linear/circular photon polarization is commonly referred to as the linear/circular dichroism. While these terms offer a concise phenomenological description, they do not provide further physical insight. The circular dichroism in topological insulators [30], copper [31] and cuprates [32] may come from very different origins. Thus we avoid using the name linear/circular dichroism throughout the thesis.
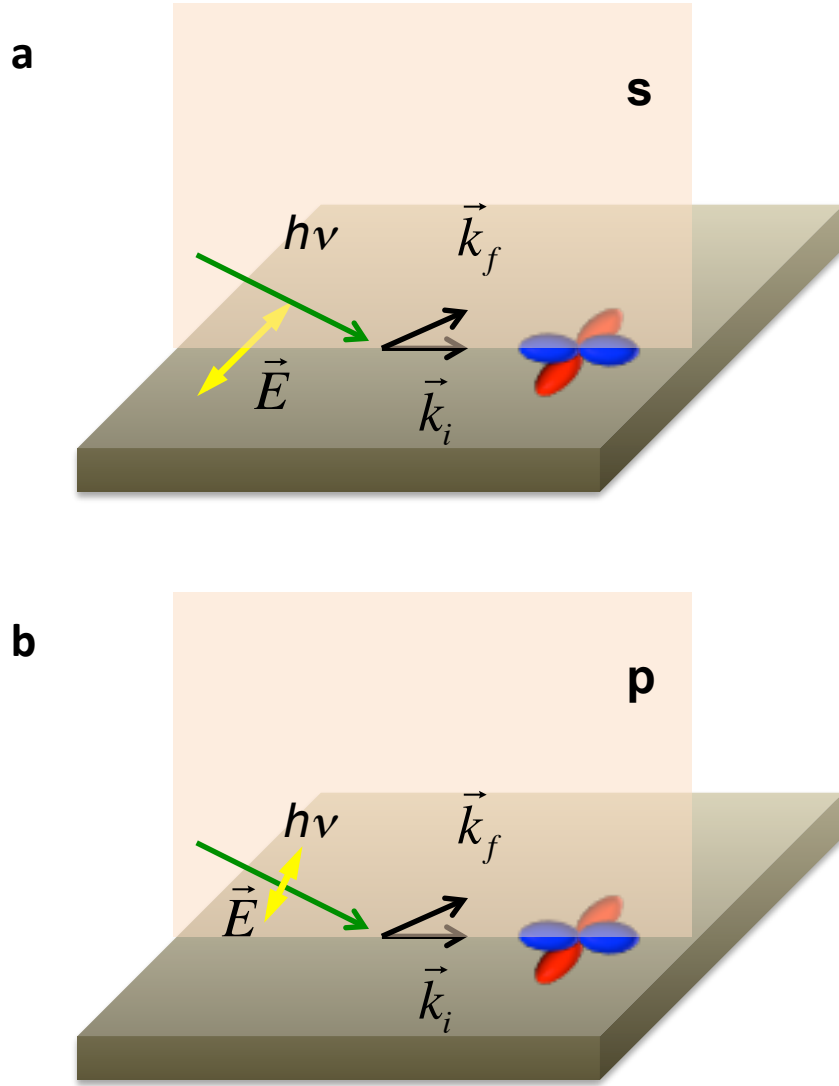
Figure 2.3: A demonstration of matrix element analysis. The matrix element $|\langle \psi_f | \vec{A} \cdot \vec{p} | \psi_i \rangle|^2$ is zero for the geometry in the panel **a** but finite in **b**. The photons are s and p polarized in panels **a** and **b** respectively, with the electric fields denoted by the yellow double arrows. $\vec{k}_i$ and $\vec{k}_f$ are the initial and final state momentum. The mirror plane is drawn in pink and contains the Poynting vector of the light, as well as $\vec{k}_i$ and $\vec{k}_f$. The orbital wavefunction of interest is even relative to the mirror plane, with the red/blue colors marking the relative phases.

Chapter 3

Mapping the Spin-Orbital Texture in Topological Phases of Matter

The prediction and discovery of the topological phases of matter, including but not limited to topological insulators (TIs) [33, 34, 5, 35] and topological crystalline insulators (TCIs) [36, 37], have proven to be one of the major advances in condensed matter physics in the last decade. The "topological" description of the solid state succeeds the integer and fractional Quantum Hall effects (QHE) as new members of the "quantum-order" [38] family.

In this chapter, we focus on the topological insulators. The criteria that guarantee the presence of quantum orders [39, 40, 41] do not depend on the details of the materials, which explains why the topological phases are often regarded as "symmetry-protected". Most of the experimentally-confirmed topological materials are "classical" semiconductors or alloys [42], with weak electron correlations. It would appear that theories and first-principles calculations [43, 44, 45] have so far provided a nearly-perfect description of the topological state and dominated the progress of experiments. The work presented in this chapter suggests otherwise. Exploiting the Orbital-Selective and Spin-Resolved ARPES (OS-SARPES), we show the topological surface state has a spin-orbital-coupled wavefunction (or "spin-orbital texture"). Also, the topological wavefunction determined from ARPES is *asymmetric* relative to the Dirac point (DP). Both observations are confirmed in the first-principles calculations, by directly collecting the spin and orbital information from the calculated surface state wavefunction. In a sense, our designed ARPES experiments plays a vital role and guides the theoretical search for these previously "hidden" facts.

The "spin-orbital texture" description of the topological surface state is in sharp contrast

to the prevailing "spin texture". This seemingly minor deviation comes with observable physical consequences, and may affect the manipulation of the electron spin in future quantum computation schemes and spintronics.

We start this chapter with an introduction to the topological insulators (following in part the elegant discussion in [5]), and analyze why the "spin texture" does not provide a complete description of the topological surface state. Then we map the orbital wavefunction of the topological surface state, as well as the spin chirality coupled to each orbital component. We show at the end of the chapter how photon polarizations control the photoelectron spin polarization, as a direct result of the spin-orbital texture.

3.1   Classifying Insulators By the Bulk Time-Reversal Symmetry

Topology starts as a mathematical concept, describing the invariance of geometrical shapes under *continuous* deformations. By "continuous" we allow deformations that bend/stretch the object under consideration, while tearing or gluing is not permitted. A famous joke is that a topologist cannot distinguish between a coffee mug and a donut — the number of "holes" for both of them being one. The condensed matter community has been utilizing the concept of topology for decades, a famous example being the non-Abelian statistics in lower dimensional systems [46].

Recently, Kane, Moore *et al.* [39, 40, 41] applied the "topological" perspective to the classification of band insulators, and raised the following question: are all band insulators topologically equivalent? In other words, could we transform one band insulator into anther by continuously "stretching" the band structure?

At first look, the answer seems obvious: we could certainly deform one band insulator (or semiconductor) into another, as long as the Fermi level still separates the empty and filled states and the band gap remains finite. However, after examining the time-reversal symmetry of the bulk bands, Kane, Moore *et al.* decided there are actually two subgroups of band insulators,

characterized by a time-reversal invariant, called the $\mathcal{Z}_2$ number

$$(-1)^{\gamma_S} = \prod_i \delta(\Gamma_i) \tag{3.1}$$

where $\delta(\Gamma_i) = \pm 1$ marks the even $(\delta(\Gamma_i) = 1)$/odd $(\delta(\Gamma_i) = -1)$ time-reversal symmetry at an independent time-reversal invariant momentum Γ_i. There are 4 Γ_i's in the two-dimensional Brillouin zone: $(0, 0)$, $(0, \pi)$, $(\pi, 0)$, (π, π); and there are 8 Γ_i's in a three-dimensional Brillouin zone. With Eqn. (3.1) we divide band insulators into two subgroups: $(-1)^{\gamma_S} = 1$, the regular band insulators; and $(-1)^{\gamma_S} = -1$ the topological insulators (TIs). There is no continuous deformation between the two subgroups, as the "stretch" operation should not change the time-reversal symmetry.

Now we show why these time-reversal invariant momenta are special. Kramers theorem dictates for materials that are time-reversal symmetric, electronic states $|\vec{k}, \sigma\rangle_n$ and $|-\vec{k}, -\sigma\rangle_n$ (called a Kramers pair, with n being the band index) are degenerate in energy, i.e. $E_n(\vec{k}, \sigma) = E_n(-\vec{k}, -\sigma)$. Some high symmetry k-points Γ_i's are invariant under the time-reversal operation. For example, in a two-dimensional Brillouin zone, $(0, \pi)$ and its time-reversal counterpart $(0, -\pi)$ are connected by a reciprocal lattice vector $(0, 2\pi)$ and therefore equivalent. At these special k-points, we have $E_n(\Gamma_i, \sigma) = E_n(\Gamma_i, -\sigma)$. This means electronic states at Γ_i's are required to be doubly degenerate and filled with both spin-"up"[1] and spin-"down" electrons. In the rest of the Brillouin zone, the states $|\vec{k}, \sigma\rangle_n$ and $|\vec{k}, -\sigma\rangle_n$ could (but does not have to) have a finite energy splitting, with each state singly-occupied. Microscopically, this energy splitting often comes from spin-orbit coupling, which preserves the global time-reversal symmetry. A consequence of the energy splitting is that the net spin current from the "down" spin and the "up" spin at the same momentum does not cancel. Thus it is natural some of the distinguishing features of the newly discovered TIs relate to the spin degree of freedom, as we will show later in this section.

The global band structure could be thought of as connecting singly filled bands (with polarized spins) between Γ_i's, as long as these singly filled bands meet at Γ_i (ensuring the 2-fold degeneracy).

---

[1] As the time-reversal symmetry is not explicitly broken, the bulk insulator is non-magnetic and the spin up/down axes may not be well-defined. Still, for a given k-point, we could call one of the state spin up, and the other spin down, both having the same band index.

The even/odd symmetry at each Γ_i depicts how the spin "up" and "down" states split at the same momentum $\vec{k}$ once away from Γ_i. For a trivial band insulator with 2-fold degeneracy throughout the Brillouin zone, every $\delta(\Gamma_i) = 1$. Only band insulators with an even number of $\delta(\Gamma_i) = -1$ is topologically identical to the trivial band insulator.

One of the most remarkable properties in a TI is a spin-polarized surface state between the topological insulator and a trivial band insulator (or the vacuum which is also topologically trivial). For the topological invariant to change at the interface, the energy gap has to vanish, and low energy states will appear where the energy gap passes through zero.

We show the surface band dispersions between two high symmetry k-points $\Gamma_a = 0$ and $\Gamma_b = \pi$ for both insulators in Figure 3.1 **a** and **b**. The dispersion in the other half of the Brillouin zone (in between $-\pi$ and 0) is a mirror reflection of the dispersions shown here. The surface bands have to be two-fold degenerate at momenta 0 and π due to the time reversal symmetry. Away from these k-points, the degeneracy could be removed, e.g. by a spin-orbit interaction. Note we could continuously deform the surface bands in a trivial band insulator (but not in a TI) till they were immersed in the bulk bands (the shaded region). Also the surface states in the trivial and topological insulators have even and odd numbers of crossings with the Fermi energy, respectively. The surface state in two- and three-dimensional TIs are plotted in Figure 3.1 **c** and **d**. We will focus on the three-dimensional TIs for the rest of this chapter.

In both cases, there are singly-occupied (except at Γ), spin-polarized dispersions crossing at the Γ point. No gap opens, as the electrons are protected from back scattering. In a three-dimensional TI, the linear surface bands form a two-dimensional Dirac cone and were confirmed in ARPES experiments [47, 48]. The topological insulators have since attracted widespread interest, for their potential applications in quantum computation and spintronics [5, 49, 46]. Also, TIs may become the workbench to realize some of the dream particles, e.g. the magnetic monople [50] and Majorana fermions [51].
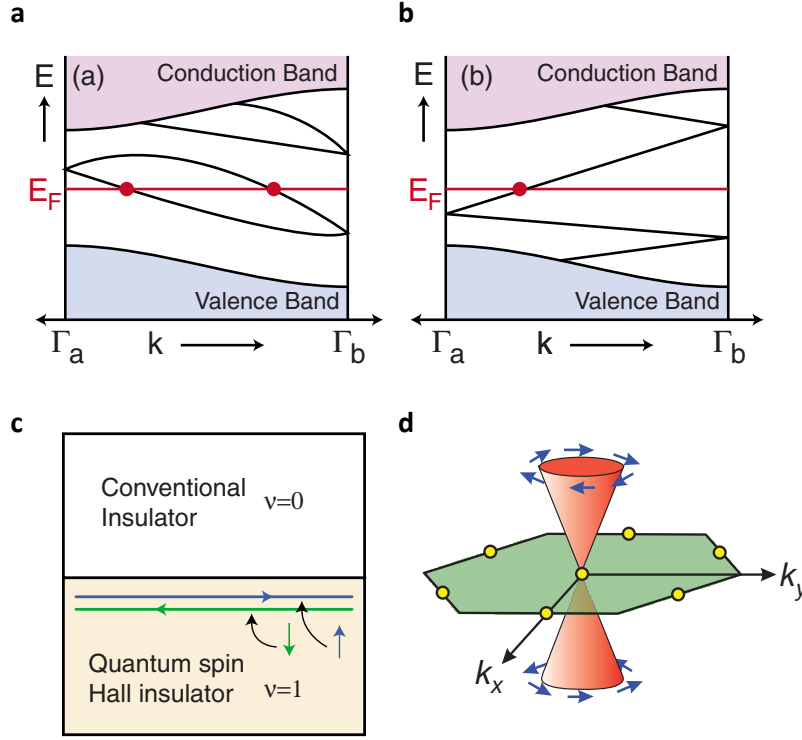
Figure 3.1: Bulk insulator coated by a surface state with net spin current and linear dispersion. **a-b**. (reproduced from [5]) Band dispersion between two boundary Kramers degenerate points $\Gamma_a = 0$ and $\Gamma_b = \pi$. The shaded areas are the bulk conduction and valence bands, while the lines are the surface bands. The surface states in the regular (panel **a**) and topological (panel **b**) insulators have even and odd numbers of intersections with the Fermi energy, respectively. **c**. (reproduced from [5]) The two-dimensional TI (also called quantum spin Hall insulator) has a net spin current at the TI-vacuum interface. **d**. (reproduced from [47]) The prevailing cartoon of the topological surface state at the Γ point. For the three-dimensional TI, the surface state has a massless linear dispersion (called a Dirac cone) at Γ. The electron at each k-point on the Dirac cone is non-degenerate (except at Γ) with chiral spin locked to the momentum. The spin is left-handed above the Dirac point and right-handed below the Dirac Point.

3.2 Beyond the "Standard" Spin Texture of the Dirac Surface State

Mapping the topological wavefunction is an indispensable yet missing piece in the grand "jigsaw puzzle" of TIs. On the one hand, the existence of the topological surface state is determined by tracking the time reversal symmetry of the bulk bands [39, 40, 41], which by itself does not provide a description of the surface state. On the other hand, future applications of TIs in the quantum computation will require *direct* manipulation of the topological wavefunction [5, 49, 46]. Also, from a historical perspective, the fractional Quantum Hall Effect, as the first case of quantum order, was only understood after the discovery of the Laughlin wavefunction [52].

The topological surface state features a linear Dirac-cone-like dispersion near the center of the Brillouin zone, occupied with spin-polarized electrons. A widely-accepted (but flawed) picture of the Dirac surface state is plotted in Figure 3.1 **d**, with the following features:

- In the vicinity of the DP, the spin lies in the k_x-O-k_y plane;

- The spin chirality is left-handed above the DP and right-handed below;

- In the ideal case, the Dirac electrons are 100% polarized.

These features could be justified by considering the time-reversal and real-space symmetries of the surface state itself, without information from the bulk bands. The time-reversal symmetry requires for a Kramer's pair at $\pm\vec{k}$, the spin orientations (if well-defined on a Bloch sphere) are opposite. Moreover, very near the DP, the Dirac cone is almost isotropic, and thus has infinitesimal rotation symmetry. This requires the spin on the Dirac cone to lie in the k_x-O-k_y plane. In real materials [45], there may still be a non-zero out-of-plane spin component, which appears further away from the DP. The s_z component has "nodes" that follow the crystalline symmetry, and often accompanies deviation of the constant energy surface from a perfect circle [53].

We could use the minimal Hamiltonian (in the form of the Rashba interaction) below [54] to describe the Dirac cone dispersion in a three-dimensional TI with a two-dimensional surface state

$$\mathcal{H} \propto \sigma_x k_y - \sigma_y k_x \tag{3.2}$$

where $\sigma_{x,y}$ are the Pauli matrices. Solving Eqn.(3.2) as a 2×2 matrix immediately leads to the linear dispersion and the chiral spin texture in Figure 3.1 **d**. The handedness of the spin texture comes from the positive prefactor [54]. Note in the above analysis, we only consider the momentum-spin locking of the Dirac electrons, and there is no information about the orbital degree of freedom. Choosing $\hat{z}$ normal to the layered surface of the material, we have

$$\mathcal{H} \propto \hat{z} \cdot (\vec{\sigma} \times \vec{k}) \propto -\vec{\sigma} \cdot \vec{L} \tag{3.3}$$

with $\vec{L} = \hat{z} \times \hbar\vec{k}$ being the orbital-angular momentum of electrons. Park *et al.* suggested [55, 56] the orbital-angular momentum as defined above is locked to the electron momentum in the opposite direction to the spin.

It may appear the minimal model presented a "perfect" cartoon of the Dirac surface state. However, when we solve for the Dirac wavefunction, we need to identify the basis set of the 2×2 matrix. For this, we consider the real-world prototype topological insulators Bi_2X_3 (X=Se, Te). The crystal structure and the calculated band dispersion of Bi_2Se_3 are displayed in Figure 3.2. For Bi_2X_3 (X=Se, Te), the bulk conduction bands and valence bands (that invert due to the spin-orbit coupling) come from the p_z orbitals of Bi and Se/Te atoms [43]. It is natural to assume the surface state that "connects" the bulk p_z bands would also have a p_z character, especially as the bulk bands originating from the in-plane p_x and p_y orbitals are well-separated from the p_z orbitals by the strong crystal field effects. The assumption that the surface state has only p_z-character was adopted in [43], among other references, the validity of which was never discussed.

We now return to the effective Hamiltonian in Eqn.(3.3). The orbital angular momentum $\vec{L}$ has been proposed as being closely tied to the local spin-orbit coupling of the constituent atoms[2] [55, 56]. As we pointed out in Section 3.1, the spin-orbit coupling plays a key role in the generation of non-spin-degenerate surface states. In fact, the spin-orbit coupling accounts for the band inversion in the known topological insulators [5, 42]. Now consider the role of the local/atomic version of

---

[2] Ref. [55, 56] made some interesting claims how $\vec{L}$ defined for the two-dimensional Dirac electrons are connected with the local spin-orbit coupling. How these two versions of the orbital angular momentum are directly related awaits further theoretical study.
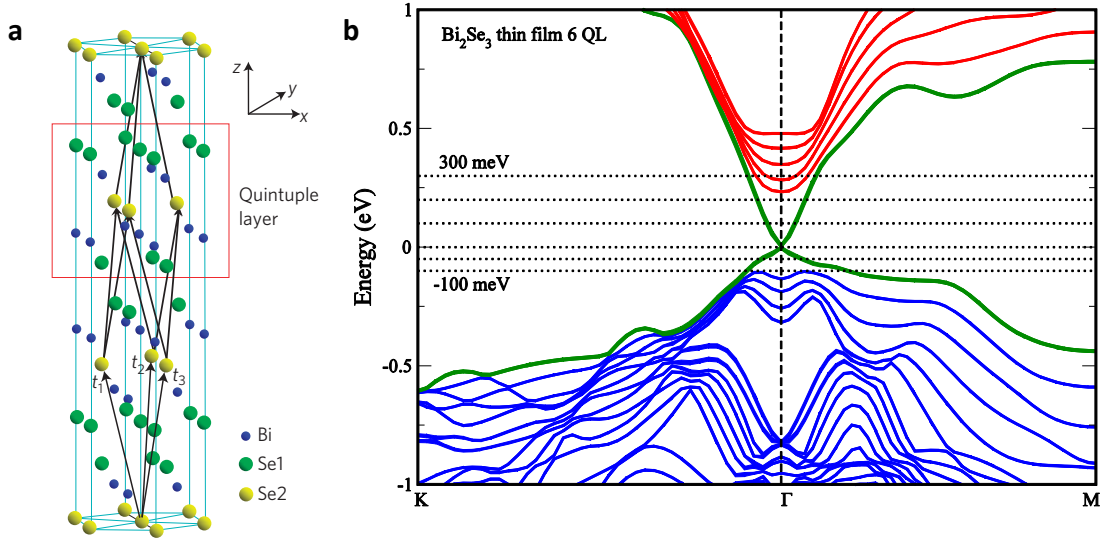
Figure 3.2: The crystal structure (panel **a**) and calculated band dispersion (panel **b**) of Bi_2Se_3. In panel **a** (reproduced from [43]), the three primitive lattice vectors are denoted as $t_{1,2,3}$. A quintuple layer is indicated by the red square. **b**. The band structure comes from a 6 quintuple layer slab of Bi_2Se_3. All energies are relative to the DP. The Dirac surface band is represented with the solid green line. The red and blue solid lines are the bulk conduction bands and valence bands, respectively.
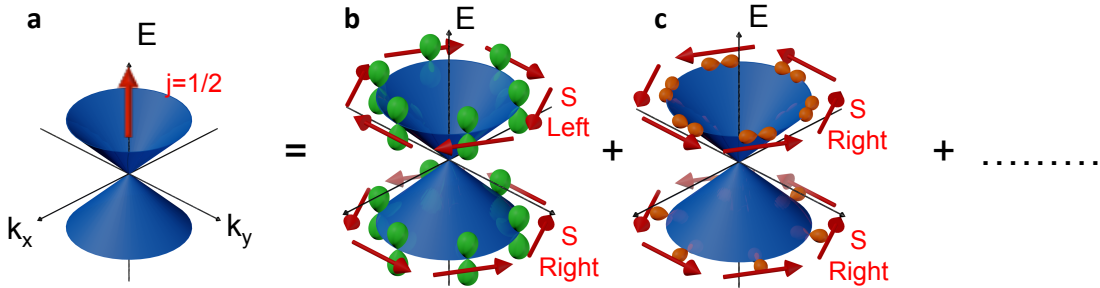
Figure 3.3: **a**. Cartoon drawing of the coupled spin-orbital texture, with the z component of the total angular momentum j_z conserved on both sides of the Dirac point. Panels **b** and **c** are the leading terms in the Dirac wavefunction. The p_z orbital coupled to the left-handed spin above the DP and right handed spin below DP. Above the DP, the majority in-plane orbital component is tangential to the constant energy surface and couples to a right-handed spin texture. Below the DP, the majority in-plane orbital component is radial to the constant energy surface and also couples to a right-handed spin texture.

the orbital angular momentum operator $\vec{L}$. $\vec{L}$ explicitly mixes the in-plane $p_{x,y}$ states with the p_z orbitals, e.g. $L_x|p_z\rangle \rightarrow |p_y\rangle$. Thus the $|p_z,\uparrow/\downarrow\rangle$ states used in [43] do not constitute a *complete* basis set of the Dirac wavefunction. Instead, the complete minimal Hamiltonian is a 6×6 matrix that includes two spin states from each of the three orthogonal p orbitals. To investigate which features of the Dirac state the "effective model" captures we now need to check both the spin and orbital properties of the electronic wavefunction. Indeed the once-missing in-plane states exhibit novel and unexpected physics.

The need for the orbital degree of freedom in the Dirac wavefunction could also be illustrated by considering the quantum invariant of the system. Since strong spin-orbit coupling is inherent in all the known TIs, spin is not a good quantum number of the Dirac state. Instead, the total angular momentum j_z, which includes both the spin and orbital degrees of freedom, is conserved, due to the infinitesimal rotation symmtry near the DP. The question at hand is how spin and orbitals couple and contribute to j_z.

As we will show in Section 3.3 and 3.4, the Dirac wavefunction has a spin-orbital coupled wavefunction — a superposition of orbital wavefunctions coupled with the corresponding spin textures (Figure 3.3). The in-plane orbital wavefunction is asymmetric relative to the DP, switching gradually from being predominantly tangential to the k-space constant energy surfaces above the DP, to being predominantly radial to them below the DP. The in-plane p orbital tangential to the constant energy surface couples to the right-handed spin texture, while the p_z orbital and the in-plane radial p orbital have the standard left-handed spin texture. How the spin and orbitals couple is a direct manifestation of conserved total angular momentum j_z.

Note within the minimal model in Eqn.(3.3) (even considering the spin-orbital coupled wavefunction), the orbital wavefunction in the vicinity of the DP is expected to be symmetric. It could be shown (see the Supplementary Online Materials in Ref. [57]) that if the wavefunction $|k,s\rangle$ is an eigenfunction of the model Hamiltonian, with an eigenvalue of E > 0, then $|k,s'\rangle = \sigma_z|k,s\rangle$ is also an eigenfunction of the model Hamiltonian, with an eigenvalue of $-$E. The discovery of an asymmetric orbital wavefunction is therefore highly unusual.

3.3   Mapping the Orbital Wavefunction of the Dirac Surface States

Angle-Resolved Photoemission Spectroscopy (ARPES) provides a unique opportunity to directly measure k-state orbital structures with different symmetries, via the matrix element effect. While a detailed introduction is presented in Chapter 2, we briefly review some of the key points here. The measured ARPES intensity $I \propto |\langle \psi_f | \vec{A} \cdot \vec{p} | \psi_i \rangle|^2$ where $\vec{A}$ is the electromagnetic gauge and $\vec{p}$ is the electron momentum. $|\psi_i\rangle$ and $|\psi_f\rangle$ represent the electron wavefunction in the solid (hereafter "the initial state") and the wavefunction of the photo-excited electron (hereafter "the final state"), respectively. By properly arranging the experimental geometry, it is often possible to adjust the parity of $|\psi_f\rangle$ and $\vec{A} \cdot \vec{p}$ such that the ARPES intensity vanishes in a certain direction, thus determining the parity (symmetry) of the initial state wavefunction $|\psi_i\rangle$.

We carefully design a set of orbital-selective ARPES experiments on Bi_2Se_3 to determine the orbital symmetry of the Dirac surface state. Data has been taken both from Bi_2Se_3 thin films and bulk samples and have shown consistent results. The Bi_2Se_3 thin films were prepared using a two-step growth method, as describe in Ref. [58], and were protected with a Se overlayer after growth, and decapped in the preparation chamber, with a base pressure better than 1×10^{-9} Torr during decapping and then transferred into the analysis chamber while maintaining ultra-high vacuum conditions throughout. The bulk samples were cleaved in situ at 50K with a base pressure better than 5×10^{-11} Torr.

The ARPES experiments were performed at Beamline 10.0.1 (HERS) of the Advanced Light Source, LBL. We show a photo of the beamline in Figure 3.4. The incident photons come at a glancing angle $\sim 7°$ to the sample plane and can have either p-polarization (photon electric field vector drawn with yellow arrow in Figure 3.5 **a**, in the orange-colored plane of incidence) or s-polarization (E field perpendicular to the plane of incidence). These possibilities are illustrated in Figure 3.5 **a**. In both configurations, only the electron analyzer is rotated to collect data, so that the relative angles between the sample coordinate axes and the photon beam coordinates (polarization and Poynting or incident vector) remain unchanged.
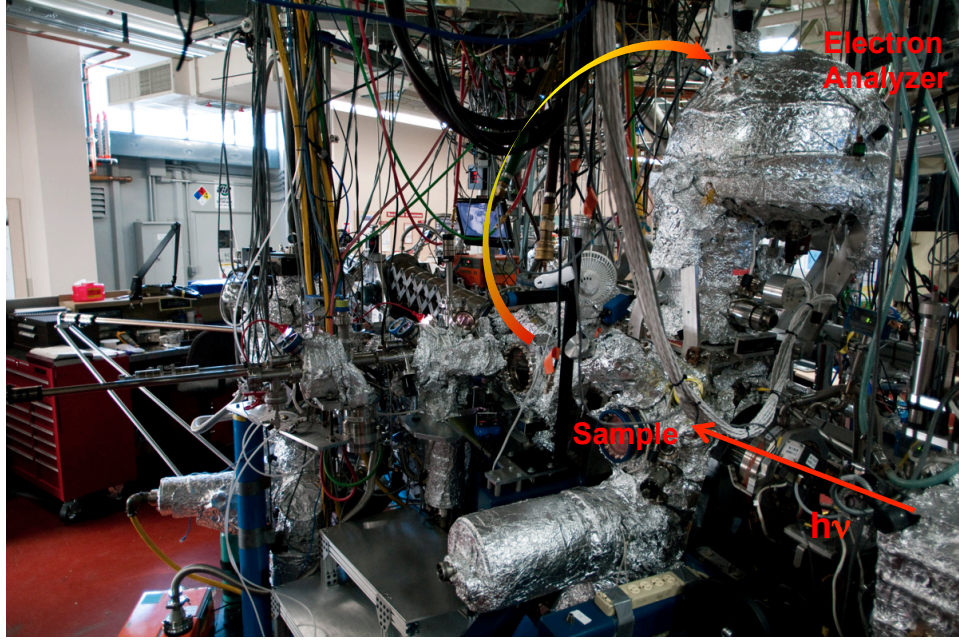
Figure 3.4: The ARPES endstation at Beamline 10.0.1 (HERS) of the Advanced Light Source (ALS), Lawrence Berkeley National Laboratory. Photo courtesy of Sung-Kwan Mo at ALS. The X-ray synchrotron beams comes in along the red arrow, parallel to the experimental ground. The electron analyzer could be rotated around the axis of the incoming beam. The polarization of the beam is fixed to be linear and horizontal (parallel to the ground). For sample facing up (towards the analyer in the geometry in the photo), the sample sees the s polarization. To get p polarization, we rotate sample around the manipulator axis by 90°. This is equivalent to rotating the photon polarization by 90° while keeping the sample intact. In both the s and p polarizations, the electron analyzer is rotated to collect ARPES data.
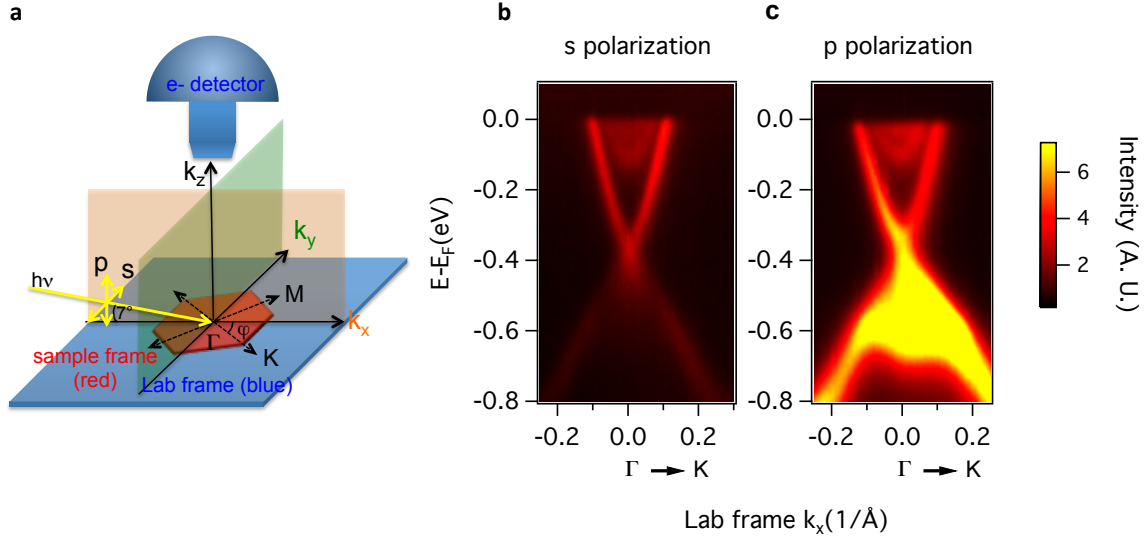
Figure 3.5: ARPES energy-momentum intensity plots at the Γ point for s and p photon polarizations. Panel **a** shows the experimental configuration, where the sample frame is shown in red and the lab frame (which contains the electron detector) in blue. The sample axes can be rotated by the angle φ relative to the lab frame, though the normal of the sample and lab frame always stay aligned. The incident photon beam makes an angle of $\sim 7°$ relative to the lab (and sample) planes and has varying polarizations ranging from full s (E field parallel to the sample plane) to full p (E field in the orange kx-kz plane). **b** and **c** are ARPES cuts along the Γ-K direction of Bi_2Se_3 taken with s and p polarization, respectively, with the sample Γ-K axis lying in the k_x lab frame direction.

As discussed in Section 3.2, to a very good approximation we only need to consider the p-like wavefunctions for the Dirac states and bulk bands nearest to the DP. The E field of p-polarization points out-of-plane. Therefore it leads to a strong ARPES cross-section for the out-of-plane p_z orbitals and a weak cross section for the in-plane orbitals. In contrast, s-polarization data has a strong cross-section for the in-plane orbitals and a weak cross-section for the out-of-plane orbitals. This is observed in the energy-momentum intensity plot along the Γ-K cut of Bi_2Se_3, taken with s and p-polarization respectively (Figure 3.5 **b** and **c**). The ARPES intensity of the Dirac cone using p-polarization is ∼2 times stronger than using s-polarization, confirming the Dirac states have a large p_z component and non-negligible contribution from in-plane states. In addition to the surface states that make up the Dirac cone, the bulk valence band can also be observed in the interior of the Dirac cone below the DP using p-polarization. This indicates that the bulk valence band has a major p_z component, consistent with Ref. [43, 54].

Figure 3.6 **a** shows constant energy surfaces (CESs) of Bi_2Se_3 for different energies relative to the DP (left to right) and for both polarizations (s and p as marked on the right of the panel). The bottom row shows data from p-polarization, mainly made up of the p_z states. These are seen to be almost uniform around the constant energy surfaces for all energy cuts. In contrast, the data taken with s-polarization has drastic intensity changes around the constant energy surfaces. In particular the data above the DP (left 2 columns) both show vanishing spectral weight parallel to the electric field, while the data below the DP (right 2 columns) shows suppressed spectral weight normal to the electric field. To determine whether this weight distribution is related to a specific crystalline orientation (sample frame) or relative to the photon field (lab frame), we rotated the sample crystalline axes in multiple 5° steps of the angle φ (defined as in Figure 3.5 **a**) about the sample normal while keeping all other experimental parameters the same. These data, shown in Figure 3.6 **b** from left to right columns are almost identical with sample rotation, illustrating that this pattern is not due to any particular arrangement relative to the 6-fold crystalline axes but is more general. Moreover, the intensity distribution on the CES does not reply on any special property of the final state wavefunction $|\psi_f\rangle$. This is confirmed by varying the incident photon

	Γ-k_A mirror plane	$\langle\Psi_f|A{\cdot}p|\Psi_i\rangle$	Γ-k_B mirror plane
p-polarization	$\langle e|e|e\rangle \rightarrow |\Psi_i\rangle = p_x{}^*/p_z$		$\langle e|e|e\rangle \rightarrow |\Psi_i\rangle = p_y{}^*/p_z$
s-polarization	$\langle e|o|o\rangle \rightarrow |\Psi_i\rangle = p_y$		$\langle e|e|e\rangle \rightarrow |\Psi_i\rangle = p_x{}^*/p_z$

Table 3.1: Initial state orbital wavefunctions with non-vanishing ARPES spectral weight. The table is shown across two key mirror planes (see Figure 3.5 for relevant mirror planes). For $*$ marked states, the spectral weight is much smaller with the momentum / photon polarization combination than the one without the $*$; but they are not symmetry forbidden.

energy so that different final states are chosen. The constant energy surface intensity plots 200meV above the Dirac point for different photon energies from Bi_2Se_3 are shown in Figure 3.7.

We now use a symmetry analysis across various mirror planes to disentangle the symmetries of the various in-plane states that contribute, requiring us to only consider s-polarized photons. A helpful mirror plane to consider is the one defined by the sample surface normal and the photon Poynting vector (orange plane in Figure 3.5 **a**, in the k_x direction in the lab frame, and shown as the orange lines in Figure 3.6 **c**). Relative to this k_x-k_z lab-based mirror plane the s-polarized photon field E has an odd parity, while it has an even parity relative to the green k_y-k_z mirror plane. The free-electron final state $|\psi_f\rangle$ is even with respect to both these mirror planes. As labeled in Figure 3.6 **c**, this constrains the initial state wavefunctions $|\psi_i\rangle$ to have a certain parity with respect to these mirror planes, so that the ARPES intensity will vanish in the correct symmetry locations if the overall parity of the matrix element is odd. Above the DP, the in-plane states along the green Γ-k_y line, and thus the initial state $|\psi_i\rangle$, must have odd symmetry with respect to this mirror plane (3.6 **c**, top) for a zero matrix element. Similarly, for the in-plane states below the DP, there is vanishing weight along the orange Γ-k_x line and so the initial state is even with respect to this mirror plane (3.6 **c**, bottom). Along k_x above DP and along k_y below the DP, there is strong spectral weight, the matrix elements are overall even, and the initial state parities can similarly be determined. Note neither of these mirror planes are necessarily along any of the high symmetry

Figure 3.6: Deducing the orbital texture from constant energy surface intensity plots. All the data were taken from Bi$_2$Se$_3$. **a** The experimental constant energy surface intensity plot at different energies relative to the DP. The Γ-K direction of Bi$_2$Se$_3$ is parallel to the lab k_x. **b**. s-polarization experimental constant energy surface intensity plots as a function of in-plane sample orientation and energies relative to the DP, in 5° steps, from left to right columns. The axes shown are the crystal axes that are attached to the lattice orientation. The lab frame direction is unchanged as the sample is rotated, and all energy labels are relative to the Dirac point. **c**. Symmetry analysis of p orbitals across the orange k_x-k_z and green k_y-k_z lab-frame mirror planes (see also Figure 3.5 **a**). The free electron final state $|\psi_f\rangle$ is even in all cases, while the s-polarized photon field $\vec{A} \cdot \vec{p}$ is odd with respect to the orange k_x-k_z mirror plane and even with respect to the green k_y-k_z mirror plane. As illustrated, this gives strong or weak intensity for initial states $|\psi_i\rangle$ with symmetry that have the total matrix element even or odd, respectively. Since this result is independent of sample rotation (panel **b**), it implies an in-plane tangential orbital texture above the DP and a radial one below (see Figure 3.3).
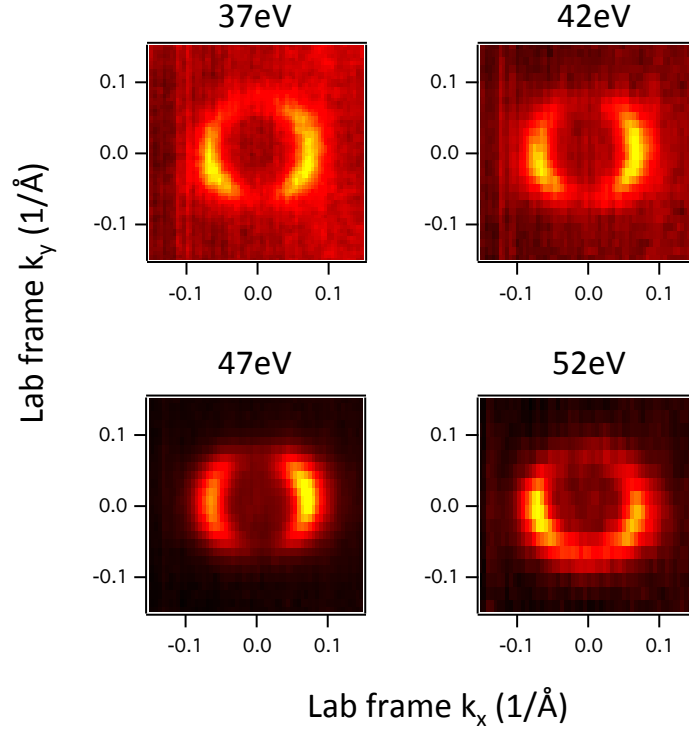
Figure 3.7: The constant energy surface intensity variation of the Dirac state as a function of photon energy. The plot shows the intensity 200 meV above the Dirac point of Bi_2Se_3. The observed intensity variation does not change with photon energy, indicating the final states in the matrix element are free electron states.

crystalline directions of the sample, as is seen from the data of 3.6 **b**. A summary of the symmetry analysis is listed in Table 3.1.

We could deduce from Figure 3.6 **c** the in-plane p orbitals $|\psi_i\rangle$ that are consistent with the symmetry constraints discussed above, that is, odd with respect to the orange and green mirror planes above the DP and even with respect to these planes below the DP. These orbital wavefunctions are tangential to the constant energy surface above the DP and then switch to being radial to the constant energy surface below the DP. This is shown more clearly in Figure 3.3 as the orange orbitals, while showing the out-of-plane p_z components of the wavefunction in green. It is quite evident from symmetry analysis that linear polarization cleanly disentangles ARPES intensity contributions from different p orbitals, while the circular polarization used in previous experiments [55, 29, 59, 60] focused on the spin chirality or the "handedness" of the wavefunctions.

The measured orbital texture is captured in our first-principles calculations based on the local density approximation. The calculated Dirac surface bands, the bulk conduction band, and the bulk valence band nearest to the DP of Bi_2Se_3 and Bi_2Te_3 are drawn in Figure 3.8 **a** and **d**. The orbital character of electronic states is obtained by projecting the calculated plane-wave based wavefunctions $|\psi_{nk}\rangle$ (n being the band index and k being the crystal momentum) onto spherical harmonics $|J_l^{R_i}Y_{lm}^{R_i}\rangle$ including p-orbitals ($l = 1$) centered at the position of the ions R_i.

$$|\psi_{nk}\rangle = \sum_{i}^{N_{at}} \sum_{lm} \alpha_{m,nk}^{R_i} |J_l^{R_i}Y_{lm}^{R_i}\rangle \tag{3.4}$$

where N_{at} is the total number of atoms. Also we choose an s-like ($l = 0$) final state to represent the electron state photon-excited to vacuum, so that it is always even with respect to the proposed mirror planes. The projection strategy is so chosen to bring about the symmetry information in the atomic orbitals, without contributions from any special mirror plane. We find that the Dirac cone states especially those away from the DP are a hybridization of topological surface states and bulk states as evidenced by their wavefunction distribution. This feature of the topological states was found in 2D HgTe/CdTe topological insulator [61]. In order to distinguish the pure topological surface states from bulk band states, we projected the states layer-by-layer and summed up the
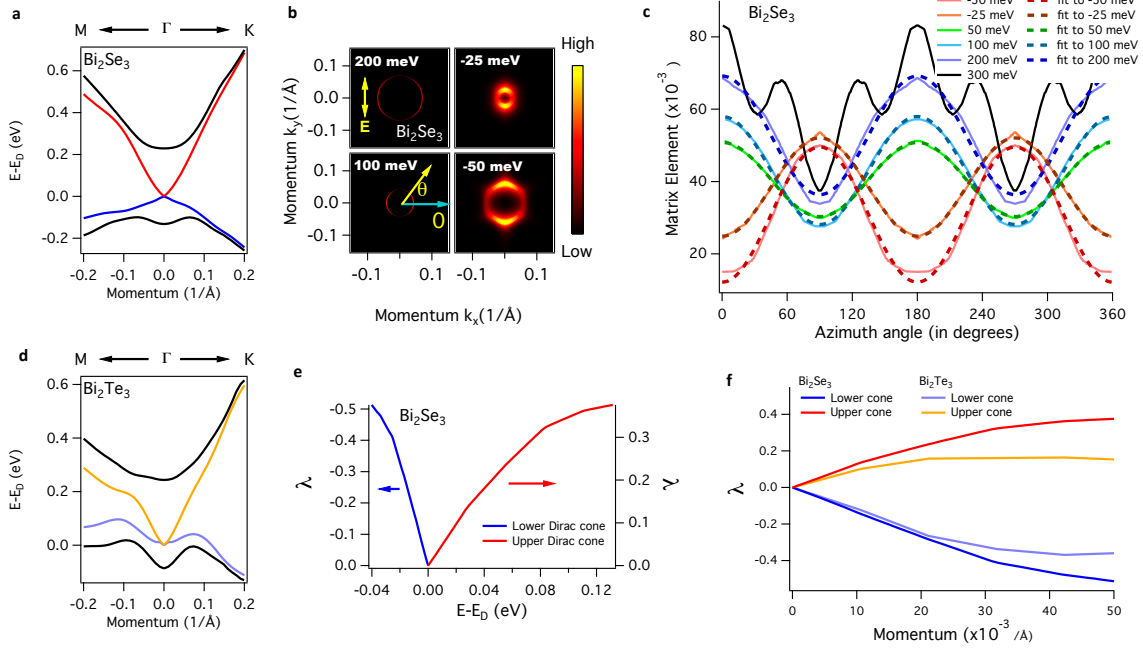
Figure 3.8: Orbital Polarization Ratio λ switches sign at the DP. **a**. and **d**. First-principles calculation of Bi_2Se_3 and Bi_2Te_3, only showing the Dirac bands and the bulk bands closest to the DP. **b**. Calculated p_y orbital intensity at different energies relative to the DP of Bi_2Se_3, each summed over a window of 20 meV relative to the central energy shown on the plot. **c**. For each energy relative to the DP of Bi_2Se_3, the calculated projected p_y orbital intensity as a function of the sample in-plane azimuth angle (for the definition of the azimuth angle, see panel **b**, with 0° as marked). The dashed lines are the selected $\cos 2\theta / \sin 2\theta$ fits to the calculated p_y intensities shown in solid lines. **e**. Calculated orbital polarization ratio λ of Bi_2Se_3 as a function of the energy relative to the DP. **f**. Calculated λ of Bi_2Se_3 and Bi_2Te_3 as a function of momentum k. Note λ switches sign exactly at the DP.
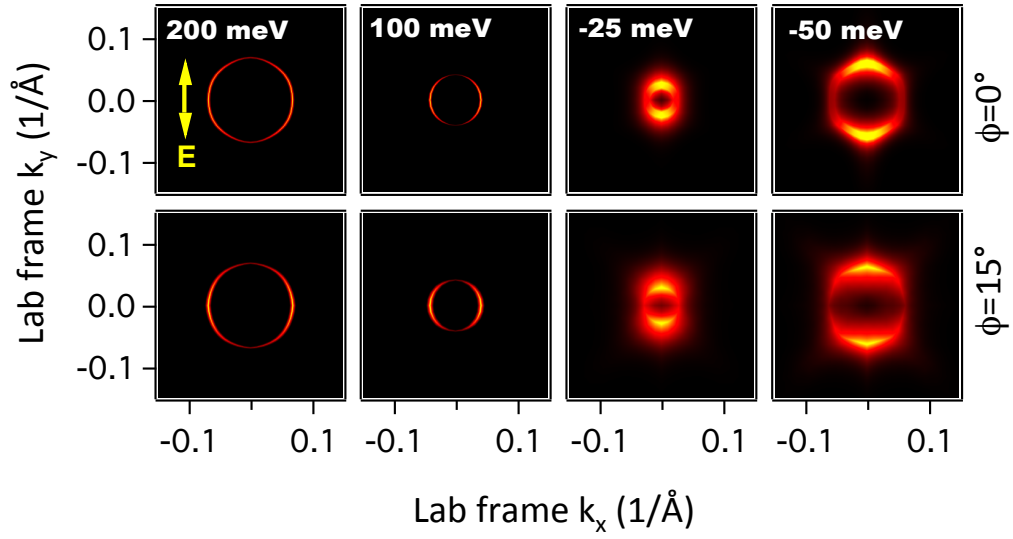
Figure 3.9: Calculated p_y orbital intensity at a variety of energies for two different sample orientations of Bi$_2$Se$_3$. Top panels show original sample orientation with ΓK along k_x, and bottom panels have a sample rotation of 15° rotated counterclockwise from the top panels, while leaving the photon polarization fixed to the lab frame. The lack of any change with rotation is consistent with the experimental observations of Figure 3.6 **b**.

contribution of each atomic orbital with an exponential weighting away from the surface, and we confirmed the choice of decay distance does not affect the calculation qualitatively. The results presented here have a decay distance of 0.5nm, which approximates the ARPES probe depth.

The experimental ARPES configuration performed with s polarized incident photons is replicated in the calculations by projecting the intensity of the p_y orbital. In Figure 3.8 **b** we show the calculated p_y orbital intensity of the Dirac state for Bi_2Se_3 on constant energy surfaces above and below the DP, each summing over a 20 meV energy window. The calculation well reproduces the experimental measurement of the orbital texture of the Dirac state. For example, above the DP, the calculated p_y component maximizes along the lab axis k_x and minimizes along k_y (where the p_x orbital dominates the in-plane states). Similar to the experiment, we also found that rotating the sample azimuth angle relative to the lab frame by angle φ has minimal effect on the calculated p_y intensity distribution, especially near the DP. In Figure 3.9, Bi_2Se_3 is rotated by 15° and the intensity distribution remains unchanged.

To further trace the origin of the orbital texture switch of the Dirac state, we would like to zoom in close to the Dirac point as this is the region where the Dirac physics is unaffected by lattice effects or hybridization to the bulk bands. Due to the limit of experimental resolution we explore this near-DP region using the initial-state p orbital densities from *ab initio* calculations. The calculated p_y orbital intensity for each constant energy surface is displayed as a function of sample azimuth angle (as defined in Figure 3.8 **b**) in 3.8 **c**. Most notable is the switch of the intensity distribution above and below the DP, which is a signature of the orbital texture switch. Also as the energy gets closer to the DP, the intensity variation fits better to a $\cos2\theta$ or $\sin2\theta$ distribution. At 300 meV above the DP, the intensity curve shows a six-fold modulation on top of the $\cos2\theta$ function. This additional modulation might come from the hybridization to the bulk bands, or from the non-isotropic term of spin-orbit coupling [53]. To identify whether the switch is sudden or gradual, we define the Orbital Polarization Ratio (OPR) λ as a function of either energy

(ω) or momentum (k=$|\vec{k}|$) relative to the DP

$$\lambda(\omega) = \frac{I_0(\omega) - I_{90}(\omega)}{I_0(\omega) + I_{90}(\omega)} \tag{3.5}$$

or

$$\lambda(k) = \frac{I_0(k) - I_{90}(k)}{I_0(k) + I_{90}(k)} \tag{3.6}$$

where I_θ is the calculated p_y orbital intensity around the CES, with the $0°$ angle in θ defined in Figure 3.8 **b** (note that this angle is relative to the lab frame, while the angle φ is between the sample and lab frame – see Figures 3.5 and 3.6). $\lambda > (<)0$ indicates there is a larger proportion of the tangential (radial) in-plane orbital. Figure 3.8 **e** and **f** show that this switch occurs exactly at the DP for both Bi_2Se_3 and Bi_2Te_3.

Analysis of the λ-dependence on electron momentum and energy yields the wavefunction of the topological state in the vicinity of the DP

$$|\psi(\vec{k},0)\rangle_+ = \sqrt{1-\alpha}|p_z\rangle \otimes |LHS\rangle + \sqrt{\frac{\alpha}{2}}\left[(1+\beta k)|p_t\rangle \otimes |s_t\rangle + (1-\beta k)|p_r\rangle \otimes |s_r\rangle\right] \tag{3.7}$$

and

$$|\psi(\vec{k},0)\rangle_- = \sqrt{1-\alpha}|p_z\rangle \otimes |RHS\rangle + \sqrt{\frac{\alpha}{2}}\left[(1-\beta k)|p_t\rangle \otimes |s_t\rangle + (1+\beta k)|p_r\rangle \otimes |s_r\rangle\right] \tag{3.8}$$

where $\pm$ denotes the wavefunction above / below the DP, α and β are (complex) coefficients and $|p_{z,t,r}\rangle$ stands for the p_z, tangential and radial in-plane p orbitals, respectively. $|LHS/RHS\rangle$ are left-handed and right-handed spin textures consistent with all previous spin resolved measurements and calculations (see e.g. [62, 44]) and $\otimes$ is the cross product between the orbital and spin degrees of freedom. There may still be additional phases among the $|p_{z,t,r}\rangle$ terms and we absorb these phases into the definition of $|p_{z,t,r}\rangle$ for the moment. The proposed wavefunction has the following characteristics:

First, the coefficient $\alpha \sim 1/2$ is the fraction of the p-orbitals with in-plane character, as determined from first-principles calculation. Both experiments and calculation show the in-plane orbital components account for a significant part of the Dirac wavefunction.

Second, the terms with βk reflect how fast the in-plane orbitals become predominantly tangential $|p_t\rangle$ or radial $|p_r\rangle$ away from the DP. At the DP ($k = 0$) the terms with βk disappear and the Dirac wavefunction has an equal proportion of radial and tangential in-plane orbitals. These statements come from the fact that λ linearly approaches zero as the energy (Figure 3.8 **e**) or momentum (Figure 3.8 **f**) approaches the DP, and to within the statistical error, changes sign exactly at the DP.

Third, the orbital content of the wavefunction can be determined by using only two parameters α and β. While we might have expected different β coefficients above and below the DP, the fact that the slopes of λ vs. k appear equal above and below the DP ($\sim$13Å for Bi_2Se_3 and 11Å for Bi_2Te_3, deduced from the slope of the curves in Figure 3.8 **f**) suggests that we need only a single β coefficient.

Our observation that the orbital texture switches exactly at the DP in two topological insulators with quite distinct electronic structures provides strong evidence that the orbital polarization switch is an intrinsic feature of the Dirac surface state. The DP of Bi_2Te_3 is much closer ($<$20meV) to the bulk valence band than Bi_2Se_3, and the surface state dispersion bends upward below the DP, in stark contrast to Bi_2Se_3 that has the more "ideal" Dirac-like linear dispersion. Despite the significant differences in the surface state dispersion, the two compounds show an almost identical behavior of the OPR λ, which changes sign exactly at the DP in both cases. This new behavior indicates the unexpected richness of the surface states of topological insulators. While the underlying symmetries that are responsible for this generic switching behavior have not yet been unearthed, complete effective models of the topological state should apparently include these features.

At this point, we have two possible forms of wavefunctions: If all the orbital components above (below) the DP couple to the same LHS/RHS spin texture, the complete Dirac wavefunction merely has a previously unnoticed spatial wavefunction, but is fundamentally the same otherwise. The other possibility is each of the orbital component couples to a different non-colinear spin orientation at the same momentum. We name the wavefunction from this possibility a "spin-orbital texture" as the Dirac wavefunction could no longer be decomposed as the product of the spin and orbital

sectors. This possibility is of course far more interesting and is chosen by Mother Nature, as we will show in Section 3.4.

3.4   Determining the Spin-Orbital Coupling

In this section, we show the Dirac wavefunction has a "spin-orbital texture", as opposed to the "spin texture" commonly used in previous literatures where only one orbital (p_z) was assumed to appear. Specifically, the in-plane p orbital tangential to the constant energy surfaces above the DP couples to a "backwards" right-handed spin (RHS) texture, while the p_z orbital has the standard left-handed spin (LHS) texture.

This is accomplished using spin-polarized electron detection, with the orbital selective p and s polarization of the incident photons. We would like to name this experimental strategy the orbital-selective spin-resolved ARPES (OS-SARPES). OS-SARPES is not a new experimental technique. Rather, it is a set of deliberately designed experiments aiming at disentangling the spin and orbital degrees of freedom. In these experiments, we carefully choose the relative geometry between the photon and the sample so that only *one* orbital in the initial wavefunction is excited with selected photon polarization. The measured photoelectron spin is thus the spin coupled to the excited orbital component.

The experiments were performed on single crystals of Bi_2Se_3 cleaved and measured *in situ* at T=21K with a photon energy of 47 eV at the COPHEE endstation at the Swiss Light Source [63]. The COPHEE endstation utilizes a helical undulator, allowing us to change the incident photon polarization from linear s to linear p without altering any other parameters of the experiment, and the multi-axis spin detector at this facility allows for a deconvolution of the various spin degrees of freedom, as described in Ref. [64].

The experimental geometry for the designed OS-SARPES measurements is shown in Figure 3.10 **a**. The photons come in at 45° relative to the sample normal and can be tuned to have either s or p polarization. The p polarization has the photon E-field parallel to the scattering plane, and lying tilted 45° out of the sample surface plane. When taking the spin resolved measurements,
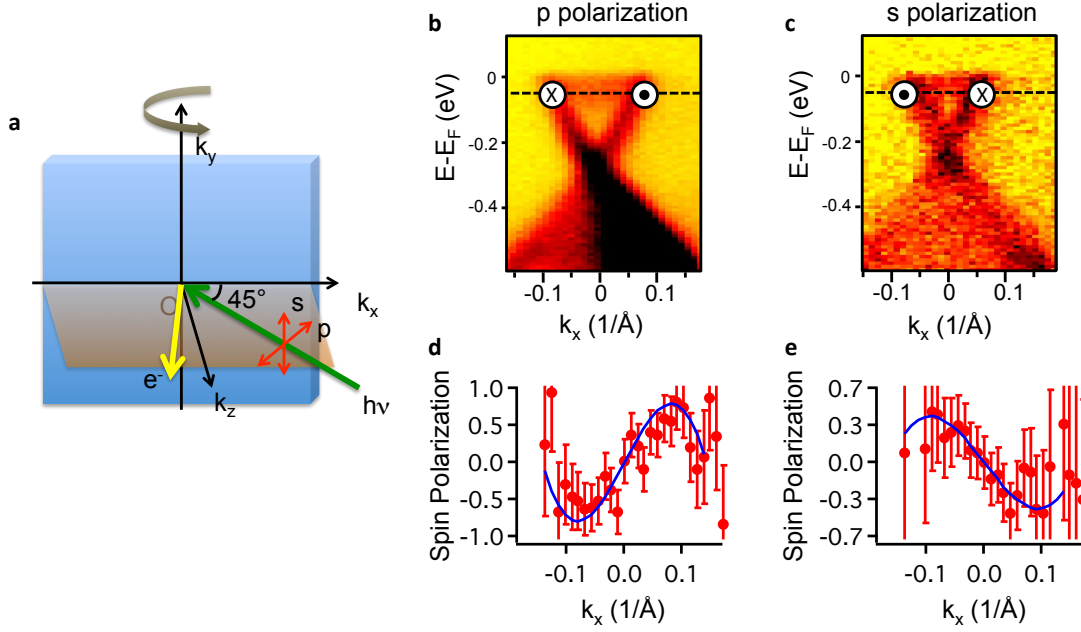
Figure 3.10: Determining the Spin-Orbital Coupling in Bi$_2$Se$_3$. **a**. Cartoon drawing of the experimental geometry. The green and yellow arrows indicate the incoming photon and outgoing photoelectron, which conserves in-plane momentum. The beam comes in at 45° relative to the sample surface. Each spin resolved momentum distribution curve (MDC) as shown in panels **d** and **e** is taken by rotating the sample relative to the k$_y$ axis. **b** and **c** are the energy-momentum intensity plots along the Γ-K orientation of Bi$_2$Se$_3$, with the measured spin texture drawn in for the corresponding photon polarization. The spin asymmetry curves are shown in panels (d) and (e).

we rotate the sample about the k_y axis in the sample plane and normal to the photon incidence plane. Thus in principle, for each data point in the spin asymmetry curve, the photon comes in at a different angle and the ratio between the matrix elements from the $|p_t\rangle$ and $|p_z\rangle$ changes. Note the s polarized photon is sensitive to only the in-plane orbital states while the component of the p polarization normal to the sample is strongly dominated by the out-of-plane p_z states.

Fortunately, the photon energy is held at 47eV and comes in at $45°$ (instead of glancing incidence) and we can cover the Dirac cone by rotating the sample within $\sim2°$. As a first order approximation, we could assume this ratio between the matrix elements of different orbitals to be a constant. However, for a 6eV photon with glancing incidence, we need to take the above mentioned effect into account.

Panels 3.10 **b** and **c** show spin-integrated measurements taken with p and s polarization respectively along the k_x axis (along the Γ-K cut through the Brillouin zone) by rotating the sample about the k_y axis (see Figure 3.10 **a**). Aside from the reduction in experimental statistics for the s-polarized data, these panels show an identical E vs. k_x dispersion for both polarizations, We took the spin-resolved data in the exact same geometry, at a fixed binding energy of 50 meV in the upper Dirac cone, which is ~300 meV above the DP. For this energy range, the $|p_r\rangle$ has negligible contribution to the complete Dirac wavefunction. The spin-resolved data are shown in Figures 3.10 **d** and **e**, taken along the black dashed lines of Figure 3.10 **b** and **c**. The measured spin polarizations are opposite for the two panels —they show a left-handed spin helicity for the p polarization data and a right-handed spin helicity for the s polarization data.

The spin polarization data taken using s polarization has photons polarized along the k_y axis and is associated with the in-plane $|p_t\rangle$ orbital. The p polarized photons could be decomposed as a $1/\sqrt{2}$ component along the sample normal and a $1/\sqrt{2}$ component along the k_x axis. Note that the $|p_t\rangle$ orbital is associated with the in-plane component of the p polarization and has vanishing spectral weight along k_x. This could be understood by referring to the intensity distribution on the constant energy surface using s polarization (see Figure 3.6 **a**), where the intensity along the electric field comes only from the radial p orbital and is very small >200meV above the DP. Note

for the p polarization in the spin-resolved experiment here, the in-plane electric field component is $90°$ rotated compared to the electric field using s polarization in Figure 3.6 **a**. Thus we expect the intensity distribution associated with this in-plane component of the p polarization is also rotated by $90°$ from that of s polarization, giving very small intensity from the $|p_t\rangle$ orbital. Therefore the spin polarization data taken using p polarization is strongly dominated by the $|p_z\rangle$ orbital.

Now we conclude the $|p_z\rangle$ orbital couples to the usual LHS [47, 62, 65, 45], and the in-plane $|p_t\rangle$ orbital couples unexpectedly to the RHS texture. We illustrate this result in Figure 3.3. Figure 3.3 **c** shows the dominant tangential orbital states $|p_t\rangle$ above the DP and the dominant radial orbital states $|p_r\rangle$ below the DP, along with the predicted (see discussion below) spin helicity for each of these states.

The magnitude of the spin polarization detected in the present experiment is between 50% and 100% for both polarizations. When deconvolving with the resolution and background we get a $\sim 100\%$ polarization for each of the measurements. This is one of the clearest evidence of the spin-orbital texture. When only one type of orbital is excited, as we are able to do here by selecting the appropriate photon polarization, all the electrons that come out have the "same" spin. In other words, the photoemission process preselects the wave function and the spin expectation value is thus the same for all photoexcited electrons. The measurements here turn out to be the crucial test for the general principle above.

The spin measurements are fully consistent with the early predictions in [66]. While the "coupled spin-orbital texture" results from the spin orbit interaction, how the spin textures couple to the orbital components is a direct manifestation of the conserved out-of-plane total angular momentum j_z. Specifically, as the surface is well described by its two dimensional surface momentum, its spin, and a p-like orbital degree of freedom, the total angular momentum is well defined *only* normal to the surface, and can be taken[3] to be $j_z = -i\partial_{\phi_k} + s_z + l_z$ in units of $\hbar$, where ϕ_k is the azimuthal angle of the momentum, s_z has eigenvalues $\pm 1/2$, and l_z has eigenvalues $0, \pm 1$. It is straightforward to verify that the wave functions $|p_z\rangle \otimes |LHS\rangle$ and $|p_t\rangle \otimes |RHS\rangle$ both have

---

[3] The definition we use here is different from [66].

$j = 1/2$. In other words, angular momentum is a good quantum number of the measured wave function, indicating that it is conserved by the effective Hamiltonian governing the surface states.

The spin orientations between $(\pm k_x, 0)$ using s and p polarizations are reversed above the DP. This result is not related to the time-reversal symmetry. The photoemission process by itself breaks the time reversal symmetry, and the spin-flip between $(\pm k_x, 0)$ points is a reflection of the spin-flip in the initial state wavefunction, not a reflection of the time reversal symmetry of the final photoelectron state. In principle, the spin orientation between a pair of inverted points in k space does not need to flip, as shown in Ref. [67, 68].

Now we write the approximate wavefunction $\sim$300meV above the Dirac point, where the spin polarized measurements in this paper were made. In particular, as seen from experiment the in-plane radial component $|p_r\rangle$ has negligible weight at this energy and we are reduced to two principle orbitals in the Dirac state wavefunction

$$|\psi(\vec{k},0)\rangle_+ = \sqrt{1-\alpha}|p_z\rangle \otimes |LHS\rangle + e^{i\chi}\sqrt{\alpha}|p_t\rangle \otimes |RHS\rangle \qquad \text{(well above Dirac point)} \qquad (3.9)$$

where $|LHS\rangle$ and $|RHS\rangle$ are the left-handed spin and right-handed spin along k_y direction. The $+/-$ subscripts denote the wavefunction above / below the Dirac point and $\otimes$ is the product between the orbital and spin degrees of freedom. There could be an extra phase of χ between the two orbitals.

Combined with our previous observations of the orbital texture [57] (also see Section 3.3), similarly we have the wavefunction for the Dirac surface state in the vicinity of the Dirac point

$$
\begin{aligned}
|\psi(\vec{k},0)\rangle_+ &= \sqrt{1-\alpha}|p_z\rangle \otimes |LHS\rangle \\
&\quad + e^{i\chi}\sqrt{\frac{\alpha}{2}}\big[(1+\beta k)|p_t\rangle \otimes |RHS\rangle - i(1-\beta k)|p_r\rangle \otimes |LHS\rangle\big]
\end{aligned}
\qquad (3.10)
$$

and

$$
\begin{aligned}
|\psi(\vec{k},0)\rangle_- &= \sqrt{1-\alpha}|p_z\rangle \otimes |RHS\rangle \\
&\quad - e^{i\chi}\sqrt{\frac{\alpha}{2}}\big[(1-\beta k)|p_t\rangle \otimes |LHS\rangle - i(1+\beta k)|p_r\rangle \otimes |RHS\rangle\big]
\end{aligned}
\qquad (3.11)
$$

where α, β and χ are coefficients. These wavefunctions are similar to those written down by Zhang *et al.* in Ref.[66] but are more constrained by experimental data, with far fewer (only α, β and χ) undetermined parameters. The phase i between the various in-plane orbitals is chosen to be consistent with Ref. [66].

Recently, Zhu et al. [27] showed the dominant in-plane p orbital component varies for each atomic layer in the quintuple layer counting from the interface, as shown in Figure 3.11. However, regardless of the atomic layer, whenever the $|p_t\rangle$ is the dominant p orbital in plane, the spin chirality is right-handed. The spin-orbital coupling is exactly as shown in Eqn. (3.10). These results further confirm the spin-orbital texture is a direct demonstration of a conserved j_z.

It is to be noted the spin-orbital texture also appears in other solids [69, 70]. Our work of disentangling the spin-orbital coupling may inspire future work into these new material families.

3.5   Controlling the Spin of the Photoelectrons

Achieving high spin polarization is desired for realistic spintronics applications [71, 72] and is also one of the main goals in the search for new topological insulators [73]. The helical spin texture was almost universally believed to be left-handed above the DP and right handed below. However, previous spin-resolved experiments [47, 62, 74] with varying geometries and photon polarizations and first-principles calculations [65, 45] have produced controversial results concerning the fraction of spin-polarized electrons, ranging from $\sim$20% [47] to $\sim$75% [62]. Recently, Jozwiak *et al.* [68] reported that the spin polarization of the photoelectrons can be manipulated through selection of the light polarization, and be very different from the left-handed (right-handed) spin texture above (below) the DP.

These works have exclusively focused on the following two questions: (a) what the spin polarization axis is, and (b) what percentage of electrons is spin-polarized. The underlying assumption, usually not explicitly stated, is that the Dirac wavefunction has a simple structure – only one orbital wavefunction p_z exists, coupled with the spin orientation well defined on a Bloch sphere. It follows naturally that Jozwiak and Park *et al.* [68, 67] interpreted the observed photoelectron spin
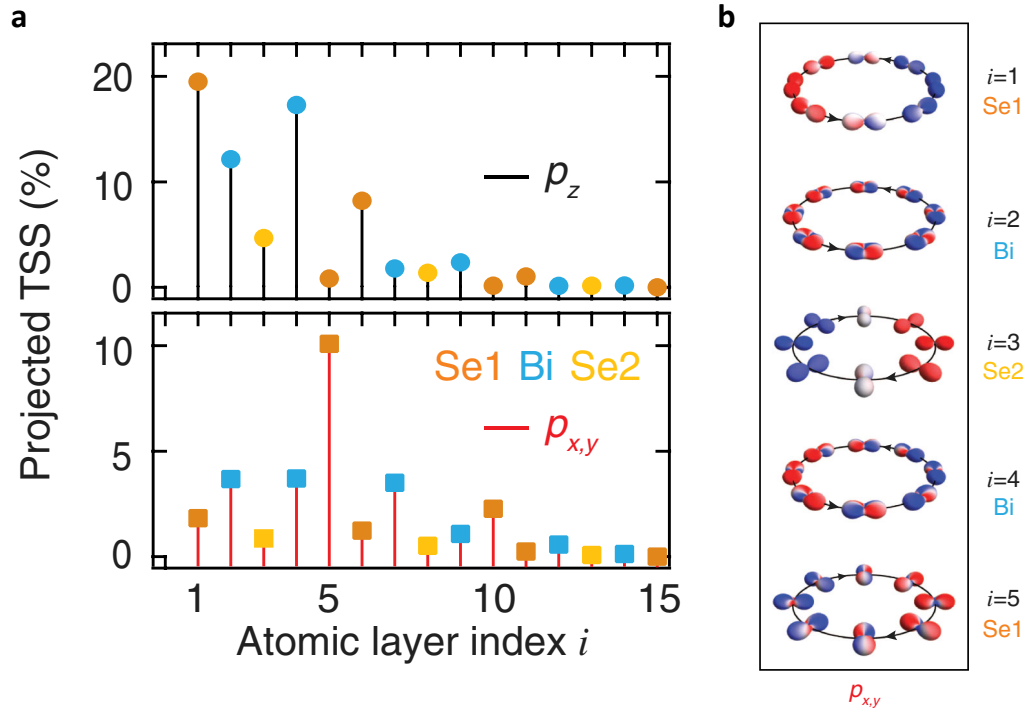
Figure 3.11: The atomic layer dependence of the spin-orbital texture. After [27]. **a**. The percentage of p_z and in-plane p orbitals in the Dirac surface state at 150meV above the DP, for the top 15 atomic layers. **b**. Layer-projected in-plane p orbital density and spin texture at 150meV above the DP.

rotation as "due to the spin-dependent interaction of the helical surface electrons with light, which originates from strong spin-orbit coupling".

The discovery of the spin-orbital texture offers an inspiring breakaway from previous assumptions. Clearly spin is not defined on a Bloch sphere for the complete spin-orbital coupled wavefunction, and is only defined for each individual orbitals. Indeed, the possibility of a spin-orbital coupled wavefunction would profoundly reshape the design and interpretation of spin-resolved measurements. Instead of asking "along which axis does the spin polarize" or "what percentage of spin is polarized", now we need to take into account the orbital wavefunction and explore how spin couples to each of the orbital components.

The spin-orbital texture provides a route to reconciling previous measurements. Roughly speaking, in the presence of multiple orbitals, each carrying their corresponding spin orientation, the total spin of the measured photoelectron exhibits interference from each spin component and depends crucially on the experimental geometry and photon polarization. To put our argument on a firm footing, we would like to revisit the matrix element in the presence of strong spin-orbit coupling. Specifically we focus on whether spin-orbit coupling induces "spin-dependent interaction of electrons with light" [68, 67].

The complete interaction between electrons in a solid and the external electromagnetic field has the general form [67]

$$\mathcal{H}^{int} \propto \vec{A} \cdot \vec{v} = \vec{A} \cdot \left[\frac{\vec{p}}{m_e} + \frac{\hbar}{4m_e^2 c^2} \left(\vec{s} \times \nabla V \right) \right] \tag{3.12}$$

where $\vec{A}$ is the electromagnetic gauge, $\vec{p}$ is the momentum of the electron and V is the ionic potential the electron experiences. This comes from the invariance of the electromagnetic gauge [67]. For spin degenerate systems, the spin orbit coupling (which still exists) is believed to have a very minor effect on the spin of the photoelectron and the spin-flipping term in Eqn. (3.12) is often ignored. This then gives the matrix element $|\langle \psi_f | \vec{A} \cdot \vec{p} | \psi_i \rangle|^2$ for the photoemission process, as commonly used in the ARPES experiments [8] as well as direct DFT simulations of the matrix elements [28].

It would be interesting to see if the spin-flipping term would have a finite effect on the spin

of the photoelectron (the final state) for spin polarized systems. To compare the contribution of the two terms in Eqn. (3.12), we rewrite the interaction Hamiltonian as

$$\mathcal{H}^{int} \propto \vec{A} \cdot \vec{v} = \frac{\hbar}{m_e}\vec{A} \cdot \left[\vec{k} + \frac{1}{4m_ec^2}\left(\vec{s} \times \nabla V\right)\right] \tag{3.13}$$

The second term $\sim 5 \times 10^{-7}\left(\vec{s} \times \nabla V\right)\text{eV}^{-1}$ and the typical k value for actual experimental measurement (so that peaks from different k points or energy points are well separated) is $0.05\text{Å}^{-1} \sim 0.1\text{Å}^{-1}$. For the two terms to be comparable, we need $\partial V/\partial r \sim 4 \times 10^5 \text{eV/Å}$. Assuming the p electron (5p electron for Bi and 3p electron for Se) could get close to the nucleus where the spin orbit coupling is strongest and the Coulomb repulsion is unscreened, the potential gradient could be approximated by

$$\frac{\partial V}{\partial r} \sim \frac{1}{4\pi\epsilon_0}\frac{Ze^2}{r^2} \tag{3.14}$$

which would put the p electron at a distance of $\sim 6\sqrt{Z} \times 10^{-3}\text{Å}$ (0.055Åfor the Bi atom and 0.035Åfor the Se atom) to the nucleus. The covalent radius is $\sim$1.5Åfor Bi and $\sim$1.2Å for Se. Thus electrons have a negligible probablity to stay near the atomic core and flip the spin.

This indicates the photoelectron is mostly determined by the matrix element $|\langle\psi_f|\vec{A} \cdot \vec{p}|\psi_i\rangle|^2$ and the spin is conserved between the electron in the solid and the excited photoelectron. Thus the OS-SARPES experiments in Section 3.4 faithfully reflects the spin texture of the selected orbitals in the initial state Dirac wavefunction.

The wavefunction of the photoelectron (the "final state") is given by [67]

$$|\psi_f\rangle = \sum_\sigma |PW,\sigma\rangle\langle PW,\sigma|\vec{A} \cdot \vec{p}|\psi_i\rangle \tag{3.15}$$

where $|PW,\sigma\rangle$ is the plane wave with spin up/down and has an energy of $E_f = E_i + h\nu$. The wavefunction of the photoelectron does not have any orbital character and is a direct superposition of the spin from each component of the initial state wavefunction. We visualize the relation between the initial and final state wavefunctions in Figure 3.12 **a**. The initial state is a two-component spin-orbital wavefunction. The spin orientations coupled to the solid pink and green orbitals are not colinear. We assume the p (with E_x and E_z in phase and colored in red) polarized photons have

non-vanishing matrix element *only* with the pink orbital. Similarly, the s polarization (with E_y colored in dark green) only interacts with the green orbital wavefunction. The final state is a plane wave, with the two spin components (inherited from the initial state) interfering with each other. There is a relative phase φ_{sp} between the s and p components of the electric field and will be carried into the final state. The prefactor A is the ratio between the non-zero transition probabilities $\langle \psi_f | \vec{A} \cdot \vec{p} | \psi_i \rangle$ from the s and the p polarization. Since the spin-orbital wavefunction of the Dirac surface state exhibits a linear combination of both spin chiralities at the same energy, it is possible to engineer the spin polarization of the photoelectron by "tuning" the relative phase between the electric field components (and thus the photon polarization).

Now we study the photoelectron spin polarization $\geq 200\text{meV}$ above the DP and along the postive k_x axis. Experimentally, the $|p_r\rangle$ orbital is found to be negligible in the complete Dirac wavefunction at this energy range. The initial state and final state could be written as

$$|\psi_i(+\omega)\rangle_{(+k_x,0)} = \sqrt{1-\alpha}|p_z\rangle \otimes \begin{pmatrix} 1 \\ -i \end{pmatrix} + e^{i\chi}\sqrt{\alpha}|p_t\rangle \otimes \begin{pmatrix} 1 \\ i \end{pmatrix} \tag{3.16}$$

and

$$|\psi_f(+\omega)\rangle_{(+k_x,0)} = |PW\rangle \otimes \left[\begin{pmatrix} 1 \\ -i \end{pmatrix} + e^{i(\chi+\varphi_{sp})}A \begin{pmatrix} 1 \\ i \end{pmatrix} \right] \tag{3.17}$$

where the LHS/RHS along k_x are

$$|LHS\rangle_{(+k_x,0)} = s_{y-} = \begin{pmatrix} 1 \\ -i \end{pmatrix} \qquad |RHS\rangle_{(+k_x,0)} = s_{y+} = \begin{pmatrix} 1 \\ i \end{pmatrix} \tag{3.18}$$

In Figure 3.12 **b** the photon polarization are defined as in [68, 67]. Note only the E_z component of the p polarization will couple to $|p_z\rangle$, so the photon could not come in normal to the sample. For $\chi = -\pi/2$ and $A = 1$. For +sp photon polarization, $\varphi_{sp} = 0$ and

$$|\psi_f(+\omega)\rangle_{(+k_x,0),+sp} = (1-i)|PW\rangle \otimes \begin{pmatrix} 1 \\ 1 \end{pmatrix} \tag{3.19}$$
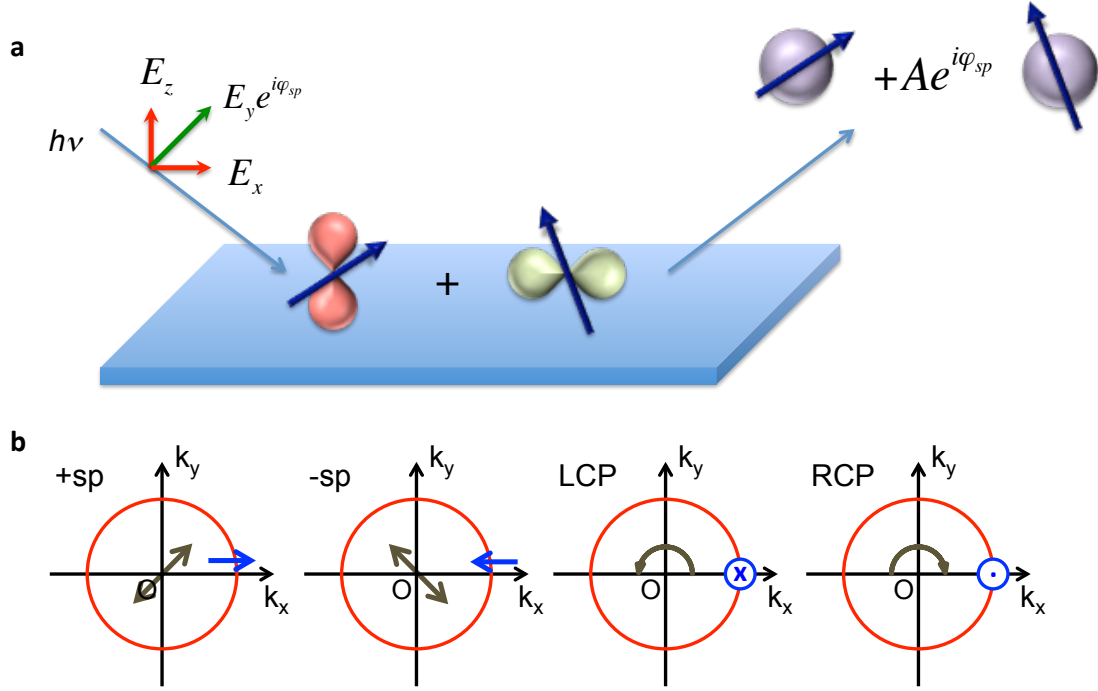
Figure 3.12: The mapping relation between the initial and final state wavefunctions and the manipulation of photoelectron spin with polarized photons. **a**. The spins coupled to the solid pink and green orbitals in the initial state are not parallel. The p (drawn in red) and s (drawn in dark green) polarized photons have non-vanishing matrix element with the pink and green orbitals respectively. The s polarization E_y has a phase φ_{sp} relative to the p polarization, which could be decomposed into E_x and E_z. The prefactor A is the ratio between the two nonzero photo-transition probabilities. **b**. The spin of the photoelectron with $\vec{k}_{\parallel} = (+k_x, 0)$ could be tuned with different photon polarizations. The grey arrows denote the photon polarization and the photoelectron spin orientations are marked in blue.

Similarly for -sp photon polarization, $\varphi_{sp} = \pi$ and

$$|\psi_f(+\omega)\rangle_{(+k_x,0),-sp} = (1+i)|PW\rangle \otimes \begin{pmatrix} 1 \\ -1 \end{pmatrix} \qquad (3.20)$$

We list the resulting photoelectron spin polarizations from different photon polarizations in Figure 3.12 **b**. These calculations match the predictions and measurements in [68, 67]. As we mentioned in Section 3.4, the dominant in-plane p orbital component changes with each atomic layer counting from the TI-vacuum interface. Zhu *et al.* [27, 75] have performed *ab initio* calculations and measurements of the photoelectron polarization, taking into the layer dependence. The guiding principle behind the seemingly complex calculation, is exactly what we have discussed in this section.

Chapter 4

The Physics of Doped Mott Insulators: Mostly Cuprates

Despite active research in the last three decades, mostly in the cuprate superconductors, the physics of doped Mott insulators and the Mott-metal crossover remain debated. Up to date, there is little consensus on many aspects of the Mott physics, from the global phase diagram, to the evolution of the band structure.

Our understanding of the Mott physics is largely hindered by the complex interplay among the spin, charge and lattice degrees of freedom, as well as a long list of emergent competing orders. It is almost impossible to give an unbiased, or complete account of the Mott physics. Thus I will instead focus on (1) the complexities of the Mott physics, and (2) the noteworthy features in ARPES measurements. I will introduce very briefly the temperature-doping phase diagram as investigated in experiments and theories. Detailed reviews are available in [76, 77, 8, 78, 79].

4.1   The Half Filled Mott Insulator

Mott designed his famous insulator [80] by tuning the lattice parameter of a half-filled metal to infinity. We visualize the formation of Mott insulators in Figure 4.1. For a periodic array of atoms close to one another (as in a typical metal) with one electron per atom, band theory dictates the band is half filled and the electrons migrate freely on the lattice (Figure 4.1 **a1**). Similar arguments could be made for an odd number of electrons per site, albeit with a slightly more complex band structure. As the inter-atomic spacing goes to infinity, the electrons are bound to their respective ion sites and form the Mott insulator (Figure 4.1 **b1**). In this process, the electron

hopping between nearest neighbor sites is suppressed with the increasing lattice constant.

We could also obtain a Mott insulator by increasing the Coulomb repulsion U for an atomic site with double electron occupancy. The natural ground state in the large U limit is to have one electron trapped to each ion (Figure 4.1 **b2**). Comparing these two formulations, the metal-Mott insulator transition is determined by the ratio of the onsite repulsion U and the electron hopping energy t.

The electron "dispersions" are distinct in the small/large U/t limit. For a negligible U/t in the metallic limit, the electrons fill the k states along the band dispersion up to the Fermi energy (Figure 4.1 **a2**). The system is expected to follow the Landau paradigm, with a relatively large quasiparticle lifetime, or a small MDC width in an ARPES measurement. For the "real" Mott limit where the electron hopping is completely suppressed, we could view each site as a stand-alone atom, with electrons occupying the same atomic level. Thus the electrons as a whole would have a narrow distribution in energy. On the other hand, every electron is localized to the atomic site. Due to the Heisenberg uncertainty principle, the electron momentum has a broad distribution. In other words, there is no defined band dispersion. In the ARPES spectrum, we then expect a "flat" spectral weight, corresponding to the state with one electron per site (Figure 4.1 **b3**). As there are a total of 2 electrons (with spin up and spin down) allowed per site, the occupied and empty states form the lower and upper Hubbard bands (LHB and UHB) respectively, separated by the energy scale of the Coulomb repulsion, or the Mott gap. Note the bandwidth (in energy) for both LHB and UHB is smaller than the Mott gap. For a sufficiently large U, the LHB could be pushed so deep below the Fermi energy that other states may now lie between the LHB and the E_F. These insulators are named "charge-transfer insulators" [76]. For example, in NiO and La_2CuO_4, the O 2p states are believed to have a higher energy than the transition metal 3d states [81, 82, 83]. For the majority of this chapter, however, we do not distinguish between Mott and charge transfer insulators.

Now we consider the phase transition as U/t goes from infinity (Mott insulator limit) to zero (Fermi metal limit) and come up with the following observations:
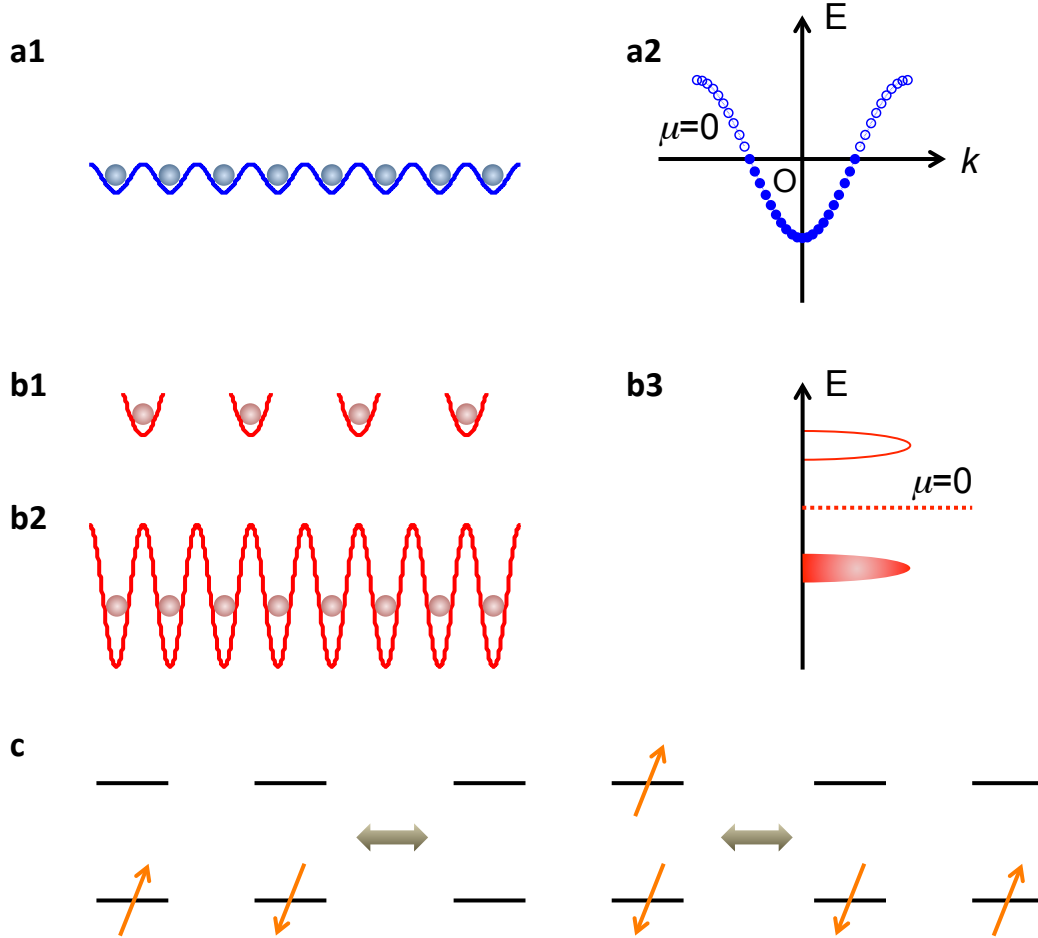
Figure 4.1: The transition between a Fermi metal and a Mott insulator. There is one electron (denoted by the solid dot) per atomic site (denoted by a potential well). The deeper potential well corresponds to the larger on-site Coulomb repulsion U. For a closely spaced atom array with a small U (panel **a1**), the electrons form a Fermi metal (panel **a2**), with the band dispersion half filled to the Fermi level. For atoms either far apart (panel **b1**) or with a large U compared to the electron hopping t (panel **b2**) a Mott insulator forms with the lower Hubbard band filled and the upper Hubbard band empty (panel **b3**). The Fermi level then lies between the upper and lower Hubbard bands. **c**. In a Mott insulator, anti-parallel spins on the nearest neighbor sites are allowed to exchange via a "virtual state" in which one site is doubly occupied.

- The bandwidth increases as $4t$, and possible band dispersion (as seen in ARPES, in contrast to the featureless atomic energy level) starts to form.

- The single-electron scattering lifetime (or the reciprocal of the MDC width observed in ARPES) increases, indicating the electrons are better described using band theory.

- The Mott gap eventually closes at a finite U/t.

Our analyses here (and throughout Chapter 4 and Chapter 5) focus on the dispersion and scattering rate, which could be directly observed in possible ARPES experiments.

With a finite t, the nearest neighbor hopping introduces an antiferromagnetic correlation. This could be understood by considering the processes shown in Figure 4.1 **c**. For the nearest neighbor sites, only anti-parallel spins are allowed to exchange, by creating an intermediate state with both electrons staying on one of the sites. Thus a local "spin singlet" on the nearest neighbor sites $\langle i, j \rangle$

$$|\psi\rangle_{\langle i,j\rangle} = \frac{1}{\sqrt{2}}(|\uparrow\rangle_i|\downarrow\rangle_j - |\downarrow\rangle_i|\uparrow\rangle_j) \tag{4.1}$$

is energetically favorable. This local antiferromagnetic correlation is intrinsic to the Mott insulator and is not equivalent to the formation of long-range antiferromagnetic order. A new energy scale $J \sim 4t^2/U$ could be introduced to characterize the local antiferromagnetic pairing. J is believed to be the leading energy scale that dominates the behavior of low energy electrons (as in the famous $t - J$ model) [78].

The long-range effect of this local antiferromagnetic correlation relies on the geometry of the lattice, as well as higher order interactions. For a frustrated lattice (e.g. triangular, Kagome) there are theoretical proposals [84, 85] and experimental evidences [86, 87] supporting a spin liquid phase (where no long-range spin order exists down to 0K). For the two-dimensional square lattice, experiments and numerical simulations [88, 89] suggest a stable long-range antiferromagnetic order. Meanwhile, there is no analytical solution of the ground state wavefunction. Possible candidates include, but are not limited to, antiferromagnetic dimers [90] and the "resonating-valence bond"

(RVB) state [91]. The stability of these proposed states depends on the details of the system, including the response of the lattice (as in the case of a dimer) and the next-nearest neighbor (and even longer-distance) spin interactions.

The long-range antiferromagnetic order on the square lattice (and other bipartite lattices) leads to a folded Brillouin zone with an even number of electrons. While less discussed, the formation of the antiferromagnetic Brillouin zone makes possible a description of the insulator using band theory. In the first-principles calculations, the antiferromagnetism is reinforced in addition to the "L(ocal) D(ensity) A(pproximation)+U" scheme to achieve a "band insulator"-like dispersion of the undoped Mott insulator. An example involves Sr_2IrO_4, which we will discuss in further detail in Chapter 5. We are not to interpret the "band insulator"-like dispersion as a signature of weak-correlation in the undoped Mott insulators. As discussed above, the strength of electron correlations is reflected both in the band dispersion and in the single-electron lifetime in an ARPES spectrum. Indeed the ARPES spectra of Sr_2IrO_4 [4] show a broad valence band, consistent with the strong correlations in the material. An interesting question is how the antiferromagnetic Brillouin zone evolves during the Mott-metal transition. While the antiferromagnetic Brillouin zone is expected to disappear or "unfold" in the good-metal limit, we do not understand the details of this process.

The Mott-metal phase transition is by definition a quantum phase transition, since we could tune U/t at 0K. The question at hand is whether a sharp boundary exists between the Mott and metal phases. Kohn suggested [92] this quantum transition actually consists of an infinite series of second-order transitions, or a "crossover". In a slightly different model where a Mott insulator is doped with charge carriers, Sachdev *et al.* [93] argued the Mott and metal phases are separated by a Quantum Critical Point. To date a definite answer to the nature of the Mott-metal transition is yet unavailable.

4.2 The Temperature-Doping Phase Diagram of Cuprates: An Experimental Review

The parent compounds of cuprate superconductors have been intensively studied in the last three decades. They are often modeled as a Mott insulator on the square lattice with one hole per site. A typical temperature-doping phase diagram of cuprates is shown in Figure 4.3. We compile this diagram following experimental evidences. We use shaded areas where a sharp boundary between different phases does not exist, or where the boundary is still controversial.

The two phases with well-defined phase boundaries are the antiferromagnetic phase (AF) and the superconducting phase (SC). These phases are distinguished from neighboring phases by bulk measurements. However, a comprehensive examination of experimental data reveals the nontrivial facets of both phases.

In the SC phase (or the superconducting dome named after its shape), the resistivity goes to zero, with the presence of the Meissener effect. The hole doping with the highest T_C is called the optimal doping (OP), and samples with hole dopings smaller / larger than the OP are said to be underdoped (UD) or overdoped (OD). The phase sensitve measurements [94], together with ARPES [95], revealed the superconducting gap $\Delta(\vec{k})$ has a d-wave paring symmetry, i.e. $\Delta(\vec{k}) \propto \cos k_x a - \cos k_y a$. An ideal d-wave gap vanishes at $k_x = \pm k_y$ (which we refer to as the nodal region) and maximizes near $k_x = 0$ or $k_y = 0$ (the anti-nodal region).

In ARPES measurements, for a large region from the lightly UD all the way to OD, and under the SC dome, the gap size follows the d-wave symmetry. Recent studies [96, 97] suggested for the ultra-underdoped sample there is a suppression of spectral weight at the nodal point. Thus the entire Fermi surface is gapped. There is no conclusion why a gap opens at the node, while Ref. [97] suggested some other pairing symmetries may be at work. There may exist profound changes under the SC dome, as suggested in Ref. [96].

The AF phase is defined by the magnetic response in bulk materials, and extends to a finite hole concentration $\sim 6\%$. The resistivity drops much faster than the long-range magnetic order.
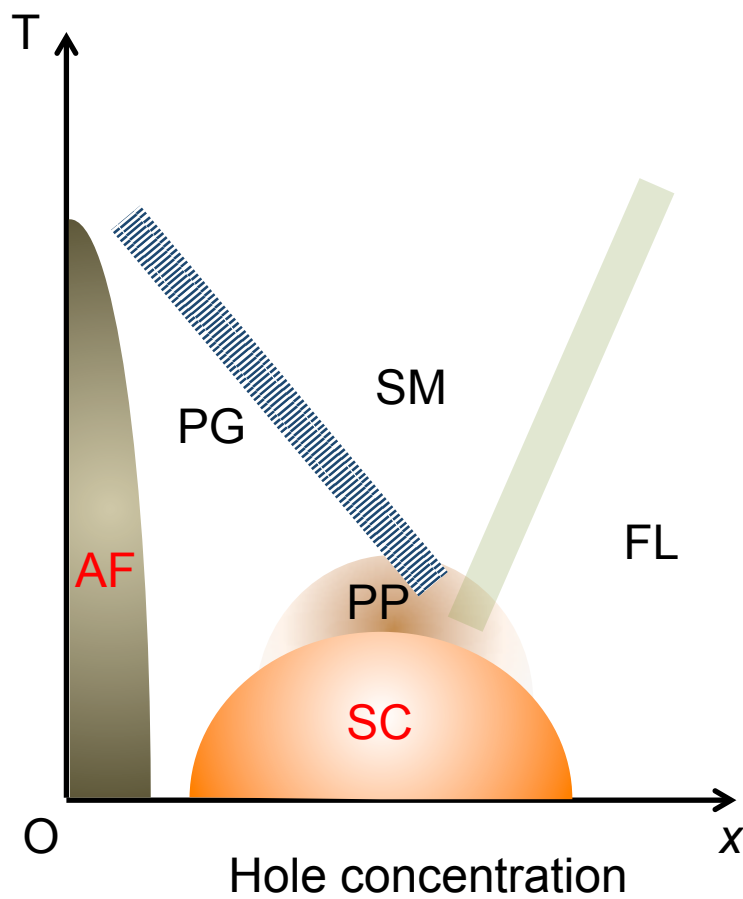
Figure 4.2: The experimental temperature-doping phase Diagram of Cuprates. The AF, PG, PP, SC, SM, FL stand for the antiferromagnetic phase, the pseudogap phase, the pre-pairing phase, the superconducting phase, the strange metal phase and the Fermi liquid phase respectively.

With as few as 1% doped holes [98], the in-plane resistivity shows a metallic behavior at moderate temperatures, with an upturn at lower temperatures. It appears there are already some "free" charge carriers even with a few doped holes. ARPES measurements in several systems [99, 100] observed band dispersion inside the Mott gap (defined by the parent compound) and close to the Fermi level. The quasiparticle spectral weight is vanishingly small at low hole concentrations and starts to grow with increased doping. Shen et $al.$ [100] ascribed these weak quasiparticles to certain polaron formation in the low doping limit, which is not widely agreed upon.

We refer to the region immediately above the SC dome as the pre-pairing (PP) phase [23], while the notion is not necessarily connected to the pre-pairing suggested by Anderson and others [91, 101, 102] which we will discuss in Section 4.3. In the PP phase, the once superconducting d-wave gap survives above T_C. As shown in [23], the ARPES spectral weight is transferred into the d-wave gap from below T_C all the way to T_{PP}, with the gap smoothly varying across T_C. It is interesting to see there is no sharp change in the ARPES features across T_C, despite drastic changes in the bulk properties. The PP phase does not show up in most bulk measurements, except in the Nernst signal [103]. Ref. [103] interpreted this region of the phase diagram as having spontaneous vortices. Whether the ARPES and Nernst experiments were observing the same physics is pending further investigation.

The region to the left and above the SC dome is the pseudogap (PG) phase. We draw the phase boundary roughly following compiled data in [79]. The pseudogap generally shows up as a suppression of spectral weight near E_F above T_C in a number of experiments, including ARPES, optical conductivity, inelastic neutron scattering, etc. [79, 77]. The spectroscopic features of a PG are in some sense similar to those of a band gap in classical semiconductors. We use the name pseudogap to distinguish them from the "hard" band gap. The origin of the PG is yet to be determined. Some reports suggest that the pseudogap may result from charge ordering [104].

The PP phase could be considered a part of the PG phase [105], and they share a common phase boundary in the near OP and OD region. As the hole doping is reduced from OP, the phase boundary of PG rises in temperature while that of PP curves down. The PP in this thesis follows

Ref. [23, 105], and the boundary of the PP phase is defined as the gap closing near the node. Some studies on the PG focused on the antinode [104], with a larger pseudogap size and higher gap closing temperatures.

4.3 Theoretical Investigations of the Doped Mott Insulator

The Mott insulator could be driven into metallicity by introducing extra charge carriers. For the convenience of discussion, we limit ourselves to the hole doping. The electron and hole doped Mott insulators have similar global phase diagrams, yet with pronounced asymmetry, e.g. in the stability of the superconducting phase [8].

From a theoretical viewpoint, solving the ground state (and the excited states) of doped Mott insulator is formidable. For a start, as a single hole starts to hop in the antiferromagnetic background (in the dilute hole doping limit), it creates a local spin mismatch (Figure 4.3 **a**), with a high energy cost on the scale of $2J$. Also, as the hole moves around the lattice plaquette and returns where it was (as in the time-dependent path integral formulation), the topological nature of the two-dimensional space allows spontaneous generated vortex (pairs)[1] . There are again the possibilities of dimerized states, prepaired resonating valence bond states, among others; and we have not yet started to consider the lattice phonons and charge/orbital-density waves. Despite increasing computing power, numerical modeling of the doped $t - J$ model has been applied only to a limited number of sites [107].

As it is impossible to conduct an exhaustive review of existing theories, we will focus on (1) the chemical potential shift and (2) influential interpretations of the phase diagram. Experimental and theoretical surveys [109, 110, 108, 111] have both yielded conflicting views on the chemical potential shift. We show the two main scenarios in Figure 4.3 **b**. The first possibility is that the chemical potential moves immediately to the LHB. Different from regular semiconductors, there is transfer of spectral weight from the UHB to the LHB. Specifically, if one hole is doped into the

---

[1] The theory of self-generated magnetic flux was quite popluar in the mid 1990s, under the name "anyon statistics" [106]. However, these theories did not find much experimental support.
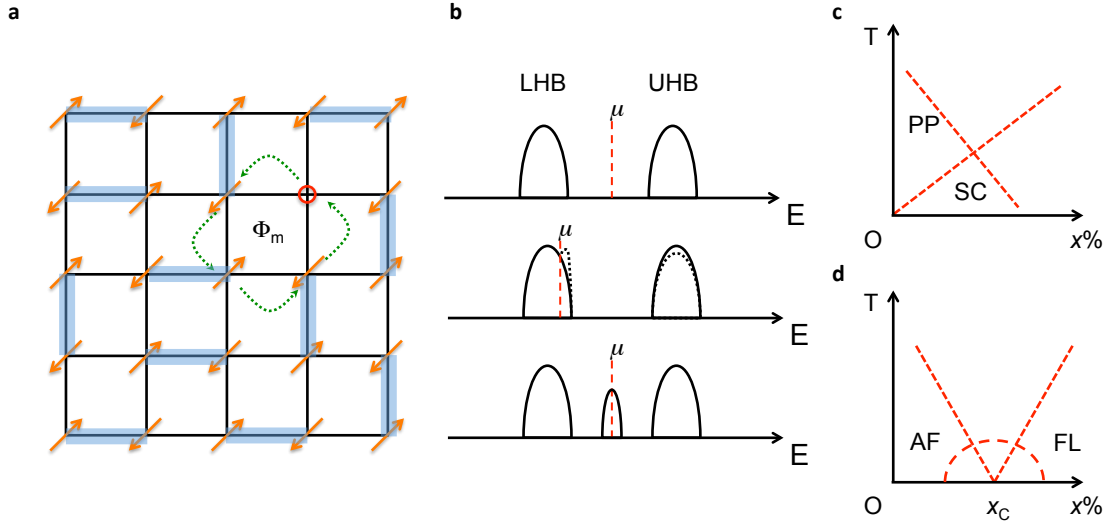
Figure 4.3: Theoretical explorations of the doped Mott insulator on a square lattice. **a**. Cartoon of a doped Mott insulator, with one hole on it. The hole could move and cause a spin mismatch. Also there is the possibility of spontaneous vortices appearing in the system. The thick blue bars connect local fluctuating spin singlets. **b**. Possible schemes for chemical potential shift in the doped Mott insulator. The dashed red lines are the Fermi levels. Similar to [108]. **c**. Proposed phase diagram from the pre-pairing (PP) picture. SC stands for the superconducting phase. **d**. Proposed phase diagram of the quantum critical point (QCP) picture. AF and FL stand for the antiferromagnetic phase and the Fermi liquid phase. The critical doping is marked by x_C. The SC is the dome shaped region.

LHB, there are two ways of adding an electron (with spin up/down) to combine with the hole. Thus there are x states transferred from UHB for the x holes doped, and the LHB comes with a total of $1 + x$ states. The other often mentioned possibility is both the LHB and UHB transfer states into the middle of the gap, and the chemical potential is pinned to the in-gap states and there is no sudden change of chemical potential relative to the parent compound.

Now we introduce two of the most influential theoretical phase diagrams, without explaining the details: the pre-pairing picture (as discussed by Anderson [91], Kotliar [101], Lee and Nagaosa [102], shown in Figure 4.3 **c**) and the quantum critical point (QCP) picture (as adopted by Laughlin [112], Sachdev [93], as shown in Figure 4.3 **d**).

In the pre-pairing picture, there are a large number of pre-paired (PP) and incoherent spin singlets (as in Eqn.(4.1)) bouncing around on the lattice (Figure 4.3 **a**) in the undoped Mott insulator. In the pre-pairing phase, an increasing number of doped holes disrupt and eventually kill the spin-singlets, leading to the suppression of the PP phase. On the other hand, as the hole concentration increases, the spin-singlets are delocalized and start to gain phase coherence. The superconductivity comes from the condensation of pre-formed and coherent spin-singlets. Historically, Kotliar *et al.* [101] have successfully predicted the d-wave pairing symmetry in cuprates in the PP picture.

The QCP picture suggests a quantum critical point exists at 0K between the undoped Mott insulator and the highly doped Fermi metal. The antiferromagnetic and the Fermi liquid phases at finite temperatures are the thermal fluctuations of the corresponding order parameters at 0K. The superconductivity arises from the two strongly competing orders and protects the QCP. There were some experimental observations [113, 114, 115], but none of them were conclusive.

Chapter 5

Doping the Spin-Orbital Coupled Mott insulator Sr_2IrO_4
Universalities and New Opportunities

The 4d and 5d transition metal oxides have attracted a lot of attention over the past few years. As the 4d/5d orbitals are more extended in real space compared to their 3d counterparts, the energy scales of the Coulomb repulsion U, crystal field splitting E_{CF} and electron hopping t are comparable. In addition, the increase in the atomic number of the transition metal element accompanies a new energy scale — the spin-orbit coupling, which is on the same order as U, E_{CF} and t. The competition among the above-mentioned interactions, together with the possibility of tuning these interactions, provides a versatile playground for realizing many novel exotic phases of matter, including high-T_C superconductors [116], spin liquids [117], correlated topological insulators [118, 119] and Weyl metals [120].

In this chapter we study a new family of Mott insulator Sr_2IrO_4 with an effective total angular momentum J_{eff}=1/2 [4, 69], and demonstrate how this novel spin-orbital coupled Mott insulator helps identify universal features during the Mott-metal crossover. By universality we refer to the low-energy properties that do not depend on the details of the interactions. For materials with relatively weak electron correlations, the low-energy excitations are well described by the Fermi liquid theory. For doped Mott insulators where correlations are strong, pinpointing the hallmarks common to all Mott-metal crossovers has proven a formidable task [76]. This could largely be attributed to the long candidate list of competing electronic orders, including long-range magnetic order and Fermi surface instabilities, among others, which yields a complex global doping-

temperature phase diagram. It becomes inseparable whether such exotic phenomena as pseudogaps [77, 121] and marginal Fermi liquid scattering rates [22] arise from the metal-insulator transition, certain density-wave instabilities or are fluctuations of the superconductivity. Moreover, the charge insulation in most known Mott insulators arises solely from the Coulomb repulsion. Thus studying doped Sr_2IrO_4 may be very valuable, as this material system has a cleaner phase diagram (thus fewer competing orders) and a different mechanism that forbids electron double-occupancy.

We focus on the evolution of electronic structure and dynamics of the hole-doped Sr_2IrO_4. The effective hole doping is achieved by replacing Ir with Rh atoms, with the chemical potential immediately jumping to or near the top of the lower Hubbard band. The doped iridates exhibit multiple exotic features previously observed in doped cuprates [76, 8, 78, 77, 22] – pseudogaps, Fermi arcs, and marginal-Fermi-liquid-like electronic scattering rates. We argue these universal features of the Mott-metal crossover are not related to preformed electron pairing, quantum criticality or density-wave formation as discussed in Chapter 4. Instead, short-range antiferromagnetic correlations may play an indispensible role.

5.1   Essence of the Spin-Orbital Coupled Mott Insulator

Sr_2IrO_4 is often referred to as a spin-orbital coupled Mott insulator with an effective J=1/2 [69, 4]. In this section we discuss the essence of this new concept. The key messages are (1) $J_{eff}=1/2$ is a local description of valence electrons on the Ir atom, and (2) globally the high-energy interactions between electrons in the antiferromagnetically ordered Sr_2IrO_4 are very different from those in traditional Mott insulators.

The crystal structure of Sr_2IrO_4 is displayed in Figure 5.1 **a**. Each iridium atom sits at the center of a Ir-O octahedra, with a Ir-O-Ir bond angle of 22° between adjacent Ir octahedras. The nature of the insulator could be understood in terms of the Ir 5d level splitting, by taking into account the role of spin-orbit coupling and Coulomb repulsion. We visualize the analysis in Figure 5.1 **b**. Due to the crystal field splitting, the 5 electrons in the 5d orbital occupy the t_{2g} levels, with the higher-in-energy e_g levels empty. The Ir t_{2g} level splits into the $J_{3/2}$ doublet (filled with 4

electrons) and the $J_{1/2}$ singlet as a result of the strong spin orbit coupling ($\sim$0.4eV). The half-filled $J_{1/2}$ further splits into lower (filled with 1 electron) and upper (empty) bands, with this splitting general believed to be due to the Coulomb repulsion, which is why these bands should be considered upper and lower Hubbard bands (LHB and UHB).

It is often said the LHB and UHB in iridates have an effective total angular momentum of J=1/2. However, the iridate only has finite crystal rotations (as opposed to the case of topological insulators near the Γ point, where infinitesimal rotations are possible, see Chapter 3 for details). Therefore the existence of an effective total angular momentum appears non-trivial.

The experimental evidence of the J=1/2 character comes from the Resonant X-ray Scattering (RXS) at the Ir L-edge, where the magnetic reflection at (1 0 2n) (with n being an integer) is suppressed (Figure 5.1 **c**). The principle of the resonant X-ray scattering is drawn in Figure 5.1 **d**. The photon resonantly pumps the Ir 2p core electron to the empty energy levels immediately above the Fermi level, leaving behind a core hole. A photo-detector collects the out-going photon intensity generated from the recombination between the core hole and the valence electron near E_F. The resonant photon energy is determined by the peak value of the X-ray Absorption Spectroscopy (XAS). The RXS intensity peaks at the lattice/electronic ordering vector, similar to the Bragg scattering. The overall cross-section of the RXS follows the same dipole transition rule as in the hydrogen atom. A detailed review of the RXS is available in [122].

For the Ir atom, as the unoccupied states immediately above the Fermi energy comes from the Ir 5d orbitals, the dipole-allowed optical transition is between the Ir 2p and 5d states. Specifically, the Ir L_2 and L_3 edges correspond to the dipole transition between the unoccupied Ir 5d states and Ir $2p^{1/2}$ and $2p^{3/2}$ core levels respectively. Experimentally, the RXS peak at the magnetic reflection (1 0 2n) (with n being an integer) is suppressed *only* at the Ir L_2 edge. This could not be explained in conventional RXS theories. Kim *et al.* [69] suggested the optical pump from the L_2 edge is forbidden since the empty state above E_F has an effective total angular momentum, rather than the orbital angular momentum seen in other materials. Moreover, Kim *et al.* [69] was able to
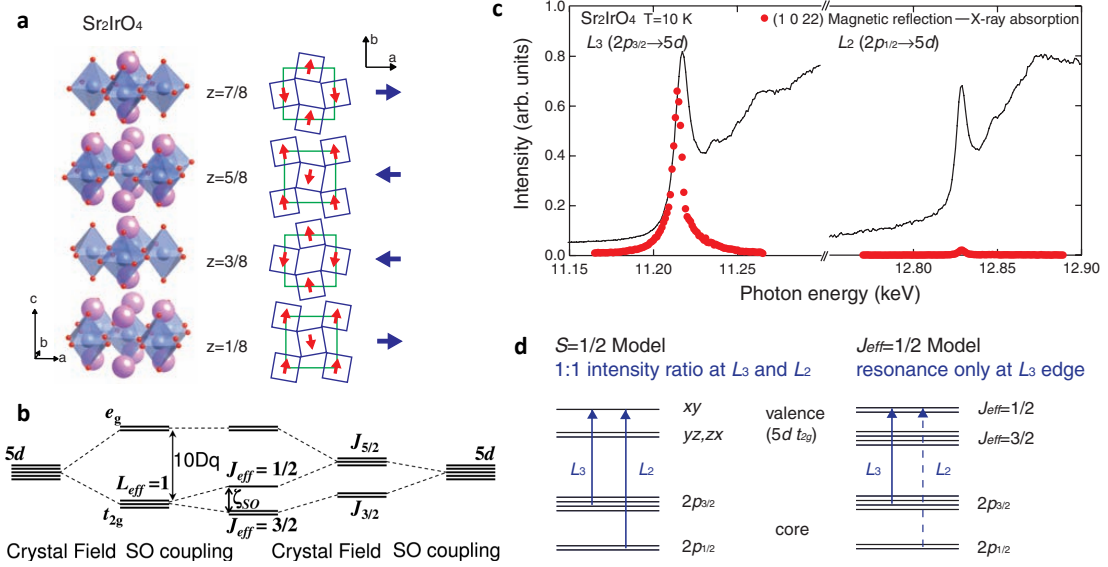
Figure 5.1: Sr_2IrO_4 as a Mott insulator with $J_{eff}=1/2$. **a.** Layered crystal structure of Sr_2IrO_4. The blue, red, and purple spheres represent Ir, O, and Sr atoms, respectively. **b.** Canted antiferromagnetic order of $J_{eff}=1/2$ moments (arrows) within IrO2 planes and their stacking pattern along the c axis in zero magnetic field. **c.** X-ray absorption spectra (solid lines) and resonant X-ray scattering intensity (dotted lines) at the Ir L-edge. The resonant X-ray scattering signal is taken at the magnetic reflection (1 0 22). **d.** For an Ir atom with spin 1/2, the calculated resonant X-ray scattering intensities at L_3 and L_2 should be almost equal. For the $J_{eff}=1/2$ model, in contrast, the resonant scattering intensity is only enhanced at the L_3 edge, and is expected to be zero at the L_2 edge. The panels **a**, **c** and **d** are reproduced from [69], and panel **b** is from [4].

decide the wavefunction of the empty states derived from the Ir 5d level, with

$$|J_{\text{eff}} = 1/2, m_{\text{eff}} = \pm 1/2\rangle = \frac{1}{\sqrt{3}}(|xy, \mp\sigma\rangle \mp |yz, \pm\sigma\rangle + i|zx, \pm\sigma\rangle) \qquad (5.1)$$

Note the empty states accessed by the RXS are atomic-like, and do not have any k-dependence. However, first-principles calculations (which we will discuss later in this Section) have yielded a conduction band that disperses in k.

The discrepancy about the empty states above E_F could be explained by revisiting the nature of the RXS process. The 2p core electrons are spatially confined near the center of the atom, and the momentum of the 2p electron has a large uncertainty. Thus the momentum of the photo-pumped (with a >11keV photon and large momentum transfer) electron in the conduction band is also not defined. Essentially the $J_{\text{eff}} = 1/2$ state the RXS probes is a local state from the sampling of the k-dispersed conductions band states.

We could also interpret the $J_{\text{eff}} = 1/2$ state as an intermediate (and even transient, as the 2p core hole lifetime could be very short) state in the local crystal field enviornment, without knowing the overall band structure. This suggests the $J_{1/2}$ is incredibly fragile. A slight change to the crystal field (e.g. with octahedra stretched along the apical oxygen) might lead to the collapse of the effective J state, as the three t_{2g} orbitals are no longer equally weighted. This has been experimentally shown by applying external pressure to Sr_2IrO_4 [123]. Also the k-space Bloch wavefunction of the $J_{1/2}$ band could be viewed as a linear combination of $J_{1/2}$ states from individual Ir atoms. However, the relative amplitude and phase among the three t_{2g} orbitals for these Bloch wavefunctions would probably deviate from Eqn. (5.1), maybe except at high-symmetry k-points. First-principles analysis as we have done in Chapter 3 could be performed to check the validity of this claim.

The ARPES spectrum of Sr_2IrO_4 has a somewhat well-defined band structure of both the LHB and the $J_{\text{eff}} = 3/2$ band, as shown in Figure 5.2 **a** and **b**. Due to the $\sqrt{2} \times \sqrt{2}$ lattice recon-struction in the bulk materials, the Brillion zone of Sr_2IrO_4 folds. The high-symmetry points X and M in the folded Brillion zone correspond to the $(\pi, 0)$ and $(\pi/2, \pi/2)$ momentum in k-space. There

is no band crossing the Fermi level, which is consistent with the insulating behavior. Moreover, the calculated band structure using LDA (Local Density Approximation) + SO (Spin-Orbit coupling) + U with U=2.0 eV and SO=0.4 eV matches the experimentally determined dispersion reasonably well, without major band shifting or renormalization[1] . Apprantly first-principles calculations need to take into account both SOC and U to get to get a finite band gap, which is different from the case of cuprates and many other Mott insulators. This is illustrated in Figure 5.2 **c**.

The agreement between ARPES measurement and band calculations may seem surprising for correlated electron materials, which are usually believed to have reduced band width relative to the LDA calculations. However, even for "classical Mott insulators" such as La_2CuO_4, the density functional calculations have achieved qualitative agreement with experiments [125, 126]. As discussed in Chapter 4, this comes in part from improved approximation to the correlation integral, and more importantly, from the formation of the folded antiferromagnetic Brillion zone. The lack of band renormalization in Sr_2IrO_4 may be a simple result that band width and Coulomb repulsion are comparable. We also need to keep in mind that "strong correlation" is reflected not only in the band width, but also in the electron scattering rate. We will focus on both aspects for the rest of this chapter.

5.2   Evolution of the Band Structure with Effective Hole Doping

Sr_2IrO_4 emerges as a new family of Mott insulators. The Ir-O planes are similar to the Cu-O planes in cuprates, with the Ir atoms antiferromagnetically ordered and located at the center of the Ir-O octahedra [127]. Driving Sr_2IrO_4 towards metallicity thus provides a unique opportunity to investigate the universal features of the Mott-metal crossover. Different approaches of doping Sr_2IrO_4 have been found [128, 129, 130, 131], and of special interest is the $Sr_2Ir_{1-x}Rh_xO_4$ series. The transport, magnetization and photoemission results shown in the rest of this chapter were

---

[1] In the ARPES data shown in Figure 5.2 **a**, the valence band at Γ has higher binding energy than that at X, while the energies at Γ and X are about the same in the calculation (Figure 5.2 **c3**). Further details are presented in [124] These seemingly minor details affect the thermal activation of electrons across the gap, which could be measured in transport experiments
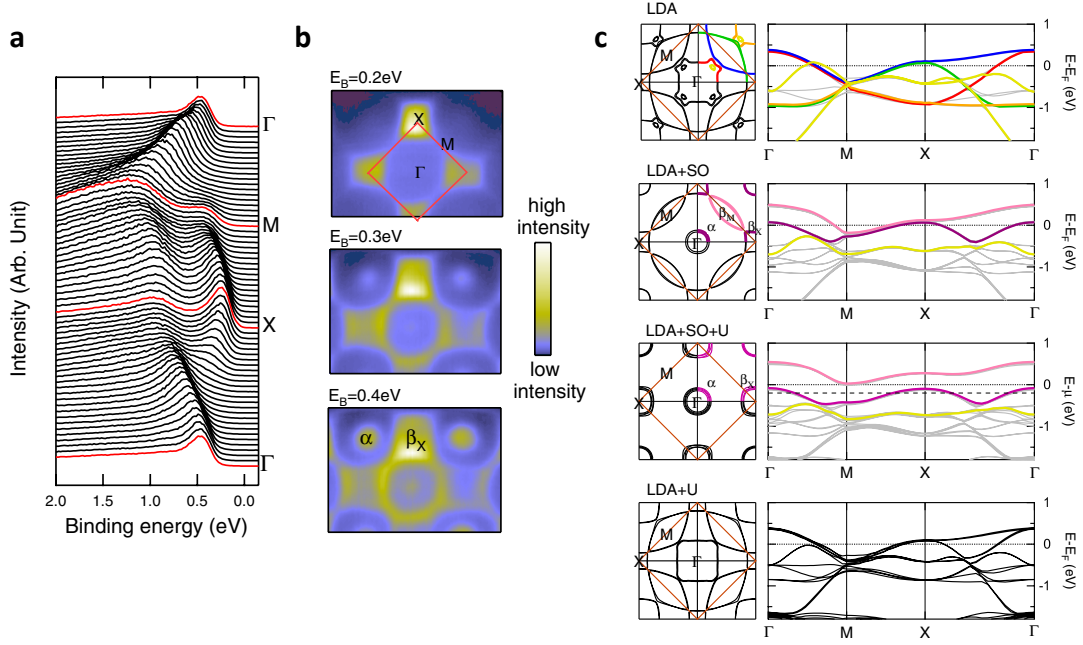
Figure 5.2: The measured and calculated band structure of Sr_2IrO_4. **a**. The EDC along high symmetry directions in k-space and **b**. constant energy intensity maps of Sr_2IrO_4. **c**. The Fermi surface topology (left column) and band structure (right column) calculated using (from top to bottom) LDA, LDA+SOC, LDA+SO+U (where the constant energy surface 200meV below E_F is shown), and LDA+U. The SO=0.4eV and U=2eV in all calculations. The panels are reproduced from [4].

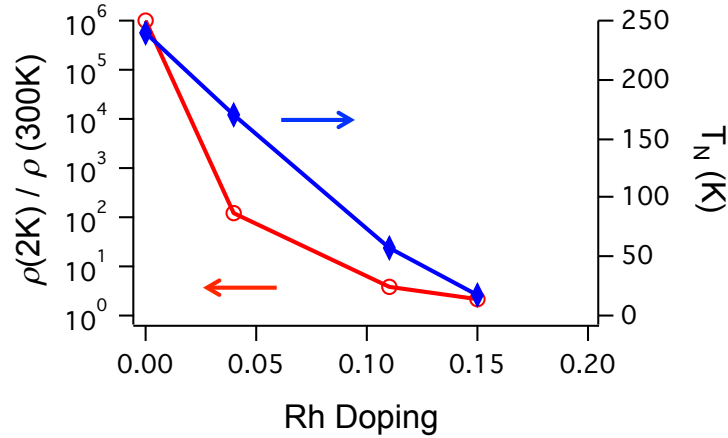Figure 5.3: The evolution of resistivity and magnetism of $Sr_2Ir_{1-x}Rh_xO_4$ as a function of Rh doping. The left axis: the normalized resistivity; and the right axis the onset of the long-range magnetic order.

performed on bulk single crystal $Sr_2Ir_{1-x}Rh_xO_4$ samples.

In Figure 5.3, we show the normalized resistivity (left axis) and the onset temperature of the long-range magnetic order (right axis) as a function of Rh concentration. With as little as 4% Rh substitution, the normalized resistivity drops by 10^4. The long-range magnetic order decays more slowly[2] and still survives with a $T_N \sim 17K$ for 15% Rh [130]. The long-range antiferromagnetism manifests itself as weak ferromagnetism in the magnetic susceptibility, due to the canted Ir moment in the Ir-O plane. This is also why we refer to the onset temperature (of weak ferromagnetic order) as the Neel temperature.

Rh is directly above Ir in the periodic table, so is expected to be isovalent. It has been proposed that the metallicity in the Rh doped iridates comes from the reduced spin-orbit coupling of Rh (due to the smaller atomic number) which then leads to the reduced splitting of the $J_{3/2}$ and $J_{1/2}$ bands [130, 131] as well as the formation of in-gap states [131] (Figure 5.4 **c3**). As we will show below, the Rh atoms in fact act as effective hole dopants to Sr_2IrO_4 (Figure 5.4 **c2**). So far, no superconductivity has yet been reported in these Rh doped compounds, which is different from doped cuprates. The absence of superconductivity reduces possible competing orders and makes the Rh doped iridates a cleaner system to study – the long-range canted antiferromagnetism is the only confirmed order in the system.

We performed ARPES on single crystals of Rh doped Sr_2IrO_4. The samples were cleaved *in situ* with vacuum better than 5×10^{-11} Torr. The band structure and low-energy spectra near the Fermi level were taken with photon energies of 77eV, 80eV, and 90eV, with an energy resolution $\sim 25meV$.

The $\sqrt{2} \times \sqrt{2}$ lattice reconstruction appears in both the parent Sr_2IrO_4 and the Rh-doped materials. This leads to the folding of the Brillion zone (BZ) in a similar way that the antiferromagnetic order in the parent cuprates gives a zone doubling. We show the lattice structures (Figure 5.4 **a**) and the constant energy surfaces (Figure 5.4 **b**) of both Sr_2IrO_4 and as a comparison, of Pb

---

[2] A spoiler: Sr_2IrO_4 is effectively hole doped when replacing Ir with Rh. The resistivity/magnetism phase diagram in the $Sr_2Ir_{1-x}Rh_xO_4$ shares intriguing similarity to the phase diagram, e.g. of $(La_{1-x}Sr_x)_2CuO_4$ [98]. It would seem plausible this kind of phase diagram might be intrinsic in the doped Mott insulators.
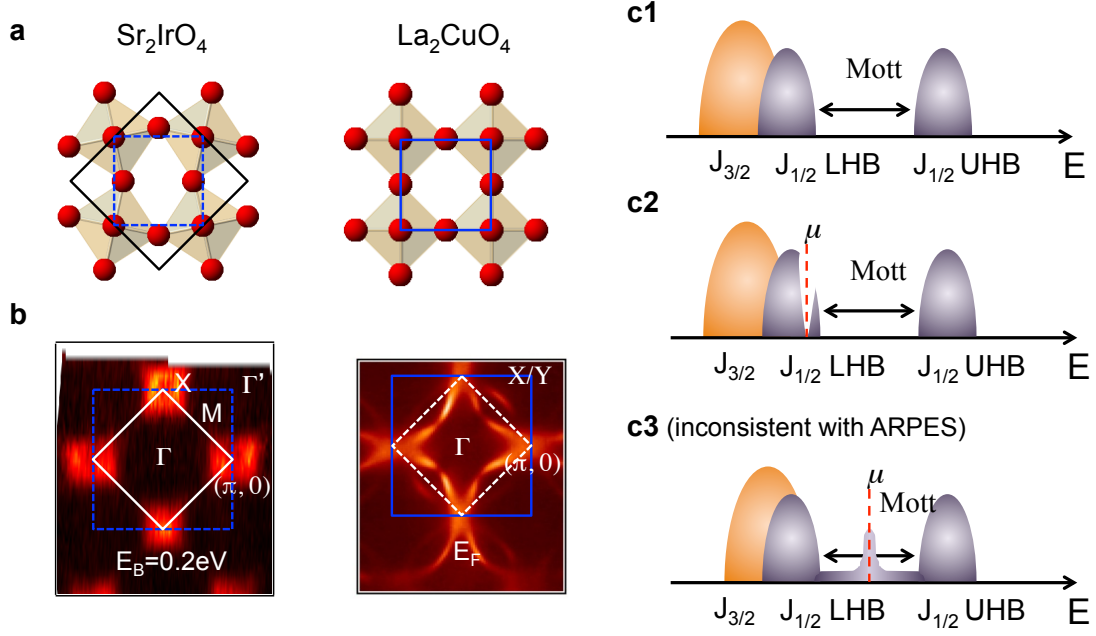
Figure 5.4: Sr_2IrO_4 as a Mott insulator on the square lattice. **a**. The real-space unit cells of Sr_2IrO4 and La_2CuO_4, only showing the transition metal-oxygen layer. **b**. The k-space unit cells of the same, with matching color-scaling and with near-E_F ARPES spectral weight. Igonoring the 22^circ Ir-O twists gives the blue cells in real and k-space, and corresponds to the regular unit cell of La_2CuO_4. Including these twists in Sr_2IrO_4 (black, panel **a**) back-folds the k-space cell in k-space (white), similar to the AF order in the parent cuprates. **c1**. The formation of the Mott gap in Sr_2IrO4 as a result of the spin-orbit coupling and Coulomb interaction. **c2**–**c3**. Schematics of possible evolution of the chemical potential with Rh doping.

doped $Bi_2Sr_2CaCu_2O_{8+\delta}$. The folded and "original" Brillion zone for the iridates are marked in white solid and blue dashed lines, respectively. The "original" Brillion zone corresponds to an Ir-O plaquette in real space, as shown by the blue dashed line in the left panel in Figure 5.4 **a**. As we will show later in the paper, the low energy features of the doped iridates are best captured not by the folded Brillion zone, but instead by the "original" blue Brillion zone. To avoid confusion, we use $(\pi, 0)$ to mark the X point in the Brillion zone as defined in [4], and use Γ' to denote (π, π), which is the Γ point in the 2nd folded Brillion zone.

In Figure 5.5 **a** and **b**, we show the constant energy surfaces as a function of binding energy for Sr_2IrO_4 and $Sr_2Ir_{1-x}Rh_xO_4$ with x=15% at T=50K. While there is no Fermi surface for the parent compound, there are states at the Fermi level in the x=15% iridate, corresponding to enhanced conductivity in the Ir-O plane. The constant energy surface of the x=15% compound is quite similar to that of the parent, except that it is shifted in binding energy by 200meV. To identify the Fermi surface topology, we plot the ARPES spectrum along Γ'-$(\pi, 0)$ for both samples (Figure 5.5 **c**) (along the yellow lines in Figure 5.5 **a** and **b** panels). There is a hole-pocket centered at $(\pi, 0)$, which comes from the $J_{1/2}$ LHB [4, 124]. The top of the valence band is $\sim$180meV below E_F in the parent compound, and is above the Fermi level for the x=15% sample. Indeed, both the $J_{3/2}$ band (white dashed line in Figure 5.5 **c**) and $J_{1/2}$ LHB (green dashed line) [132, 133] are shifted by $\sim$200meV.

The shift of the chemical potential is better illustrated by taking the second derivative of EDCs along the high symmetry directions of the Brillion zone in Figure 5.5. This technique is routinely used to highlight the band dispersion in ARPES experiments [134, 135, 136]. For both the parent compound and the x=15% sample, the $J_{1/2}$ LHB and $J_{3/2}$ band are drawn in dashed green and red lines respectively. It is evident that both the $J_{1/2}$ LHB and $J_{3/2}$ band move towards E_F, with neither major relative shift between these two bands nor bandwidth renormalization. Note that while the Rh doped compound displays strong spectral weight extending towards $(\pi/2, \pi/2)$ (the M point) near E_F, the band dispersion at the M point lies below E_F. Therefore, the "Fermi surface" is made up only of the states encircling X or $(\pi, 0)$, i.e. it encompasses holes. To

conclude, rather than a reduced splitting of the $J_{3/2}$ and $J_{1/2}$ bands as would have been expected from reduced spin-orbit coupling, we observe that Sr_2IrO_4 is hole doped with Rh substitution.

The chemical potential shift could be determined quantitatively from the valence bands. As shown in Figure 5.7, with the increase of Rh concentration, the chemical potential is pushed deeper into the $J_{1/2}$ LHB, confirming that Rh acts as an effective hole dopant. We extrapolate the chemical potential shift at finite Rh densities and derive a ~180meV intercept in the zero doping limit. Note the top of the valence band in the parent compound locates at $(\pi, 0)$ and is around 180meV below E_F, from both ARPES [124] and STM [137] experiments.

The abrupt change in the chemical potential demonstrates that the chemical potential immediately jumps to the edge of the lower Hubbard band (Figure 5.4 **c2**), as opposed to competing models (Figure 5.4 **c3**) [131, 110] where new quasiparticle-like states emerge in the middle of the Hubbard gap.

The doping schematic in Figure 5.4 **c2** also agrees with the recent optical conductivity measurements [131]. Indeed, the optical conductivity experiments could not distinguish between the two scenarios in Figure 5.4 **c2** and **c3**. The α and β transition peaks seen in the optical conductivity are interpreted as the optical transition from the $J_{1/2}$ LHB and $J_{3/2}$ band to the $J_{1/2}$ UHB, respectively. For Rh concentrations less than 20%, the α and β peak locations do not change – an indication there is not much relative shift between the $J_{3/2}$ band and $J_{1/2}$ Hubbard bands. This is consistent with both scenarios in Figure 5.4. The ARPES experiment as presented here, however, unambiguously shows that there is a sudden jump in the chemical potential, thus ruling out the scenario with the in-gap state as shown in Figure 5.4 **c2**. Moreover, the low energy peak that appears below the α peak in the Rh substituted samples could also be explained in Figure 5.4 **c2**. As we will discussion in Section 5.3, there is suppression of spectral weight near E_F for the Rh doped samples. Thus the low energy peak might originate from the intra-band optical transition across the pseudogap, without introducing any in-gap states as in Figure 5.4 **c3**.

The effective hole doping is quite plausible when considering the simple atomic model depicted in Figure 5.7 **b**. Rh atoms have smaller spin orbit coupling than Ir, leading to the smaller splitting
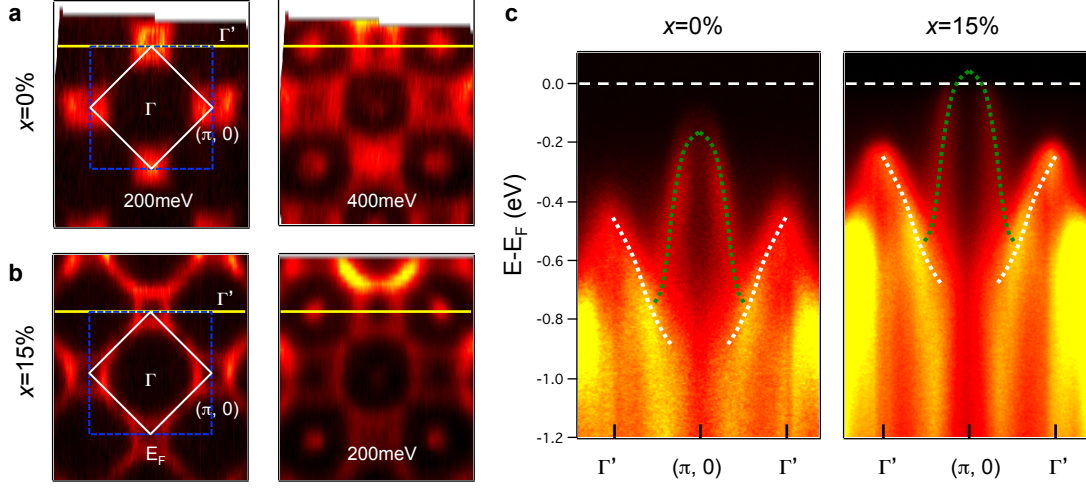
Figure 5.5: Constant energy surfaces and high symmetry cuts of the parent and Rh doped Sr_2IrO_4. **a.** and **b.** The constant energy surfaces of the parent (**a**) and x=15% Rh substituted (**b**) Sr_2IrO_4. The numbers are binding energies relative to E_F. The solid white / dashed blue lines are the folded / original BZs. **c.** ARPES energy-momentum intensity plots along Γ'-$(\pi, 0)$-Γ' (yellow lines in panels **a** and **b**). The dashed green and white lines through the data guide the eye for the $J_{1/2}$ and $J_{3/2}$ bands respectively.
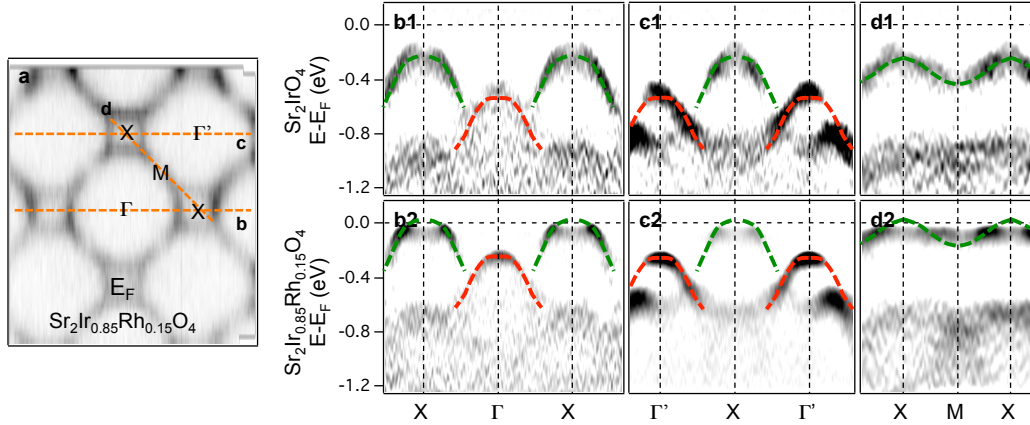
Figure 5.6: Comparing the band structure along high symmetry directions in the parent and Rh doped Sr_2IrO_4. **a.** The Fermi surface topology of the x=15% Rh-doped sample. The high symmetry cuts in panels **b** to **d** are drawn in dashed orange line. **b.-d.** The EDC second-derivative maps for the parent (**b1-d1**) and x=15% Rh-doped sample (**b2-d2**) respectively. The dashed lines are guides to the eye where the green and red colors denote the $J_{1/2}$ lower Hubbard band and $J_{3/2}$ band.
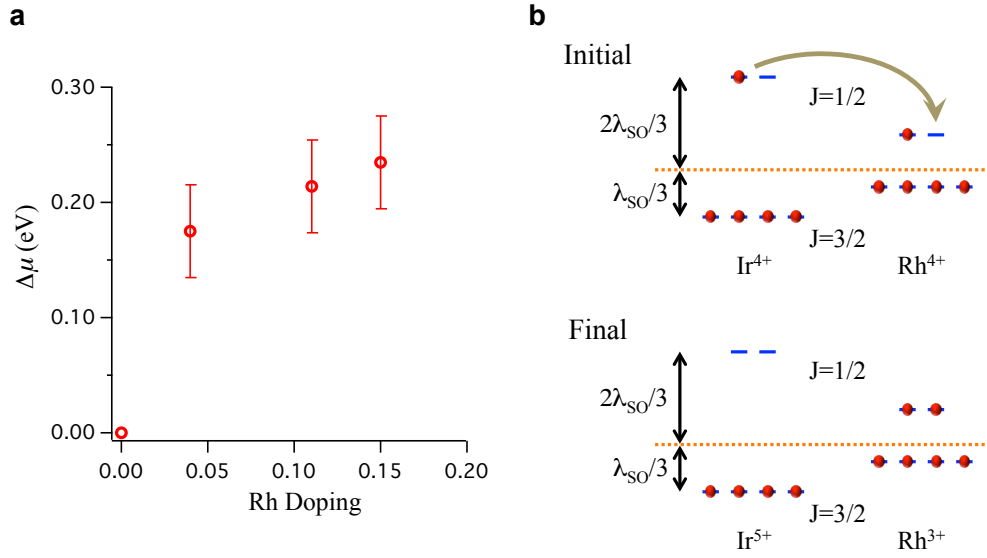
Figure 5.7: Rh atoms act as hole dopants in Sr_2IrO_4. **a**. Chemical potential shift vs. Rh concentration. The chemical potential shift is measured from the shift of both $J_{1/2}$ lower Hubbard band and $J_{3/2}$ bands. **b**. Simple atomic picture of hole doping, ignoring band effects and Mott splitting. With a roughly similar average energy for both Ir and Rh sites, the smaller on-site spin-orbit splitting on the Rh sites lowers the $J_{1/2}$ energy relative to that of the host Ir sites. This causes an electron transfer to Rh, i.e. hole doping of the Ir lattice.

between the $J_{3/2}$ and $J_{1/2}$ states. Assuming the average energy of all 6 t_{2g} states is similar for both Rh and Ir, the empty $J_{1/2}$ state of Rh would then have a lower energy than that of Ir. Thus a $J_{1/2}$ electron from a neighboring Ir atom will fill the $J_{1/2}$ state on the Rh site, leaving behind a hole on the Ir site, as well as a filled and immobile Rh^{3+} site. Of course this is a simplistic model that neither takes into account the finite bandwidth of the effective J states nor the Coulomb repulsion U. Recent X-ray absorption experiments at the Rh L_3-edge have also confirmed Rh has a valence of 3+ in these compounds [138].

5.3   Low-energy Electron Dynamics in the Hole Doped Sr_2IrO_4

Hereafter we focus on the low-energy electronic dynamics of these hole-doped compounds in search for "universal" features during the Mott-metal crossover. In Figure 5.8 **a** we show the Fermi surface topology for the x=15% sample at 50K. The segments of the Fermi surface centered at Γ (Γ') and equivalent k locations are highlighted with solid yellow (blue) lines, and labeled FS1 and FS2, respectively. EDCs from many different k points on the Fermi surface are plotted in Figure 5.8 **b**. There is a dramatic difference between the EDCs from FS1 and FS2 – those from FS2 are generally pushed away from E_F.

We use the standard "midpoint of leading edge" method [95, 139] to quantify the spectral weight suppression, by fitting the EDCs to the shifted, broadened leading edge function below, with the amount of shift (defined as the gap size) giving the 50% point of the leading edge

$$BG + \frac{A + B\omega}{1 + e^{(\omega+\Delta)/k_B T^*}} \tag{5.2}$$

Eqn. (5.2) is essentially a Fermi function with variable edge width $k_B T^*$ and with the leading edge midpoint shifted from the chemical potential by the pseudogap value Δ. We use a constant BG to describe the spectral weight above E_F, and A, B are fitting coefficients.

Note that in contrast to the case of a BCS-like gap that works well for superconductivity or a standard charge or spin density wave gap, this shifted edge does not have a pile-up of spectral weight beyond the gap edge, i.e. it does not enforce spectral weight conservation upon the opening

of the gap. Similar broad EDCs have also been observed in lightly doped cuprates [99] as well as manganites [139]. This suggests the effectively hole-doped iridates are certainly not Fermi liquids.

We assign the gap size Δ_1 and Δ_2 from the leading edge fitting to FS1 and FS2 respectively. For x=15%, Δ_1 as defined by this leading edge method vanishes, and FS1 can be considered a regular piece of Fermi surface, while EDCs from FS2 show a partial depletion of near-E_F spectral weight. As FS1 is only topologically connected to the "gapped" FS2, we describe the FS1 as a Fermi surface "arc" and FS2 as "pseudogapped".

We track how Δ_1 and Δ_2 evolve with reduced Rh concentration, as the material gets closer to the Mott insulator. At x=4% (Figure 5.8 **c**), both Δ_1 and Δ_2 are finite, indicating that both FS1 and FS2 are pseudogapped, with $\Delta_1 \sim$3meV and an increased $\Delta_2 \sim$38meV. In Figure 5.8 **d** we plot the doping dependence of Δ_1 and Δ_2. For x=4%$\sim$<11%, the entire Fermi surface is pseudogapped, which resembles the ultra-underdoped cuprates where a second pseudogap (on top of the preparing pseudogap and above the superconducting transition temperature) affects the nodal states [97, 96]. We mark the presence of both pseudogaps as suppressed spectral weight near E_F (the notch) in Figure 5.4 **c2**. The pseudogaps observed here are not to be mistaken for the matrix element effect as these pseudogaps happen over a very narrow binding energy range that is essentially identical for different photon energies.

The pseudogap phase is often considered a symmetry-broken phase of matter. Thus the origin of the pseudogap could be reflected in its k-space symmetry as well as its thermal evolution. For Rh concentration 4%$\sim$15%, Δ_1 (Δ_2) is roughly independent of k along the Fermi surface segment FS1 (FS2). In this sense, the pseudogaps in the non-superconducting Rh-doped iridates are clearly different from the near-nodal prepairing pseudogap in the near-optimal cuprates [23], where pseudogaps follow the superconducting pairing symmetry.

Figure 5.8 **e** shows the temperature dependence of EDCs at k_F from FS1 and FS2 for the x=11% sample, with the temperature range straddling the AF ordering temperature T_N=57K. Within the error bar no obvious changes with temperature are observed, indicating that the pseudogap is not directly related to the long range canted AF order. This is further confirmed in the
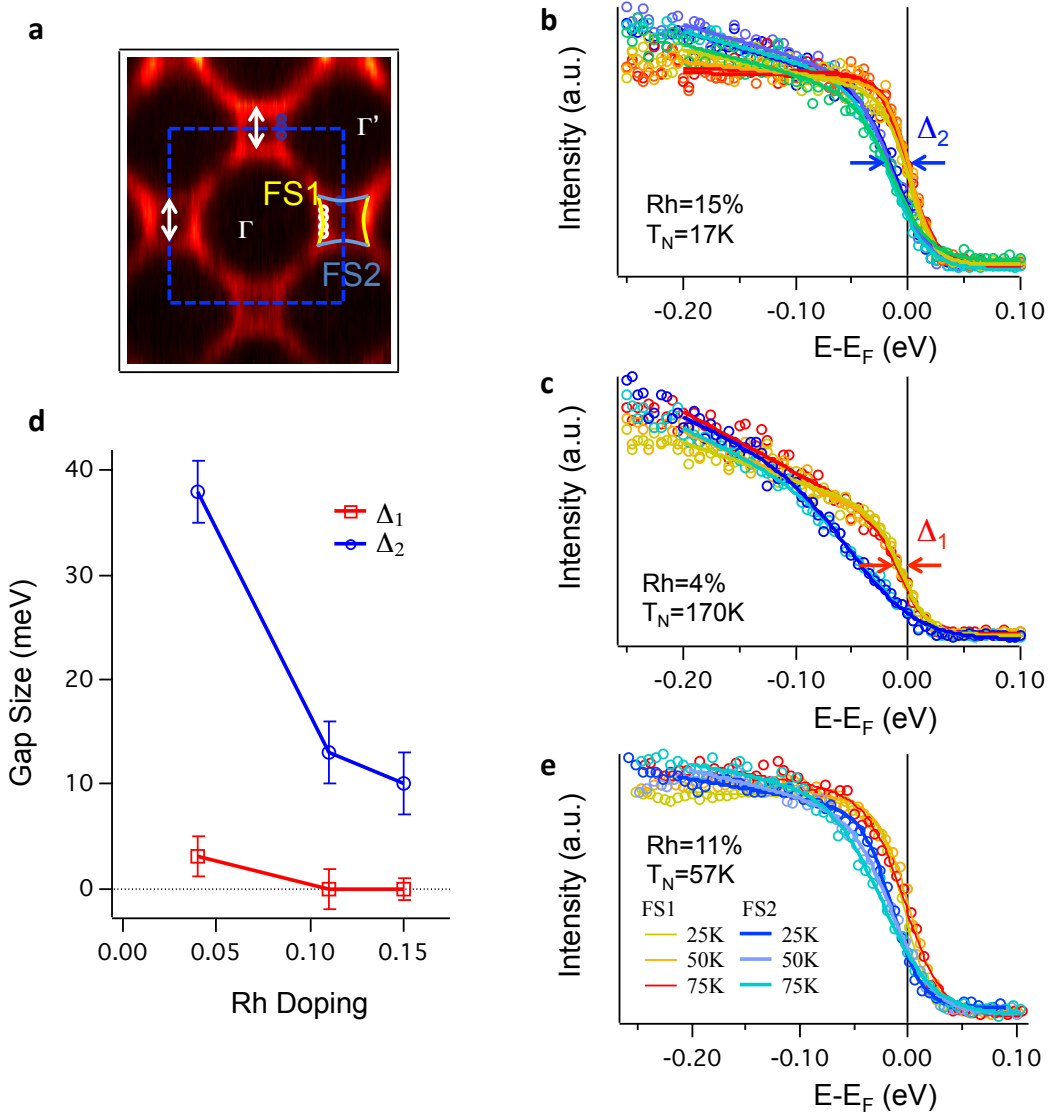
Figure 5.8: Fermi surface segments and pseudogaps in Rh-doped Sr_2IrO_4. **a**. Fermi surface spectral weight of the x=15% sample, with a hole-like Fermi pocket centered around the $(\pi,0)$ point of the unfolded (blue dashed) BZ. The FS pocket is separated into segments FS1 (yellow) and FS2 (blue), with FS1 facing Γ and FS2 facing Γ'. Q vectors (white arrows) are possible density-wave nesting vectors. **b** and **c**. EDCs from multiple locations along the FS1 and FS2 segments (yellow and blue, respectively) taken from the x=15% and x=4% samples. Locations of the individual EDCs are marked by the open colored circles in panel **a**. The leading edges of most EDCs do not reach E_F, i.e. they are gapped or pseudogapped. Gap sizes extracted using the midpoint of leading edge method, are shown in panels **b** and **c** and compiled in panel **d**, with Δ_1 labeling the gaps from FS1 and Δ_2 the gaps from FS2. **e**. EDCs from FS1 (dashed) and FS2 (solid) showing minimal temperature dependence across the magnetic phase transition of the x=11% sample.

x=15% sample (5.8 **b**), where Δ_2 is finite at 50K, above T_N=17K. This observation clearly suggests the pseudogap is not tied to the long-range magnetic order, and it is likely the pseudogap phase persists down to the zero-temperature quantum ground state in these hole-doped iridates.

Another commonly considered origin of pseudogaps is the density-wave instabilities in the form of Fermi surface nesting, as has been discussed in the manganites and cuprates [139, 140, 104]. In the case of iridates, it is temping to draw nesting vectors such as the white arrows (Figure 5.8 **a**) between FS2's with the same gap size Δ_2. However, the same ordering vector Q also connects FS1's, yet with a much smaller gap Δ_1. The Fermi-surface nesting scenario does not explain the preference for a larger gap along FS2. It appears the iridate pseudogap is different from influential explanations for the antinodal pseudogap [139, 140, 104] in manganites and near optimally-doped cuprates though it may be more connected with the more-recently observed nodal pseudogap in heavily underdoped cuprates [97, 96].

The non-Fermi liquid nature of these doped iridates is not only reflected in the absence of quasiparticle peaks along the EDC (Figure 5.8 **b-c**), but also in the single-electron scattering rate. In the Fermi liquid theory, the quasiparticle scattering rate grows linearly with the binding energy (and temperature) squared. For up to 15% Rh substitution, as shown in Figure 5.9 **b** (with raw data shown in Figure 5.9 **a**) the scattering rates increase roughly linearly with binding energy – a signature of the marginal Fermi liquid [22]. Moreover, from the resistivity curve in Figure 5.9 **c**, there is a linear relation between the scattering rate and the sample temperature, as highlighted by the black dashed line. Here we have ignored the upturn of the resistivity at low temperatures that is likely due to a localization effect, as has also been observed in most of the underdoped cuprates [98]. The linear Marginal Fermi Liquid scattering rate is one of the most iconic features of the cuprates and other correlated materials such as the ruthenates [141] and has been attributed to a wide range of ideas including quantum critical fluctuations [22] and the break-up of quasparticles [142].

Combining the observations presented in Figure 5.8 and 5.9, the hole doped Sr_2IrO_4 apparently shares striking similarities with the doped cuprates, including the presence of pseudogaps and
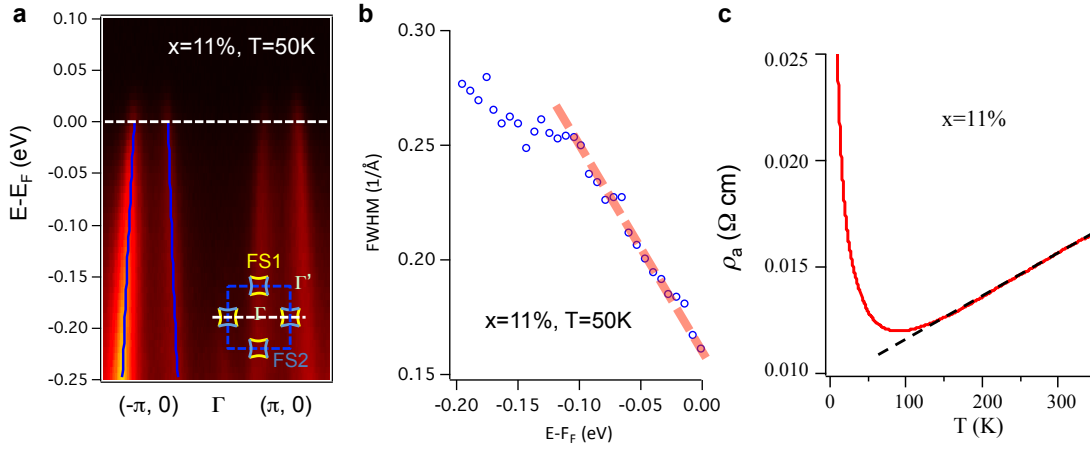
Figure 5.9: Marginal-Fermi-liquid-like electron scattering rates in in Rh-doped Sr_2IrO_4. **a**. The energy-momentum intensity plot along Γ-X=$(\pi,0)$-Γ for an x=11% sample at T=50K, passing through four pieces of FS1 Fermi surface. The peak centroids obtained from MDC double Lorentzian fittings are marked with blue lines. The inset shows where the cut in the main figure is taken from the BZ. **b**. The peak widths (FWHM) from the MDC Lorentzian fitting are plotted vs. the binding energy, showing a linear "marginal Fermi liquid" scattering rate. **c**. Resistivity vs temperature for the same sample showing a linear dependence at intermediate temperatures (black dashed line).

marginal-Fermi-liquid-like scattering rates, despite detailed differences.

Our analysis rules out prepairing and density-wave instabilities as accountable for the pseudogap. Also there is no known quantum critical point in the doped iridates. These are some of the most claimed origins of pseudogaps in cuprates. To identify the origin of these hallmarks in the Mott-metal crossover, we set out to find the common features between iridates and cuprates. While structural distortions appear in both materials, their effect is more likely to be static, and less related to the electron dynamics. We also note that for both materials the parent compound has a long-range AF order that is gradually suppressed with carrier doping. While the pseudogap is not tied to the long-range antiferromagnetism in iridates, the short-range AF correlations that underlie the long-range AF order should still survive regardless of the long-range AF order. Indeed short-range AF correlations may be responsible for many of these hallmarks. For example, short-range AF correlations could indicate a widespread distribution of AF interaction strengths and quantum incoherence, giving rise to the lack of quasiparticle peaks and less well-defined gapping near the Fermi level — a possibility also very relevant for the cuprates and other doped Mott insulators.

We would like to briefly comment on recent debates over whether Sr_2IrO_4 is a Mott insulator or a Slater insulator [143, 144]. The main disagreement between the two types of insulators is the role of short-range AF correlation. The Slater insulator is a mean-field concept that ignores the short-range correlation, or at best considers them as fluctuations of the long-range order. It is expected the gap in a Slater insulator will diminish with decreasing long-range magnetic order, trending to zero as the phase transition is approached. Experimentally, there is no clear change in the band structure for both the parent compound [124, 145] and the doped iridates (this chapter) across the onset of long-range magnetism. This suggests the long-range magnetic order is not necessary for the formation of the gap and Sr_2IrO_4 is a Mott insulator. Moreover, the smooth crossover from the Mott insulator Sr_2IrO_4 to its hole-doped "bad metals"', with the emergence of pseudogaps and marginal Fermi liquid behavior similar to doped cuprates, pinpoints the critical role of short-range correlation in the low energy electron dynamics.

5.4 Universal Features during the Mott-metal Crossover: Beyond ARPES

We compile a list of similarities between iridates and cuprates during the Mott-metal crossover as below:

- The long-range antiferromagnetic order survives at a small but finite hole doping, albeit with a lower Neel temperature.

- The in-plane resistivity drops significantly upon hole doping, and there is an upturn in the low temperature resistivity when cooled towards 0K.

- There is a pseudogap phase that exists above the well-defined ordered phase (being the long-range antiferromagnetism in iridates and superconductivity in cuprates); and in the ultra-low doping limit, the entire Fermi surface is gapped.

- The electron scattering rate is linear in energy close to the Fermi level, accompanying linear-in-temperature resistivity (above the aforementioned upturn temperature).

- The local electron density (as observed in scanning tunneling experiments) for both iridates [146, 147] and cuprates [148] have electronic phase separation.

While the scanning-tunneling experiment in [147] were performed on $Sr_3Ir_2O_7$, our ARPES experiment [124] suggests Sr_2IrO_4 and $Sr_3Ir_2O_7$ are similar, except the latter has splitted $J_{1/2}$ and $J_{3/2}$ bands and reduced dimensionality due to bilayer coupling.

We suggest the above similarities may be universal to the Mott-metal crossover. This argument is highly non-trivial, as the high-energy electron interactions in iridates and cuprates are very different:

- The mechanism that forbids electron double occupancy in cuprates is the Coulomb repulsion, while iridates also need the participation of spin-orbit coupling.

- The spin in cuprates is antiferromagnetically ordered, while the total moment J in iridates

exhibits antiferromagnetism[3] .

Recently, there has been substantial progress in q-resolved resonant inelastic X-ray scattering (q-RIXS) where q denotes the k-space momentum transfer. Dispersive magnetic modes <1eV have been identified in both cuprates [149, 150] and iridates [151, 152]. Combining ARPES and RIXS, we could portrait both the single-particle and collective excitations during the Mott-metal crossover, and investigate, e.g. the role of AF correlations in both materials. Specifically, the high photon energy (and thus large momentum transfer) at the Ir L-edge makes possible mapping the magnetic excitation in the complete q-space. In the upcoming years, combined experimental exploration into these layered iridates under controlled conditions may greatly advance our understanding of the Mott physics.

---

[3] Note in elastic neutron/X-ray scattering, it requires extra work (by measuring the form factor) to distinguish ordered spin moments from ordered J moments

Bibliography

[1] J. Bardeen, L. N. Cooper & J. R. Schrieffer: <u>Physical Review</u> **108** (5), 1175 (1957).

[2] Y. Tokura & N. Nagaosa: <u>Science</u> **288** (5465), 462–468 (2000).

[3] T. Beale, P. Spencer, P. Hatton, S. Wilkins, M. v. Zimmermann, S. Brown, D. Prabhakaran & A. Boothroyd: <u>Physical Review B</u> **72** (6), 064432 (2005).

[4] B. Kim, H. Jin, S. Moon, J.-Y. Kim, B.-G. Park, C. Leem, J. Yu, T. Noh, C. Kim, S.-J. Oh <u>et al.</u>: <u>Physical Review Letters</u> **101** (7), 076402 (2008).

[5] M. Z. Hasan & C. L. Kane: <u>Reviews of Modern Physics</u> **82** (4), 3045 (2010).

[6] T. Das: <u>Scientific Reports</u> **2** (2012).

[7] S. Danzenbächer, D. Vyalikh, Y. Kucherenko, A. Kade, C. Laubschat, N. Caroca-Canales, C. Krellner, C. Geibel, A. Fedorov, D. Dessau <u>et al.</u>: <u>Physical Review Letters</u> **102** (2), 026403 (2009).

[8] A. Damascelli, Z. Hussain & Z.-X. Shen: <u>Reviews of Modern Physics</u> **75** (2), 473 (2003).

[9] S. Hüfner: <u>Photoelectron spectroscopy: principles and applications</u>. Springer (2003).

[10] D. Hsieh, F. Mahmood, J. McIver, D. Gardner, Y. Lee & N. Gedik: <u>Physical Review Letters</u> **107** (7), 077401 (2011).

[11] J. B. Goodenough: <u>Physical Review</u> **100** (2), 564 (1955).

[12] C. Ulrich, L. Ament, G. Ghiringhelli, L. Braicovich, M. M. Sala, N. Pezzotta, T. Schmitt, G. Khaliullin, J. van den Brink, H. Roth <u>et al.</u>: <u>Physical Review Letters</u> **103** (10), 107205 (2009).

[13] J. Schlappa, K. Wohlfeld, K. Zhou, M. Mourigal, M. Haverkort, V. Strocov, L. Hozoi, C. Monney, S. Nishimoto, S. Singh <u>et al.</u>: <u>Nature</u> **485** (7396), 82–85 (2012).

[14] T. Ohta, A. Bostwick, T. Seyller, K. Horn & E. Rotenberg: <u>Science</u> **313** (5789), 951–954 (2006).

[15] A. Bostwick, T. Ohta, T. Seyller, K. Horn & E. Rotenberg: <u>Nature Physics</u> **3** (1), 36–40 (2007).

[16] J. Koralek, J. Douglas, N. Plumb, J. Griffith, S. Cundiff, H. Kapteyn, M. Murnane & D. Dessau: Review of Scientific Instruments **78** (5), 053905 (2007).

[17] M. Seah & W. Dench: Surface and Interface Analysis **1** (1), 2–11 (1979).

[18] C. Berglund & W. Spicer: Physical Review **136** (4A), A1044 (1964).

[19] J. Koralek, J. Douglas, N. Plumb, Z. Sun, A. Fedorov, M. Murnane, H. Kapteyn, S. Cundiff, Y. Aiura, K. Oka et al.: Physical Review Letters **96** (1), 017005 (2006).

[20] A. Gray, C. Papp, S. Ueda, B. Balke, Y. Yamashita, L. Plucinski, J. Minár, J. Braun, E. Ylvisaker, C. Schneider et al.: Nature Materials **10** (10), 759–764 (2011).

[21] V. N. Strocov, M. Shi, M. Kobayashi, C. Monney, X. Wang, J. Krempasky, T. Schmitt, L. Patthey, H. Berger & P. Blaha: Physical Review Letters **109** (8), 086401 (2012).

[22] C. Varma: Physical Review Letters **83** (17), 3538 (1999).

[23] T. Reber, N. Plumb, Z. Sun, Y. Cao, Q. Wang, K. McElroy, H. Iwasawa, M. Arita, J. Wen, Z. Xu et al.: Nature Physics **8** (8), 606–610 (2012).

[24] P. A. Casey, J. Koralek, N. Plumb, D. Dessau & P. W. Anderson: Nature Physics **4** (3), 210–212 (2008).

[25] Y. Cao & D. D. S: Unpublished.

[26] Y.-D. Chuang, A. Gromko, A. Fedorov, Y. Aiura, K. Oka, Y. Ando, M. Lindroos, R. Markiewicz, A. Bansil & D. Dessau: Physical Review B **69** (9), 094515 (2004).

[27] Z.-H. Zhu, C. Veenstra, G. Levy, A. Ubaldini, P. Syers, N. Butch, J. Paglione, M. Haverkort, I. Elfimov & A. Damascelli: Physical Review Letters **110** (21), 216401 (2013).

[28] A. Bansil, M. Lindroos, S. Sahrakorpi & R. Markiewicz: New Journal of Physics **7** (1), 140 (2005).

[29] Y. Wang, D. Hsieh, D. Pilon, L. Fu, D. Gardner, Y. Lee & N. Gedik: Physical Review Letters **107** (20), 207602 (2011).

[30] M. Scholz, J. Sánchez-Barriga, J. Braun, D. Marchenko, A. Varykhalov, M. Lindroos, Y. J. Wang, H. Lin, A. Bansil, J. Minár et al.: Physical Review Letters **110** (21), 216801 (2013).

[31] M. Mulazzi, G. Rossi, J. Braun, J. Minár, H. Ebert, G. Panaccione, I. Vobornik & J. Fujii: Physical Review B **79** (16), 165421 (2009).

[32] V. Arpiainen, A. Bansil & M. Lindroos: Physical Review Letters **103** (6), 067005 (2009).

[33] X.-L. Qi & S.-C. Zhang: Physics Today **63** (1), 33–38 (2010).

[34] J. E. Moore: Nature **464** (7286), 194–198 (2010).

[35] X.-L. Qi & S.-C. Zhang: Reviews of Modern Physics **83** (4), 1057 (2011).

[36] L. Fu: Physical Review Letters **106** (10), 106802 (2011).

[37] Y. Tanaka, Z. Ren, T. Sato, K. Nakayama, S. Souma, T. Takahashi, K. Segawa & Y. Ando: Nature Physics **8** (11), 800–803 (2012).

[38] X.-G. Wen: Advances in Physics **44** (5), 405–473 (1995).

[39] L. Fu, C. L. Kane & E. J. Mele: Physical Review Letters **98** (10), 106803 (2007).

[40] L. Fu & C. L. Kane: Physical Review B **76** (4), 045302 (2007).

[41] J. E. Moore & L. Balents: Physical Review B **75** (12), 121306 (2007).

[42] Y. ANDO: Journal of the Physical Society of Japan **82** (10), 102001–1 (2013).

[43] H. Zhang, C.-X. Liu, X.-L. Qi, X. Dai, Z. Fang & S.-C. Zhang: Nature Physics **5** (6), 438–442 (2009).

[44] W. Zhang, R. Yu, H.-J. Zhang, X. Dai & Z. Fang: New Journal of Physics **12** (6), 065013 (2010).

[45] S. Basak, H. Lin, L. Wray, S.-Y. Xu, L. Fu, M. Hasan & A. Bansil: Physical Review B **84** (12), 121401 (2011).

[46] C. Nayak, S. H. Simon, A. Stern, M. Freedman & S. D. Sarma: Reviews of Modern Physics **80** (3), 1083 (2008).

[47] D. Hsieh, Y. Xia, D. Qian, L. Wray, J. Dil, F. Meier, J. Osterwalder, L. Patthey, J. Checkelsky, N. Ong et al.: Nature **460** (7259), 1101–1105 (2009).

[48] Y. Xia, D. Qian, D. Hsieh, L. Wray, A. Pal, H. Lin, A. Bansil, D. Grauer, Y. Hor, R. Cava et al.: Nature Physics **5** (6), 398–402 (2009).

[49] N. Read: Physics Today **65** (7), 38–43 (2012).

[50] X.-L. Qi, R. Li, J. Zang & S.-C. Zhang: Science **323** (5918), 1184–1187 (2009).

[51] L. Fu & C. L. Kane: Physical Review Letters **100** (9), 096407 (2008).

[52] R. B. Laughlin: Physical Review Letters **50** (18), 1395–1398 (1983).

[53] L. Fu: Physical Review Letters **103** (26), 266801 (2009).

[54] C.-X. Liu, X.-L. Qi, H. Zhang, X. Dai, Z. Fang & S.-C. Zhang: Physical Review B **82** (4), 045122 (2010).

[55] S. R. Park, J. Han, C. Kim, Y. Y. Koh, C. Kim, H. Lee, H. J. Choi, J. H. Han, K. D. Lee, N. J. Hur et al.: Physical Review Letters **108** (4), 046805 (2012).

[56] S. R. Park, C. H. Kim, J. Yu, J. H. Han & C. Kim: Physical Review Letters **107** (15), 156803 (2011).

[57] Y. Cao, J. Waugh, X. Zhang, J. Luo, Q. Wang, T. Reber, S. Mo, Z. Xu, A. Yang, J. Schneeloch et al.: Nature Physics **9** (8), 499–504 (2013).

[58] N. Bansal, Y. S. Kim, E. Edrey, M. Brahlek, Y. Horibe, K. Iida, M. Tanimura, G.-H. Li, T. Feng, H.-D. Lee et al.: Thin Solid Films **520** (1), 224–229 (2011).

[59] Y. Ishida, H. Kanto, A. Kikkawa, Y. Taguchi, Y. Ito, Y. Ota, K. Okazaki, W. Malaeb, M. Mulazzi, M. Okawa et al.: Physical Review Letters **107** (7), 077601 (2011).

[60] G. Bian, L. Zhang, Y. Liu, T. Miller & T.-C. Chiang: Physical Review Letters **108** (18), 186403 (2012).

[61] J.-W. Luo & A. Zunger: Physical Review Letters **105** (17), 176805 (2010).

[62] Z.-H. Pan, E. Vescovo, A. Fedorov, D. Gardner, Y. Lee, S. Chu, G. Gu & T. Valla: Physical Review Letters **106** (25), 257004 (2011).

[63] M. Hoesch, T. Greber, V. Petrov, M. Muntwiler, M. Hengsberger, W. Auwärter & J. Osterwalder: Journal of Electron Spectroscopy and Related Phenomena **124** (2), 263–279 (2002).

[64] F. Meier, J. Dil & J. Osterwalder: New Journal of Physics **11** (12), 125008 (2009).

[65] O. V. Yazyev, J. E. Moore & S. G. Louie: Physical Review Letters **105** (26), 266806 (2010).

[66] H. Zhang, C.-X. Liu & S.-C. Zhang: Physical Review Letters **111** (6), 066801 (2013).

[67] C.-H. Park & S. G. Louie: Physical Review Letters **109** (9), 097601 (2012).

[68] C. Jozwiak, C.-H. Park, K. Gotlieb, C. Hwang, D.-H. Lee, S. G. Louie, J. D. Denlinger, C. R. Rotundu, R. J. Birgeneau, Z. Hussain et al.: Nature Physics **9** (5), 293–298 (2013).

[69] B. Kim, H. Ohsumi, T. Komesu, S. Sakai, T. Morita, H. Takagi & T. Arima: Science **323** (5919), 1329–1332 (2009).

[70] C. Veenstra, Z.-H. Zhu, M. Raichle, B. Ludbrook, A. Nicolaou, B. Slomski, G. Landolt, S. Kittaka, Y. Maeno, J. Dil et al.: Physical Review Letters **112** (12), 127002 (2014).

[71] D. Pesin & A. H. MacDonald: Nature Materials **11** (5), 409–416 (2012).

[72] S. Wolf, D. Awschalom, R. Buhrman, J. Daughton, S. Von Molnar, M. Roukes, A. Y. Chtchelkanova & D. Treger: Science **294** (5546), 1488–1495 (2001).

[73] K. Miyamoto, A. Kimura, T. Okuda, H. Miyahara, K. Kuroda, H. Namatame, M. Taniguchi, S. Eremeev, T. Menshchikova, E. Chulkov et al.: Physical Review Letters **109** (16), 166802 (2012).

[74] S. V. Eremeev, G. Landolt, T. V. Menshchikova, B. Slomski, Y. M. Koroteev, Z. S. Aliev, M. B. Babanly, J. Henk, A. Ernst, L. Patthey et al.: Nature Communications **3**, 635 (2012).

[75] Z.-H. Zhu, C. Veenstra, S. Zhdanovich, M. Schneider, T. Okuda, K. Miyamoto, S.-Y. Zhu, H. Namatame, M. Taniguchi, M. Haverkort et al.: Physical Review Letters **112**, 076802 (2014).

[76] M. Imada, A. Fujimori & Y. Tokura: Reviews of Modern Physics **70** (4), 1039 (1998).

[77] T. Timusk & B. Statt: Reports on Progress in Physics **62** (1), 61 (1999).

[78] P. A. Lee, N. Nagaosa & X.-G. Wen: Reviews of Modern Physics **78** (1), 17 (2006).

[79] S. Hüfner, M. Hossain, A. Damascelli & G. Sawatzky: Reports on Progress in Physics **71** (6), 062501 (2008).

[80] N. Mott: Reviews of Modern Physics **40**, 677–683 (1968).

[81] A. Fujimori & F. Minami: Physical Review B **30** (2), 957 (1984).

[82] Y. Ohta, T. Tohyama & S. Maekawa: Physical Review Letters **66** (9), 1228 (1991).

[83] J. Falck, A. Levy, M. Kastner & R. Birgeneau: Physical Review Letters **69** (7), 1109 (1992).

[84] P. Anderson: Materials Research Bulletin **8** (2), 153–160 (1973).

[85] S. Yan, D. A. Huse & S. R. White: Science **332** (6034), 1173–1176 (2011).

[86] S. Nakatsuji, Y. Nambu, H. Tonomura, O. Sakai, S. Jonas, C. Broholm, H. Tsunetsugu, Y. Qiu & Y. Maeno: Science **309** (5741), 1697–1700 (2005).

[87] T.-H. Han, J. S. Helton, S. Chu, D. G. Nocera, J. A. Rodriguez-Rivera, C. Broholm & Y. S. Lee: Nature **492** (7429), 406–410 (2012).

[88] S. Mitsuda, G. Shirane, S. Sinha, D. Johnston, M. Alvarez, D. Vaknin & D. Moncton: Physical Review B **36** (1), 822 (1987).

[89] M. Matsumoto, C. Yasuda, S. Todo & H. Takayama: Physical Review B **65** (1), 014407 (2001).

[90] L. Capriotti & S. Sorella: Physical Review Letters **84** (14), 3173 (2000).

[91] P. W. Anderson: Science **235** (4793), 1196–1198 (1987).

[92] W. Kohn: Physical Review Letters **19** (14), 789 (1967).

[93] S. Sachdev: Nature Physics **4** (3), 173–185 (2008).

[94] C. Tsuei & J. Kirtley: Reviews of Modern Physics **72** (4), 969 (2000).

[95] Z.-X. Shen, D. Dessau, B. Wells, D. King, W. Spicer, A. Arko, D. Marshall, L. Lombardo, A. Kapitulnik, P. Dickinson et al.: Physical Review Letters **70** (10), 1553 (1993).

[96] I. Vishik, M. Hashimoto, R.-H. He, W.-S. Lee, F. Schmitt, D. Lu, R. Moore, C. Zhang, W. Meevasana, T. Sasagawa et al.: Proceedings of the National Academy of Sciences **109** (45), 18332–18337 (2012).

[97] E. Razzoli, G. Drachuck, A. Keren, M. Radovic, N. Plumb, J. Chang, Y.-B. Huang, H. Ding, J. Mesot & M. Shi: Physical Review Letters **110** (4), 047004 (2013).

[98] Y. Ando, A. Lavrov, S. Komiya, K. Segawa & X. Sun: Physical Review Letters **87** (1), 017001 (2001).

[99] T. Yoshida, X. Zhou, T. Sasagawa, W. Yang, P. Bogdanov, A. Lanzara, Z. Hussain, T. Mizokawa, A. Fujimori, H. Eisaki et al.: Physical Review Letters **91** (2), 027001 (2003).

[100] K. Shen, F. Ronning, D. Lu, W. Lee, N. Ingle, W. Meevasana, F. Baumberger, A. Damascelli, N. Armitage, L. Miller et al.: Physical Review Letters **93** (26), 267002 (2004).

[101] G. Kotliar & J. Liu: Physical Review B **38** (7), 5142 (1988).

[102] P. A. Lee & N. Nagaosa: Physical Review B **46** (9), 5621 (1992).

[103] Y. Wang, L. Li & N. Ong: Physical Review B **73** (2), 024510 (2006).

[104] R.-H. He, M. Hashimoto, H. Karapetyan, J. Koralek, J. Hinton, J. Testaud, V. Nathan, Y. Yoshida, H. Yao, K. Tanaka et al.: Science **331** (6024), 1579–1583 (2011).

[105] T. Reber, N. Plumb, Y. Cao, Z. Sun, Q. Wang, K. McElroy, H. Iwasawa, M. Arita, J. Wen, Z. Xu et al.: Physical Review B **87** (6), 060506 (2013).

[106] Y.-H. Chen, F. Wilczek, E. Witten & B. I. Halperin: International Journal of Modern Physics B **3** (07), 1001–1067 (1989).

[107] E. Dagotto: Reviews of Modern Physics **66** (3), 763 (1994).

[108] M. Van Veenendaal, G. Sawatzky & W. Groen: Physical Review B **49** (2), 1407 (1994).

[109] M. Meinders, H. Eskes & G. Sawatzky: Physical Review B **48** (6), 3916 (1993).

[110] J. Allen, C. Olson, M. Maple, J.-S. Kang, L. Liu, J.-H. Park, R. Anderson, W. Ellis, J. Markert, Y. Dalichaouch et al.: Physical Review Letters **64** (5), 595 (1990).

[111] P. Phillips: Annals of Physics **321** (7), 1634–1650 (2006).

[112] R. Laughlin: Advances in Physics **47** (6), 943–958 (1998).

[113] G. Aeppli, T. Mason, S. Hayden, H. Mook & J. Kulda: Science **278** (5342), 1432–1435 (1997).

[114] Y. Dagan, M. Qazilbash, C. Hill, V. Kulkarni & R. Greene: Physical Review Letters **92** (16), 167001 (2004).

[115] S. E. Sebastian, N. Harrison, M. Altarawneh, C. Mielke, R. Liang, D. Bonn & G. Lonzarich: Proceedings of the National Academy of Sciences **107** (14), 6175–6179 (2010).

[116] F. Wang & T. Senthil: Physical Review Letters **106** (13), 136402 (2011).

[117] G. Jackeli & G. Khaliullin: Physical Review Letters **102** (1), 017205 (2009).

[118] A. Shitade, H. Katsura, J. Kuneš, X.-L. Qi, S.-C. Zhang & N. Nagaosa: Physical Review Letters **102** (25), 256403 (2009).

[119] D. Pesin & L. Balents: Nature Physics **6** (5), 376–381 (2010).

[120] X. Wan, A. M. Turner, A. Vishwanath & S. Y. Savrasov: Physical Review B **83** (20), 205101 (2011).

[121] Z.-X. Shen & D. Dessau: Physics Reports **253** (1), 1–162 (1995).

[122] S. Ishihara & S. Maekawa: Reports on Progress in Physics **65** (4), 561 (2002).

[123] D. Haskel, G. Fabbris, M. Zhernenkov, P. Kong, C. Jin, G. Cao & M. van Veenendaal: Physical Review Letters **109** (2), 027204 (2012).

[124] Q. Wang, Y. Cao, J. Waugh, S. Park, T. Qi, O. Korneta, G. Cao & D. Dessau: Physical Review B **87** (24), 245109 (2013).

[125] M. Czyżyk & G. Sawatzky: Physical Review B **49** (20), 14211 (1994).

[126] J. K. Perry, J. Tahir-Kheli & W. A. Goddard III: Physical Review B **63** (14), 144510 (2001).

[127] F. Ye, S. Chi, B. C. Chakoumakos, J. A. Fernandez-Baca, T. Qi & G. Cao: Physical Review B **87** (14), 140406 (2013).

[128] M. Ge, T. Qi, O. Korneta, D. De Long, P. Schlottmann, W. Crummett & G. Cao: Physical Review B **84** (10), 100402 (2011).

[129] T. Qi, O. Korneta, S. Chikara, M. Ge, S. Parkin, L. De Long, P. Schlottmann & G. Cao: Journal of Applied Physics **109** (7), 07D906 (2011).

[130] T. Qi, O. Korneta, L. Li, K. Butrouna, V. Cao, X. Wan, P. Schlottmann, R. Kaul & G. Cao: Physical Review B **86** (12), 125105 (2012).

[131] J. Lee, Y. Krockenberger, K. Takahashi, M. Kawasaki & Y. Tokura: Physical Review B **85** (3), 035101 (2012).

[132] H. Zhang, K. Haule & D. Vanderbilt: Physical Review Letters **111** (24), 246402 (2013).

[133] C. Martins, M. Aichhorn, L. Vaugier & S. Biermann: Physical Review Letters **107** (26), 266404 (2011).

[134] T. Sato, T. Kamiyama, T. Takahashi, K. Kurahashi & K. Yamada: Science **291** (5508), 1517–1519 (2001).

[135] F. Ronning, T. Sasagawa, Y. Kohsaka, K. Shen, A. Damascelli, C. Kim, T. Yoshida, N. Armitage, D. Lu, D. Feng et al.: Physical Review B **67** (16), 165101 (2003).

[136] H.-B. Yang, Z.-H. Pan, A. Sekharan, T. Sato, S. Souma, T. Takahashi, R. Jin, B. C. Sales, D. Mandrus, A. Fedorov et al.: Physical Review Letters **95** (14), 146401 (2005).

[137] J. Dai, E. Calleja, G. Cao & K. McElroy: arXiv preprint arXiv:1303.3688 (2013).

[138] J. P. Clancy, A. Lupascu, H. Gretarsson, Z. Islam, Y. F. Hu, D. Casa, C. S. Nelson, S. C. LaMarra, G. Cao & Y.-J. Kim: Physical Review B **89**, 054409 (2014).

[139] Y.-D. Chuang, A. Gromko, D. Dessau, T. Kimura & Y. Tokura: Science **292** (5521), 1509–1513 (2001).

[140] K. M. Shen, F. Ronning, D. Lu, F. Baumberger, N. Ingle, W. Lee, W. Meevasana, Y. Kohsaka, M. Azuma, M. Takano et al.: Science **307** (5711), 901–904 (2005).

[141] S. Grigera, R. Perry, A. Schofield, M. Chiao, S. Julian, G. Lonzarich, S. Ikeda, Y. Maeno, A. Millis & A. Mackenzie: Science **294** (5541), 329–332 (2001).

[142] P. W. Anderson: Nature Physics **2** (9), 626–630 (2006).

[143] D. Hsieh, F. Mahmood, D. Torchinsky, G. Cao & N. Gedik: Physical Review B **86** (3), 035128 (2012).

[144] R. Arita, J. Kuneš, A. Kozhevnikov, A. Eguiluz & M. Imada: <u>Physical Review Letters</u> **108** (8), 086403 (2012).

[145] S. Moser, L. Moreschini, A. Ebrahimi, B. Dalla Piazza, M. Isobe, H. Okabe, J. Akimitsu, V. Mazurenko, K. Kim, A. Bostwick <u>et al.</u>: <u>New Journal of Physics</u> **16** (1), 013008 (2014).

[146] J.-X. Dai: private communication.

[147] Y. Okada, D. Walkup, H. Lin, C. Dhital, T.-R. Chang, S. Khadka, W. Zhou, H.-T. Jeng, M. Paranjape, A. Bansil <u>et al.</u>: <u>Nature Materials</u> **12** (8), 707–713 (2013).

[148] Y. Kohsaka, T. Hanaguri, M. Azuma, M. Takano, J. Davis & H. Takagi: <u>Nature Physics</u> **8** (7), 534–538 (2012).

[149] M. Le Tacon, G. Ghiringhelli, J. Chaloupka, M. M. Sala, V. Hinkov, M. Haverkort, M. Minola, M. Bakr, K. Zhou, S. Blanco-Canosa <u>et al.</u>: <u>Nature Physics</u> **7** (9), 725–730 (2011).

[150] M. Dean, G. Dellea, R. Springell, F. Yakhou-Harris, K. Kummer, N. Brookes, X. Liu, Y. Sun, J. Strle, T. Schmitt <u>et al.</u>: <u>Nature Materials</u> (2013).

[151] J. Kim, D. Casa, M. Upton, T. Gog, Y.-J. Kim, J. Mitchell, M. Van Veenendaal, M. Daghofer, J. van Den Brink, G. Khaliullin <u>et al.</u>: <u>Physical Review Letters</u> **108** (17), 177003 (2012).

[152] J. Kim, A. Said, D. Casa, M. Upton, T. Gog, M. Daghofer, G. Jackeli, J. van den Brink, G. Khaliullin & B. Kim: <u>Physical Review Letters</u> **109** (15), 157402 (2012).

[153] T. Okuda & A. Kimura: <u>Journal of the Physical Society of Japan</u> **82** (2) (2013).

Appendix A

The Hemispherical Electron Analyzer

In this appendix, we focus on the design of hemispherical analyzers, which is and will very likely remain the major workhorse of ARPES. The ultimate goal of the electron analyzer is to separate photoelectrons by the kinetic energy and momentum. We treat the sample as an extended electron source, with a size comparable to the projected area of the incoming photon beam. Electrons travel with different kinetic energies and in all directions away from the sample.

The hemispherical analyzer uses electrostatic fields to steer electrons, and consists of two parts (Figure A.1): the cylindrical lens (hereafter lens) and the hemisphere. Electrons emitted from the extended source are refracted in the lens towards a focal plane, with different points on the plane corresponding to a unique emission angle. In other words, the lens Fourier transforms the angular distribution of electrons into a spatial distribution on the focal plane. There is a narrow slit between the lens and the hemisphere, so that only electrons along a line cut in k-space are allowed into the hemisphere. These electrons are then bent across the hemisphere and fly towards the micro-channel plate (MCP). The spatial distribution of the electrons on the MCP is recorded, representing the electron distribution in enegry and momentum (along an one-dimensional line in k-space).

We refer to the cylindrical electrodes as "lenses" due to their similarity with the optical lenses. The trace of electrons in an electrostatic field follows the Principle of Least Action in classical mechanics, while the path of a light ray between two points in space is the one with the least time (Fermat's principle). This way we could introduce optical concepts including lens,
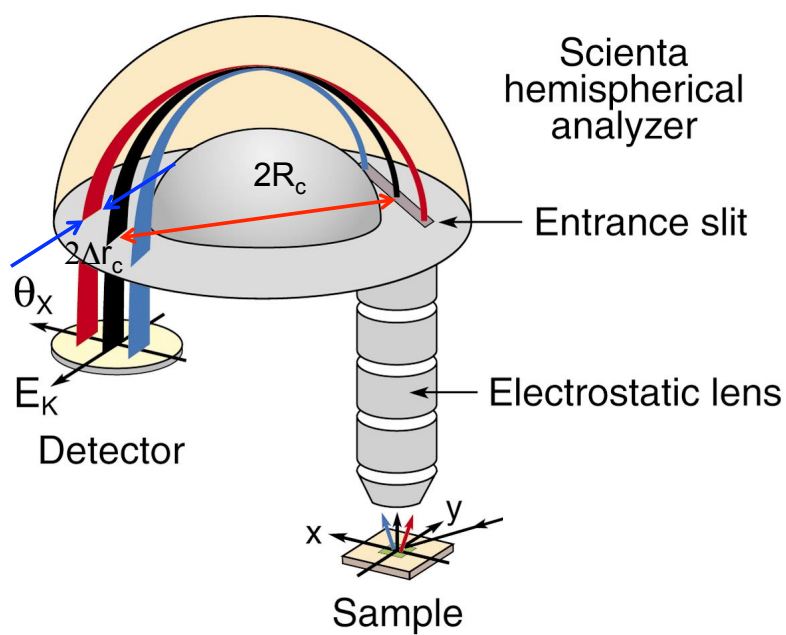
Figure A.1: The hemispherical electron analyzer consists of the hemisphere and the cylindrical lens. The lens spatially separates the ejected electrons from the material by their emission angle relative to the sample normal, and the hemisphere further maps the kinetic energy of electrons. Figure reproduced from [8].

aberration, etc. to describe the electron trajectory. In fact the research on steering the electrons is called "electron optics".

We could also understand this "optics — electron optics" analogy from the analysis below: in Figure A.2 **a**, an electron travels from a region with local potential V to one with potential $V + \Delta V$. We assume there is a hard interface between the two potentials. The electron momentum normal to the interface is conserved, while the momentum along the interface is retarded/accelerated due to the potential difference. We could derive a "Snell's Law" for an electron with kinetic energy T with the electric potential V

$$\sqrt{T} \sin \alpha_1 = \sqrt{T + e\Delta V} \sin \alpha_2 \tag{A.1}$$

For $\Delta V > 0$, the electron is refracted towards the normal direction at the interface (Figure A.2 **a**). In reality, the electric potential changes smoothly in space (Figure A.2 **b**). We could think of electrons as flying through a continuum of interfaces with infinitesimal potential changes and varying index of refraction.

To design the Fourier lens needed, manufacturers often (but not necessarily) stack a series of Einzel lens together. The geometry of a typical Einzel lens is shown in Figure A.2 **b**. Each Einzel lens has three electrodes, and the center has a higher/lower voltage than the electrodes on the two sides. The equal potential surfaces are drawn in Figure A.2 **b**. It is apparent that the Einzel lens is very "fat". How to correct the severe spherical and chromatic aberrations from these "fat" electric lenses is crucial for improving the performance of the electron analyzer. A partial solution is to design lens systems with a large diameter, so that electron trajectories are better approximated by paraxial optical rays and experience less aberrations.

The hemisphere has two concentric electrodes, with the outer hemisphere placed at a more negative potential (Figure A.1). The electric field between the inner and outer shells follows $\propto 1/r^2$. For a given potential difference between the inner/outer spheres, only electrons with a specific kinetic energy (which we call the pass energy E_P) can travel along a circular path and land at the center of the MCP on the other side of the hemisphere. Electrons with higher/lower kinetic energy
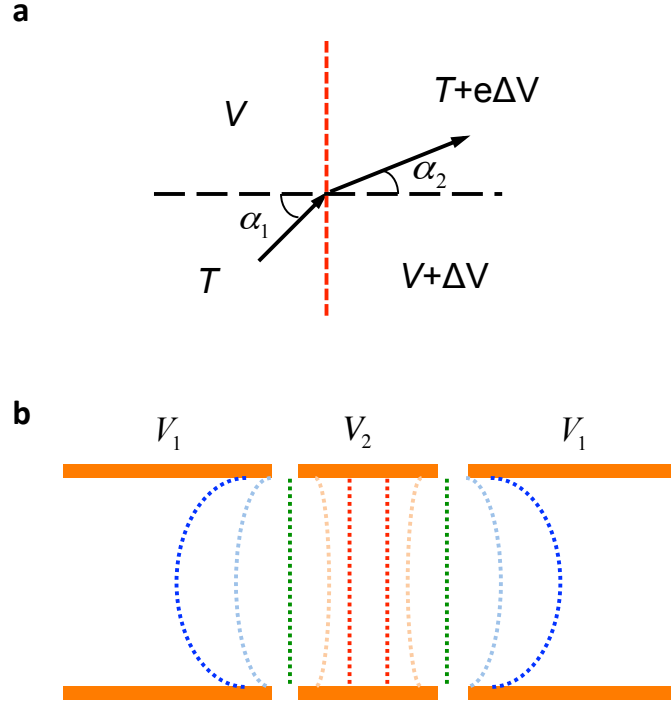
Figure A.2: Working mechanism of the electrostatic lens. **a**. The electron bends as it travels across a hypothetical interface with different electric potential on the two sides. With $\Delta V > 0$, the electron is bent towards the normal direction at the interface. **b**. A typical geometry of an Einzel lens. The center electrode has a higher/lower potential than those on the two sides. The colored lines are equal potential surfaces in the cylindrical lens.

land away from/towards the center of the hemisphere, with an elliptical trajectory. Thus we could map the location of the electron on the MCP to its kinetic energy at the slit. The kinetic energy of the photoelectron $E_k \pm \Delta E$ and the kinetic energy at the slit $E_P \pm \Delta E$ are further related by

$$E_k \pm \Delta E = (E_P \pm \Delta E) - eV_{\text{diff}} \tag{A.2}$$

where e is the electron charge and V_{diff} is the voltage difference between the slit and the sample (which is usually grounded). Electrons flying through different spots along the slit (Figure A.1) are distributed on the MCP parallel to the slit, corresponding to different emission angles from the sample. Thus the angle and energy axes of the energy-angle intensity map on the MCP are parallel and normal to the slit, respectively.

The energy resolution of the hemispherical analyzer is dominated by [8]

$$\Delta E_{res} = \mathcal{O}\left(\frac{w}{R_c} E_P\right) \tag{A.3}$$

where w is the width of the slit and R_c is the radius of the circular path of electrons (see Figure A.1). This is why more recent analyzers usually have larger hemispheres than their precursors. We could also improve the analyzer resolution by using lower pass energies. However electrons with lower pass energy are more likely to be affected by the the fringe electric field which appears at the corner of the slit or close to the electrode. Moreover, lower pass energy means a smaller energy window available on the MCP.

Recent progress in the ultrafast laser >6eV has boosted the use of time-of-flight electron analyzers [29], where electrons are detected in the temporal order they arrive at the analyzer. These analyzers are cylindrical lens, without the hemisphere. As the slit is removed, more electrons are collected per unit time.

We have discussed spin-resolved ARPES results in Chapter 3. The spin-resolved hemispherical analyzers have an additional spin detector where spin-up/down electrons are scattered off a target with different probabilities. The commonly-used spin detectors include Mott chambers and VLEED detectors, among others. A detailed review is available in Ref. [153].